IDEA League

MASTER OF SCIENCE IN APPLIED GEOPHYSICS

RESEARCH THESIS

Feature extraction of GPR data for the classification of reflectors in reinforced concrete

Lena Gierens

August 5, 2020

TU DELFT ETH ZURICH RWTH AACHEN

Feature extraction of GPR data for the classification of reflectors in reinforced concrete

Master of Science Thesis

for the degree of Master of Science in Applied Geophysics at
RWTH Aachen University
by

Lena Gierens

August 5, 2020

Faculty of Georesources and Material Engineering, RWTH Aachen University
BAM-Fachbereich 8.2, Bundesanstalt für Materialforschung und -prüfung (BAM)

RWTH Aachen University

Printed in Germany

IDEA LEAGUE
JOINT MASTER'S IN APPLIED GEOPHYSICS

Delft University of Technology, The Netherlands
ETH Zürich, Switzerland
RWTH Aachen, Germany

Dated: *August 5, 2020*

Committee Members:

Dr. rer. nat. Ernst Niederleithinger

Prof. dr. ir. C.P.A. Kees Wapenaar

Supervisor(s):

Dr. rer. nat. Ernst Niederleithinger

Dr. Thomas Kind

Abstract

During their service live reinforced and prestressed concrete structures experience deterioration. Therefore, to effectively assure the safety and durability of the compounds, non destructive testing methods, such as Ground Penetrating Radar, employed at high frequencies, provide a rapid assessment of the geometry of the compound. Although amplitude and traveltime evaluations are the most widely used techniques, attribute based analysis to enhance the interpretation quality has gained interest in recent years. A great quantity of surveys exist that attempt to determine the diameter of cylindrical targets such as reinforcement bars or tendon ducts. Indeed, the affiliation of a reflector to one of the two groups is still a challenging task. Therefore, different attribute approaches are applied to four data sets with high spatial sampling rates collected under controlled conditions, to derive features that unambiguously assign the considered reflection hyperbolas to either reinforcement bars or tendon ducts. For this purpose, B-scans are reduced to the individual reflectors by manual selecting the desired windows. Then, attributes are applied to the hyperbolas and the results are compared with each other to derive features describing the two reflector types. For attributes where features can be extracted, they are tested for measurements with relatively low spatial sampling rates and for one on-site data set. It is shown that the analysis provides sufficient classifications for six out of the nine tested attributes when data with high spatial sampling rates under controlled environment conditions are considered. In contrast, relatively low spatial sampling rates yield to accurate results for only three attributes: The maximum absolute amplitude, the cumulative energy and the amplitude at the apex. Although promising results for low spatial sampling rates are obtained, the application to on-site data is still complicated. Nevertheless, this study provides the basis for automated reflector classification.

Acknowledgements

First of all, I am very grateful for the opportunity to work on my thesis in cooperation with BAM Division 8.2. I would like to thank my supervisor Dr. Thomas Kind who was very supportive during my thesis and always available to answer any upcoming question. His sometimes critical but in any case constructive view on the project inspired me to improve the developed approaches. I also owe my sincere thanks to Dr. Ernst Niederleithinger for the assistance and suggestions throughout this project. Many thanks go to all people of BAM who formed a very helpful and supportive environment, especially to Niklas Epple, Tim Klewe and Stefan Küttenbaum for the constructive and scrutinizing comments to finalize my thesis. A big thank-you also goes to Jens Wöstmann who introduced me to the acquisition system and helped me to organize the printing and the timely submission of my thesis. Last but not least, I want to express my heartfelt thanks to my family and friends for their unfailing support and continuous encouragement throughout these two years. Special thanks go to Johanna Klahold for our precious and enthusiastic discussions and for the incredibly valuable moments that we experienced during our studies.

RWTH Aachen University Lena Gierens
August 5, 2020

Table of Contents

Abstract **v**

Acknowledgements **vii**

Nomenclature **xv**

Acronyms **xv**

1 Introduction **1**

2 Theory of Electromagnetic Waves **5**

- 2-1 Electromagnetic Fields 5
  - 2-1-1 Interaction of Fields with Matter 7
  - 2-1-2 Material Properties 8
- 2-2 Electromagnetic Waves 10
  - 2-2-1 Electromagnetic Wave Equation 11
  - 2-2-2 Solution to the Wave equation 12
    - Plane Time-Harmonic Waves 13
  - 2-2-3 Wave Polarization 14
- 2-3 Boundary Conditions 15
  - 2-3-1 Reflection, Refraction and Transmission 16
    - Reflection From a Buried Conductor 17
  - 2-3-2 Scattering and Diffraction 17
  - 2-3-3 Target Polarization 18

3 Ground Penetrating Radar 21
3-1 Fundamentals 21
3-1-1 Total Path Loss 22
3-1-2 Vertical and Horizontal Resolution 23
3-1-3 Antenna Types 24
3-2 Survey Design and Parameters 25
3-2-1 Antenna Polarization and Orientation 26
3-3 Reflection Pattern for Conductive Cylinders 27

4 Reinforced and Prestressed Concrete 29
4-1 Fundamental Theory 29
4-2 Tasks for Non Destructive Testing 32

5 Materials and Method 33
5-1 Concrete Test Specimens 33
5-2 Measuring System and Data Acquisition 36
5-3 Preprocessing 38
5-3-1 Hyperbolic Reflection Specific Processing 39
5-4 Classification Attribute Analysis 41
5-4-1 Amplitude Based Attributes 43
5-4-2 Geometry of the Hyperbolic Signature 48
5-4-3 Logistic Regression 49

6 Results 51
6-1 Preprocessing Results 51
6-2 Amplitude Based Attributes 52
6-3 Geometry of the Hyperbolic Signature 61

7 Discussion 63

8 Conclusion and Outlook 69

Bibliography 71

A Materials and Methods 79

B Results 81
B-1 Preprocessing Results 82
B-2 Extracted Hyperbolic Reflections 87
B-3 Amplitude Based Attributes 90
B-4 Geometry of the Hyperbolic Signature 105
B-5 Random Data Points 106

C Python Programs 109

List of Figures

2-1 Detachement of EM waves from a dipole antenna. 11
2-2 Polarization of the electrical field vector. 15
2-3 Electromagnetic wave at normal incidence. 16
2-4 $\boldsymbol{E}$-parallel and $\boldsymbol{E}$-perpendicular excitation relative to a cylinder. 19
2-5 Scattering Width for a conductive cylinder. 20

3-1 GPR example trace. 22
3-2 Schematic of the Fresnel zone. 24
3-3 Common offset acquisiton mode. 25
3-4 Antenna polarizations for GPR: E-horizontal and E-vertical. 27
3-5 Formation of the characteristic hyperbolic pattern for scattering from a cylinder. 28

4-1 Nonreinforced, reinforced, and prestressed conctrete beams. 30
4-2 Picture of a reinforcement bar and a tendon duct. 31

5-1 Schematic representation of the concrete specimens. 35
5-2 Antenna orientations for measurement *B-2*. 38
5-3 Flow chart of the data preparation. 40
5-4 Overlap positions for two antenna orientations in case of unequal spatial sampling rates. 41
5-5 Comparison of reflection hyperbolas with $R = 0$ and $R \neq 0$. 48

6-1 Dewowed and background removed radargram for measurement *A*. 53
6-2 Reflection and propagation attributes for measurement *A*. 54
6-3 Maximum absolute amplitude and cumulative energy for the extracted reflection events. 55
6-4 Normalized amplitude variance for measurement *A*. 57
6-5 Amplitude ratios for the orthogonal polarizations for measurement *A*. 57

6-6 Apex amplitudes of the hyperbolas. . . . 58
6-7 Mean of the normalized hyperbola range. . . . 59
6-8 Slope of the line fit for the autocorrelation. . . . 60
6-9 Peak-to-peak amplitude ratios. . . . 61
6-10 Velocity of the hyperbola fit. . . . 62

7-1 Maximum absolute amplitude and cumulative energy for the extracted reflection events with clusters. . . . 65
7-2 Apex amplitudes of the hyperbolas with clusters. . . . 67

B-1 Dewowed and background removed radargrams of measurement *B-1*. . . . 82
B-2 Dewowed and background removed radargrams of measurement *C*. . . . 83
B-3 Dewowed and background removed radargrams of measurement *D*. . . . 84
B-4 Dewowed and background removed radargrams of measurement *B-2*. . . . 85
B-5 Dewowed and background removed radargrams of measurement *E*. . . . 86
B-6 Radargram with extracted hyperbolas for measurements *A* and *B-1*. . . . 87
B-7 Radargram with extracted hyperbolas for measurements *C* and *D*. . . . 88
B-8 Radargram with extracted hyperbolas for measurement *E*. . . . 89
B-9 Reflection and propagation attributes for measurements *B-1* and *C*. . . . 91
B-10 Reflection and propagation attribute of measurements *D*, *B-2* and *E*. . . . 92
B-11 Cumulative energy B-Scans. . . . 93
B-12 Relation between cumulative energy and maximum absolute amplitude. . . . 94
B-13 Normalized amplitude variance for measurements *A* and *B-1*. . . . 95
B-14 Normalized amplitude variance for measurement *C*. . . . 96
B-15 Normalized amplitude variance for measurement *D*. . . . 97
B-16 Normalized amplitude variance for measurement *B-2*. . . . 98
B-17 Amplitude ratios for the orthogonal polarizations. . . . 99
B-18 Mean of the hyperbol range for measurements *B-1* and *C*. . . . 100
B-19 Mean of the hyperbol range for measurements *D* and *B-2*. . . . 101
B-20 Apex value for the mean of the hyperbola range. . . . 102
B-21 Autocorrelation of the apex trace for measurement *A* and *B-1*. . . . 103
B-22 Autocorrelation of the apex trace for measurements *C* and *D*. . . . 104
B-23 Relationship of the peak-to-peak amplitude ratio for the two polarizations. . . . 105
B-24 Hyperbolas for the extracted reflection events. . . . 105
B-25 Maximum absolute amplitude and cumulative energy in comparison with random data points. . . . 106
B-26 Apex amplitudes of the hyperbola in comparison with random data points. . . . 107

List of Tables

4-1 Typical diameters of reinforcement bars and tendon ducts. 31

5-1 Material parameters for air, concrete and steel. 34
5-2 Survey parameters for the measurements at the different specimens. 37
5-3 Summary of the considered attributes. 42

A-1 Structural composition of the concrete specimens. 79
A-2 Coordinates for the extracted reflectors. 80

B-1 Summary of the results for the feature extraction. 90

C-1 Python programs used for preprocessing and hyperbola selection. 109
C-2 Python programs used for feature extraction. 110
C-3 Python function used for attribute analysis (A to M). 111
C-4 Python function used for attribute analysis (N to Z). 112

Acronyms

DUT Delft University of Technology

ETH Swiss Federal Institute of Technology

RWTH Aachen University

EM Electromagnetic

GPR Ground Penetrating Radar

RCS Radar Cross Section

SW Scattering Width

TWT Two Way Traveltime

NDT Non Destructive Testing

PL-BD, PL Parallel Broadside

PR-BD, PR Perpendicular Broadside

GSSI Geophysical Survey Systems, Inc.

SC Structure scanner measurements

MA Manual measurements

2D, 3D two-dimensional, three-dimensional

arb. unit Arbitrary unit

Chapter 1

Introduction

Reinforced and prestressed concrete with its build-in elements, such as reinforcement bars and tendon ducts, are the fundamental compounds for constructions like buildings, bridges, tunnels and the like. During their service life civil structures are subjected to deterioration mechanisms conditioned by reinforcement corrosion, extreme loads, climate change and natural catastrophes, yielding to damage and consequently to a loss of the structural element (Li et al., 2009; Wang, 2018). To prevent the damage, non destructive investigation is fundamental to ensure serviceability by simultaneously providing information on the geometry of the compound. Ground Penetrating Radar (GPR) is based on the propagation of electromagnetic (EM) waves to detect changes in material properties and thus to derive information about the investigated material. Therefore, it offers comprehensive and accurate assessment of the geometry, i.e. localization of reinforcement bars or tendon ducts (Annan et al., 2002). Consequently, it has become one of the most important tools for evaluating infrastructural elements. In addition, the rapid acquisition velocity allows to maintain the serviceability yielding to a low out-of-service time of the structural component and accordingly reduces inspection costs. Planning of rehabilitation schemes and quality control requires the best knowledge of position, size and shape of any embedded element as construction plans do not entirely cover the condition of the structure (Dérobert et al., 2018). Yet, the classification of the located objects is key in order to assess the potential impairment since the different types of elements have their almost independent purpose. Reinforcement bars and tendon ducts are considered to behave as conductive cylinders in a dielectric material. Accordingly, they result in a characteristic hyperbolic imprint in GPR data (Bungey et al., 1994). Since the response of those objects is strongly influenced by the electromagnetic properties of the dielectric, and on the depth, diameter and orientation of the target (Shihab and Al-Nuaimy, 2005), simple visual amplitude inspection is insufficient in many real case scenarios.

A great quantity of GPR surveys were conducted with the purpose of determining the diameter of cylindrical objects, i.e., Chang et al. (2009), Leucci (2012), Sangoju (2017), Shihab and Al-Nuaimy (2005), Utsi and Utsi (2004) and Zanzi and Arosio (2013). Indeed, to the best knowledge of the author no survey exist which evaluates reflectors with respect to a classification in compliance with their purpose of design: Reinforcement bar or tendon duct.

Accordingly, this thesis aims to find measures which clearly indicate the affiliation of a reflector to a certain category by simultaneously keeping the computational effort small. This derives a feature that characterizes the individual object types and enhances the classification quality. Attribute analysis was originally developed for seismic data interpretation and has gained interest in recent years. Thus, a number of surveys were performed showing the potential of attribute based analysis for GPR surveys. Due to the total reflection of the radar wave at conductive steel elements, the dominant difference between reinforcement bars and tendon ducts is the change in diameter of the cylindrical shape. However, GPR surveys can be utilized to sufficiently determine the position and orientation of cylindrical objects. Whereas for estimating the diameter it only serves as an indicative measure as it is challenging to gain a proper estimation, shown by Chang et al. (2009), Leucci (2012), Sangoju (2017), Shihab and Al-Nuaimy (2005), Utsi and Utsi (2004) and Zanzi and Arosio (2013).

In Chapter two, the theory of electromagnetic waves with respect to the interaction with matter is developed and a plane wave solution to the EM wave equation is provided. Furthermore, a short introduction into boundary conditions is given to form the basis for target polarization. Chapter three covers the fundamentals of Ground Penetrating Radar and focuses on survey design to determine the acquisition parameters. At the end, the generation of the hyperbolic reflection pattern is discussed. Next, Chapter four gives a brief overview of reinforced and prestressed concrete and discusses the advantages and disadvantages. Attribute based analysis is applied to high spatial sampling rate data collected at four different concrete specimens and to one manual measurement from one of these specimens. Additionally, one on-site data set acquired at a bridge in Northwestern Germany is evaluated but is showing insufficient results. To evaluate the reflections from multiple conductive cylinders, i.e. rebars and tendon ducts, the hyperbolic signatures are manually extracted from B-scans. Accordingly, the four concrete specimens, the acquisition software and the parameter settings are explained in Chapter five. Then nine attributes which can be divided into amplitude based and geometry related attributes (described in Chapter five), are tested for the selected hyperbolas. The results from this analysis are presented in Chapter six. For measurements under controlled conditions three of them result in the correct affiliation of a reflector to either rebars or tendon ducts: Reflection attributes, cumulative energy and apex amplitude. In total six attributes provide adequate results for data with high spatial sampling rates, i.e., the maximum of the mean trace, the peak-to-peak ratio and the hyperbola fitting velocity, and thus constrains further limitations on the sampling intervals for manual measurements (see Chapter seven). The remaining attributes: Amplitude variance, autocorrelation function and amplitude reverberations, lead to misclassification as no clear decision line between rebars and tendon ducts can be found. Finally, in Chapter eight conclusions are drawn and possibilities for future work are provided.

Current State of Research

In many surveys the approaches to estimate the size of reinforcement show good results when applied under controlled environment conditions but are only seldom tested at real case data and thus, rarely applied for industrial usage. Doğan and Turhan-Sayan (2016) investigate cumulative energy curves enabling the detection of a buried target in the highly simplified case of only one intrusion but does not provide information about the shape of the object.

Queiroz et al. (2012) however, uses attribute analysis to solve the inverse problem regarding the characterization of embedded objects in dielectrics with regard to the electrical properties and the depths of intrusions. Indeed, for real data application the diameter of the objects was not varied, being the major limitation of this study. Further, Chang et al. (2009) and Sangoju (2017) apply a method based on the power reflectivity to calculate rebar diameters. For the highly idealized measurements at test specimens they propose an accuracy for the estimation of 7 %. Other authors focus on the angle dependent reflectivity of cylinders where the maximum amplitude is created when the incident electrical field is parallel to the long axis of the elongated cylinder and hence, showing a larger radar cross section (RCS) value. Accordingly several studies have proven that combining different antenna orientations (incident electrical field parallel or perpendicular to the long axis of the cylinder) provides information about the orientation of elongated objects (Van Gestel and Stoffa, 2001; Roberts, 1994; Roberts and Daniels, 1996; Al-Zayer, 2005). Furthermore, the RCS is strongly dependent on the diameter of the target cylinder yielding to the potential to investigate the amplitude ratio of two antenna orientations. This was successfully applied by Utsi and Utsi (2004) for controlled environments. Providing an accuracy for the estimation of 20 %, they state that the capability for on-site studies is limited. Nevertheless, Leucci (2012) adapted this technique and applied it to both, synthetic and real data stating an accuracy of 6 %. Indeed, Zanzi and Arosio (2013) evaluated this property with special focus on the comparison between theoretical prediction and real data, showing uncertainties especially with regard to on-site experiments. Eisenmann et al. (2013) makes use of the dependency between the peak amplitude of the hyperbola and the size and depth of the object and establishes a relationship for these parameters considering rebars in air. Within the study of Shihab and Al-Nuaimy (2005) the hyperbolic reflection pattern was modeled for finite diameters resulting in an accuracy of 9 %. Only two examples are provided however the authors state the successful application for real data. Also, Leucci (2012) uses this fitting method to analyze hyperbolas, demonstrating the capability for diameter determination. Further, Ristic et al. (2009) developed an algorithm based on a nonlinear model with an optimality criterion resulting in a more accurate and robust diameter estimation compared to Shihab and Al-Nuaimy (2005). In addition, in Syambas et al. (2009) the authors propose an algorithm that sorts the amplitudes within a defined window around the reflection signature to gain shape information. Park et al. (2018) investigates the phase of the signal to retrieve information about the material type of the buried intrusion. In Morris et al. (2019) relative differences between attributes, i.e., reflection and propagation attributes, for two case studies are presented and the sensitivity of the considered attributes to material property differences is stated. Böniger and Tronicke (2010) and Zhao et al. (2013) show that amplitude based attribute analysis can be sufficiently applied to 3D data in archaeological investigations providing an enhanced detectability of target remains. Further, Castro et al. (2014) discuss the applicability of various seismic attributes to GPR data in a geological context enabling the understanding of depositional environments in inactive dunes. The authors state the increased quality of visual inspections. Concluding, the aforementioned studies prove that attribute based analysis can be used to sufficiently delineate and characterize reflections within GPR data.

Chapter 2

Theory of Electromagnetic Waves

Ground Penetrating Radar is a geophysical method based on the propagation of electromagnetic waves consisting of two orthogonal vector components: the electric intensity $\boldsymbol{E}$ and the magnetic flux density $\boldsymbol{B}$. To generate *Electromagnetic (EM) waves* as used to investigate the subsurface or civil structures, accelerated charges are needed to radiate energy into the medium of interest. Thus, the interaction between electric and magnetic fields for static and non-static cases need to be understood. Therefore, this Chapter contains basic concepts about electromagnetic fields in free space and its interaction with matter. Next, the generation and detection of electromagnetic waves is discussed and a plane wave solution to the wave equation is presented. In addition, some fundamental properties for the polarization of EM waves are introduced. As GPR requires the wave to be reflected at interfaces, boundary conditions are presented with their consequences for reflection, refraction and transmission of the waves, especially for the reflection on conductive mediums like steel. Finally, the concept of target polarization is introduced forming the basis for the survey design.

2-1 Electromagnetic Fields

When studying Electromagnetic fields, one primarily has to deal with the study of charges at rest and in motion. Attraction and repulsion of two static charges is summarized in *Coulomb's law* (Coulomb, 1953), showing in addition, that electrical forces between two charges decrease as the square of the distance between the two increases. Indeed, when dealing with moving charges, this is not completely true, since the force acting on these particles can be characterized by two vector quantities: the electrical force and the magnetic force (Lovejoy, 1993).

Accordingly, the total electromagnetic force $\boldsymbol{F}$ acting on a moving charge q at position (x, y, z) is represented by the *Lorentz force* (see Eq. (2-1a)) which combines electrical ($q\boldsymbol{E}$) and magnetic forces ($q(\boldsymbol{v} \times \boldsymbol{B})$) and thus accounts for the interaction between static currents. Where $\boldsymbol{v}$ represents the constant velocity at which the charge is traveling. It also reveals that the magnitude and direction of the total electromagnetic force depends on the direction of motion of the charged particle (Feynman et al., 2010). Particularly this can be seen when considering only the last part of Equation (2-1a): The magnetic force is perpendicular to the direction of motion and to the magnetic field.

$$\boldsymbol{F} = q\left(\boldsymbol{E} + \boldsymbol{v} \times \boldsymbol{B}\right) \tag{2-1a}$$

Rather than dealing with forces, it is more convenient to consider electrical fields $\boldsymbol{E}(t, \boldsymbol{x})$ in volt per meter (V/m) and magnetic fields $\boldsymbol{B}(t, \boldsymbol{x})$ in Tesla ($\mathrm{T} = \mathrm{Vs/m^2}$) associated with every point in space as they are present even if the charge at $\boldsymbol{x}$ which experienced the forces, is removed. Thus, the two fields can be seen as the force that a potential charge would experience at a particular position in space. As seen above, the two fields are vector quantities with magnitude and direction and can additionally depend on the time t.

While stationary electric charges or charge distributions can only produce electrical fields in the surrounding space, charges in motion, like stationary electric currents, will also cause magnetic fields. This property is considered when talking about *Static Electromagnetism* where it is assumed that none of the field quantities are time dependent and therefore the electricity and magnetism can be regarded independently, resulting in two pairs of uncoupled partial differential equations, namely the *Maxwell's equation* for the *static case*. However, in *Ground Penetrating Radar* one has to deal with time-dependency and thus, the more complex, first order, coupled partial differential equations are considered, where $\rho(t, \boldsymbol{x})$ is the total charge density in coulombs per cubic meter ($\mathrm{C/m^3}$), $\boldsymbol{j}(t, \boldsymbol{x})$ the total electric current density in amperes per square meter ($\mathrm{A/m^2}$) and $\epsilon_0 = 8.854 \times 10^{-12}$ As/Vm (ampere seconds per volt meter) and $\mu_0 \approx 4\pi 10^{-7}\ \mathrm{N/A^2}$ (newton per ampere squared) are the electrical permittivity and the magnetic permeability in free space, respectively:

$$\nabla \cdot \boldsymbol{E} = \frac{\rho}{\epsilon_0}, \tag{2-2a}$$

$$\nabla \times \boldsymbol{E} = -\frac{\partial}{\partial t}\boldsymbol{B}, \tag{2-2b}$$

$$\nabla \cdot \boldsymbol{B} = 0, \tag{2-2c}$$

$$\nabla \times \boldsymbol{B} = \mu_0 \left(\boldsymbol{j} + \frac{\partial}{\partial t}\epsilon_0 \boldsymbol{E}\right). \tag{2-2d}$$

Contrary to the static case, the equations in (2-2a) - (2-2d) contain time-derivatives and describe the coupling between the electric and magnetic fields. However, they represent the microscopic systems and thus do not account for anything else than free space (see Section 2-1-1).

To summarize the content of these important equations, *Gauss' law* in Eq. (2-2a) characterizes the flux of the electric field through a closed surface being equal to the charge density divided by the constant electric permittivity ϵ_0, meaning that it is proportional to the charge contained by this surface. Thus, it describes how the static electric field is generated simply by a distribution of electric charges. Next, *Faraday's law* Eq. (2-2b) states that a time-varying magnetic field causes a circulating electric field. Equation (2-2c), known as Gauss' law for magnetic fields describes, that there exist no magnetic monopoles, hence no isolated positive or negative magnetic charge exists. Thus, no flow sources are present and as a result the net outwards flux of the magnetic field through the closed surface will always be zero. By considering the conservation of charge, the last of Maxwell's equations was formulated (see Eq. (2-2d)): The flux through a closed boundary is equal to the total change in quantity in this volume. Therefore, the *Displacement Current* term was added to *Ampère's law* to account for changing electric fields producing magnetic fields. This term is similar to real currents but does not require moving charges. This shows, that not only an electrical current but also a changing electrical flux through a particular surface can produce a circulating magnetic field (Feynman et al., 2010; Balanis, 2012; Davis, 1990; Ling et al., 2016).

To emphasize, a time-varying magnetic field gives rise to a time-varying electric field and vice versa, given by Faraday's and Ampère's laws, respectively. This mutual induction causes the existence and propagation of electromagnetic waves as kind of a chain reaction.

2-1-1 Interaction of Fields with Matter

Until now, exclusively electromagnetic fields in free-space were considered. However, as GPR investigates the subsurface or structural elements, materials effecting the magnetic and electric fields are substantial for this method. Any kind of matter consists of positive and negative electric charges in form of atoms. In electrostatics, it is supposed that some charges are quasi-free to migrate in the substance (*conduction* charges) and some are bound and thus cannot move independent of each other (*polarization* charges). This is why two main groups of matter are investigated: *Conductive* and *dielectric* materials (Balanis, 2012; Kansu, 2013). In conductive bodies the atoms form a structure in which electrons can easily hop around from one atom to another although the nucleus stays fixed. Thus, under the influence of an external electrical field the negative charges which are situated close to their nucleus experience an electrical (Coulomb) force and start to migrate in the direction determined by the applied field (Ellingson, 2018; Lovejoy, 1993). The region from where the electrons have migrated away shows a surplus of positive charges whereas the region to which they moved shows a negative surplus (Everett, 2013).

In contrast, the motion of electrons in dielectrics is limited as they are strongly bounded to their nucleus. When a dielectric is brought into an electrical field, the electron cloud surrounding the positive nucleus is influenced such that small electrical dipole moments are created. This is because the negative charges are displaced in a direction opposite to the positive charges, resulting in a polarized material (Balanis, 2012; Everett, 2013). In the same way, a molecule which has an asymmetric charge distribution will be aligned under the influence of an external electrical field. This type of polarization becomes extremely important in wet materials as water is an asymmetric molecule (Everett, 2013). As a result of the microscopic charge displacement the inside of a dielectric material remains electrically neutral because the positive charge of the dipoles cancels with the negative charge of neighboring dipoles. Contrary, the charges at the surface are non-zero and form so-called bound charges (Kansu, 2013). Thus, the cumulative effects account for the characteristic behavior of dielectric materials and the polarization $\boldsymbol{P}$ is always directed parallel to the associated external electrical field. Following this, the total charge density has contributions from both bounded and free charges and hence can be written as: $\rho = \rho_{free} + \rho_{bound}$ (Kansu, 2013; Poplavko, 2019).

In analogy to the separation of the charges, electrical currents causing magnetic fields can be classified as well. Magnetization is less important for this work and thus the topic is only marginal addressed. Electrons oscillating around their nucleus cause magnetic fields which on the macroscopic scale can be seen as magnetic dipoles. In materials in which this is randomly occurring, the dipoles cancel each other (Kansu, 2013). However, in an external magnetic field they experience a torque and eventually align depending on the type of matter. The materials are separated into different groups: The first one, ferromagnetic materials, a special case as they retain their magnetization resulting in so-called permanent magnetization. Even if the magnetic field is removed the microscopic dipoles are still aligned in the direction of $\boldsymbol{B}$. In paramagnetic materials the magnetization $\boldsymbol{M}$ occurs in the same direction as $\boldsymbol{B}$, contrary to diamagnetic materials where $\boldsymbol{M}$ is antiparallel to $\boldsymbol{B}$. Analogous to bound charges, when materials become magnetized interior regions cancel out. Although there will be regions in the outer range where a current strip exists, namely a bound current. Besides this, polarization currents, caused by the polarization of the dielectric materials and free currents caused by the motion of free electrons, need to be taken into account. So, ending up with a total current density where each part adds up: $\boldsymbol{j} = \boldsymbol{j}_{bound} + \boldsymbol{j}_{free} + \boldsymbol{j}_{polarization}$ (Thidè, 2011; Feynman et al., 2010; Everett, 2013; Kansu, 2013).

By following these considerations, the electric and magnetic fields are transferred to a pair of fields already incorporating effects of macroscopic matter: The electric displacement $\boldsymbol{D}$ and the magnetizing field $\boldsymbol{H}$. This is reasonable, because including $\boldsymbol{D}$ and $\boldsymbol{H}$ simplifies the differentiation of charges and currents, proven in many textbooks, i.e., Thidè (2011) and Feynman et al. (2010). In general, these fields obey a non-linear relationship but when the response of the homogeneous, isotropic material can be assumed linear, the relationship between them simplifies to the constitutive relations:

$$\boldsymbol{D} = \epsilon_0 \boldsymbol{E} + \boldsymbol{P} = \epsilon \boldsymbol{E}, \tag{2-3a}$$

$$\boldsymbol{B} = \mu_0 \boldsymbol{H} + \boldsymbol{M} = \mu \boldsymbol{H}, \tag{2-3b}$$

with ϵ being the electrical permittivity and μ the magnetic permeability. Summarizing, when considering the interaction of electromagnetic fields with matter, commonly the macroscopic formulation of Eq. (2-2a) - (2-2d) are considered where Gauss' and Ampère's law are modified. In these expressions only the free charge and current densities are contained, see Eq. (2-4a) and (2-4b).

$$\nabla \cdot \boldsymbol{D} = \rho_{free} \tag{2-4a}$$

$$\nabla \times \boldsymbol{H} = \boldsymbol{j}_{free} + \frac{\partial}{\partial t}\boldsymbol{D}. \tag{2-4b}$$

2-1-2 Material Properties

In geophysical and NDT surveys various types of materials are encountered each obeying special electromagnetic behavior depending on their electrical and magnetic properties. These material characteristics are intensive properties since their magnitude stays unchanged when the size of the system is varied. Three relevant properties are: Permittivity in farad per meter (F/m), conductivity in siemens per meter (S/m) and permeability in henry per meter (H/m). The latter, being the property of matter that affects the magnetic field, describes the ability of a material to support the formation of internal magnetic fluxes when it is subjected to an external magnetic field. It is a complex number where the real part accounts for the storage of magnetic energy and the complex part for the dissipation component (Baker et al., 2007). So, it characterizes the induced magnetization. Since free space permeability is a constant $\mu_0 = 4\pi \times 10^{-7}$ H/m, the permeability of any material can be expressed in terms of this value: $\mu = \mu_r \mu_0$. Thus, the resultant factor μ captures the effect of the material and the relative permeability μ_r is simply the ratio of the materials permeability to that of free space. Commonly, most compounds present in the subsurface do not exceed the vacuum permeability and thus for these materials μ_r is approximately equal to one. Concrete is typically classified as non-magnetic. Other encountered materials, like steel, are predominantly ferromagnetic and exceed μ_0 drastically. As steel is an iron alley it shows a large permeability. However, the value of μ_r strongly depends on the purity of iron in it. For types of steel used for structural applications a typical value is 100 whereas pure iron would reach values up to 200000 (Ellingson, 2018; Soutsos et al., 2001).

Dielectric permittivity is a property concerning the electrical field and relates the displacement field to the external electrical field. Thus, it reveals information about the reorientation of electric dipoles in response to the applied field and accordingly measures the degree of polarization. Energy is dissipated due to heat transformation in response to the charge movement (Baker et al., 2007). On the other hand, energy is stored because the charges move when subjected to an external applied field until an internal EM field has built up that balances the fields. Again, this parameter is a complex function with energy storage defined by the real component and energy dissipation by the complex component. In addition, in the presence of rapidly changing electrical fields, $\boldsymbol{P}$ cannot change instantaneously, producing a phase difference between the external field and the polarization vector. This adds up to the imaginary part of the permittivity described above (Everett, 2013). Nevertheless, permittivity is the primary diagnostic physical property for Ground Penetrating Radar as changes within an investigated material result in reflection or transmission. As for the permeability, the real part of the permittivity is commonly related to its value in free space $\epsilon_0 = 8.8542 \times 10^{12}$ F/m. From this it follows that the relative permittivity ϵ_r is simply the ratio of both (Ellingson, 2018; Everett, 2013). For materials that encounter significant loss, the complex dielectric permittivity must be considered but is often neglected. Liquid water ($\epsilon_r \approx 81$) shows the maximum relative permittivity for materials found in geophysical and NDT surveys. Contrary, values for soil vary between 3 (sand) and 40 (clay), depending on the percentage of water in the pores. The values for concrete vary strongly depending on humidity, composition and operating frequency. For a dry concrete a relative permittivity of 5 can be chosen rising up to 14 for a saturated concrete. With an increase in frequency ϵ_r starts to decrease slightly. However, for high frequencies (above 200 MHz) the values reach a plateau and thus the dependency becomes neglectable (Soutsos et al., 2001).

The electrical conductivity σ quantifies a material property representing the ease with which charges can move through the material subjected to an external electrical field. Materials with a large conductivity easily allow electric current to flow whereas in low conductives the resistance to current flow is large. It is a key element in *Ohm's law* which relates the electrical field to the current density for linear materials via $\boldsymbol{j} = \sigma \boldsymbol{E}$. It has many contributions and is strongly dependent on the water content of the material. Common values encountered range from 0 S/m for free space, to water $0.005 - 0.050$ S/m, up to iron 1×10^{7} S/m. Most soils show values in a range between 1×10^{-4} S/m (dry) and 1×10^{-1} S/m (wet). Concrete, being an insulator, shows relatively low values (0.025 S/m), again depending on humidity, composition and frequency. In contrast to ϵ_r the frequency sensitivity cannot be disregarded and therefore, the conductivity can take values ranging from close to zero to 0.1 S/m (Ellingson, 2018; Soutsos et al., 2001).

In general, the discussed material properties are tensors and thus vary in different directions. Moreover, they are strongly frequency dependent as time-varying fields are utilized, resulting in complex functions. However, for simple isotropic, comparatively homogeneous materials, being in the focus of this work, and assuming instantaneous behavior the simplified relations presented are valid (Ellingson, 2018; Everett, 2013).

2-2 Electromagnetic Waves

In order to understand the propagation of electromagnetic waves, it is useful to first put together the theory from section 2-1. Consider a uniformly moving, positively charged particle and its associated field lines which are always directed perpendicular to its surface. As field lines start at the particle and extend radially outwards to infinity *kinks* must exist if the particle was accelerated for only a certain time $t_a > 0$ where $c \approx 300\,000$ km/s is the speed of light in vacuum. This is because the field lines for distances larger than ct_a remain unchanged before the acceleration took place and the field lines for distances smaller than ct_a must follow the field lines of the particle after being accelerated. Since $\boldsymbol{E}$ must be differentiable due to Eq. (2-2a) the field lines cannot show discontinuities at the border, they have to be connected via kinks (Visser, 2012). This disturbance of the electric field lines is attended by a changing magnetic field, both moving outwards from the accelerated particle at the speed of light forming an electromagnetic wave. Thus, whenever charged partials, i.e., electrons, are accelerated or decelerated in form of a time-varying electric current or due to accelerated charges, time-varying electric and magnetic fields in form of electromagnetic waves are generated. The radiated energy originates from the charged particle and is therefore lost by it (Visser, 2012).

Focusing on dipole antennas, Figure 2-1 illustrates schematically how the electric field propagates away from a wire (black lines) consisting of two conductors with positive and negative charges. For simplicity only the radiation in one plane is presented, however, it should be clear that this is rotationally symmetric around the axis of the dipole. Typically, the two rods are much shorter than the wavelength of the applied alternating current (AC) source. A common type of dipole antenna is a *Half-wavelength* antenna where the total length of the dipole is approximately one-half of the wavelength and the corresponding rods have a length of one-quarter each. In Figure 2-1 the waveform below the dipole displays the current as a function of time, each instance is annotated by a black dot on the curve. Right after the source was turned on, an electrical field starts to build up (a) pointing in downward direction since the upper rod gets positively and the lower rod negatively charged. As the currents increases further, the strength of $\boldsymbol{E}$ increases as well. Until in (b) it reaches its maximum for $t = T/4$ where the field component from (a) has already propagated to a distance of $\lambda/4$. At this point, no fields exist for distances larger than $\lambda/4$. After this time step, the time change of the current changes its sign as can be seen in the waveform representing the current source and thus the charges are accelerated in the opposite direction resulting in field lines pointing upwards (c). Again, they travel a distance of $\lambda/4$ while the charge diminishes. In addition, the upwards directed field lines from $t < T/4$ also travel another quarter wavelength. After one-half of the period has past, the two rods become charge free resulting in zero net-charge,

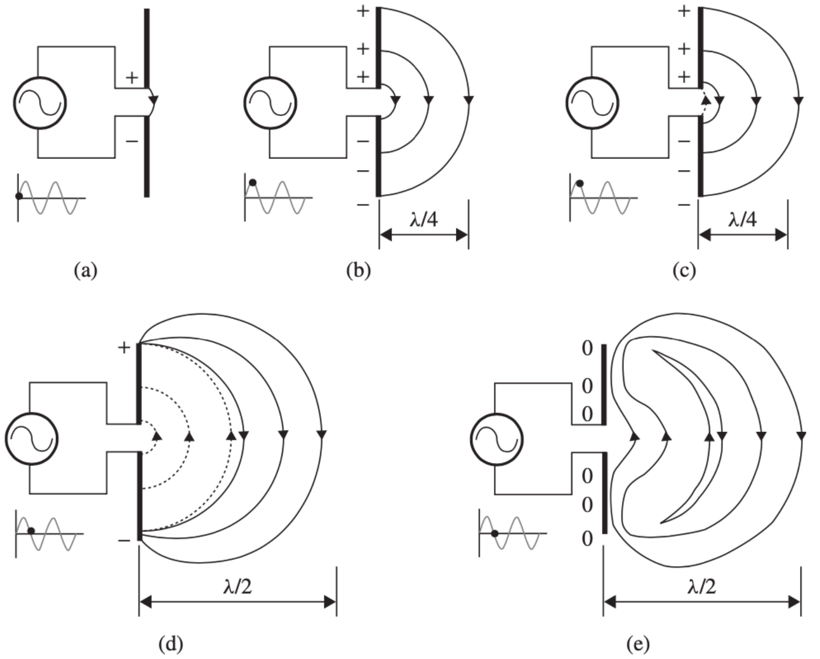

Figure 2-1: Schematic illustration of the detachment of electromagnetic waves from a dipole antenna when an alternating current source is applied: For (a) $t = 0$, (b) $t = T/4$, (c) $t = T/4 + \Delta t$, (d) $t = T/2$ and (e) $t = T/2 + \Delta t$ (Visser, 2012).

see Figure 2-1 (e). Owing to this, the field lines do not need to act perpendicular to the dipole anymore and thus, unite together and detach from the antenna to couple into space and propagate outwards (Visser, 2012; Balanis, 2016).

So far, only the generation of the electric field was described, however due to Ampère's law this AC source results in a magnetic field. Following Figure 2-1 (a), the magnetic field encircles the wire in counterclockwise direction forming closed loops around the dipole source. This generated magnetic field changes orientation each half cycle.

This succession of changing electric and magnetic fields where one induces the other as described by Maxwell's equations (2-2a) - (2-2d) causes a movement through space. Also, both fields are perpendicular to each other as well as to the direction of propagation which results in a *transverse wave* (Annan, 2012). Likewise, for the detection of electromagnetic waves the incoming wave induces oscillating currents in a receiver antenna. The frequency of the EM wave determines the frequency of the oscillating currents (Balanis, 2016; Feynman et al., 2010; Urone and Hinrichs, 2012; Visser, 2012).

2-2-1 Electromagnetic Wave Equation

Besides the quite practical approach to consider a dipole antenna, Maxwell's equations can be used to derive the wave equation for electromagnetic waves. For simplicity, consider Eq. (2-4a), (2-2b), (2-2c) and (2-4b) in an infinitely extended isotropic and homogeneous medium which is neutral, thus without free charges ($\rho = 0$). In order to uncouple these equations, it is helpful to raise their order yielding to uncoupled second order partial differential equations.

Applying the curl which is a vector operator $(\nabla\times)$ to both sides of Eq. (2-2b) and (2-4b), using the constitutive equations from Eq. (2-3a), (2-3b) and Ohm's law $j = \sigma E$ and by using the vector identity $\nabla \times \nabla \times \boldsymbol{A} = \nabla(\nabla \cdot \boldsymbol{A}) - \nabla^2 \boldsymbol{A}$ results in Eq. (2-5a) and (2-5b).

$$-\nabla^2 \boldsymbol{E} = -\mu \frac{\partial}{\partial t} (\nabla \times \boldsymbol{H}) \tag{2-5a}$$

$$-\nabla^2 \boldsymbol{H} = \nabla \times \left(\boldsymbol{j}_{free} + \frac{\partial}{\partial t} \boldsymbol{\epsilon E} \right) \tag{2-5b}$$

On the right-hand side, both curls are substituted by Eq. (2-4b) and (2-2b), respectively. For Eq. (2-5b) additionally Ohm's law is needed to substitute the free charge current. Following this leads to the uncoupled, homogeneous wave equations (see Eq. (2-6a) and (2-6b)) describing a wave traveling at some speed $v = 1/\sqrt{\mu\epsilon}$. Obviously, both fields satisfy the same wave equation (Feynman et al., 2010; Balanis, 2012; Dobbs, 1985).

$$\nabla^2 \boldsymbol{E} - \sigma\mu \frac{\partial}{\partial t} \boldsymbol{E} - \epsilon\mu \frac{\partial^2}{\partial t^2} \boldsymbol{E} = 0 \tag{2-6a}$$

$$\nabla^2 \boldsymbol{H} - \sigma\mu \frac{\partial}{\partial t} \boldsymbol{H} - \epsilon\mu \frac{\partial^2}{\partial t^2} \boldsymbol{H} = 0 \tag{2-6b}$$

2-2-2 Solution to the Wave equation

Solutions to the electromagnetic wave equations (2-6a) and (2-6b) exist in different forms, including spherical and plane waves. Each of them is defined by their distinct shape of the phase front. When the surfaces of constant phase are infinite parallel planes perpendicular to the direction of propagation, it is said to be a plane wave. As a result, the intensity of plane waves remains constant as it propagates in space. However, this means that there is no spreading in energy. In contrast, a spherical wave shows a constant phase on a sphere of any radius r obeying a solution similar to $\psi(r,t) = f(r - ct)/r$ where c corresponds to the velocity in free space and t for any time instance. This clearly indicates that the amplitude of this wave type decreases with $1/r$. As solving the electromagnetic wave equation for spherical waves requires the transformation to spherical coordinates, which is quite useful for point-like sources and for the far-field of dipole antennas, the reader is referred to Feynman et al. (2010), Balanis (2012) or Hum (2020). Indeed, EM waves can be modeled as locally planar waves when the dimensions of the source are relatively small compared to the scale on which the wave is observed (Ellingson, 2018; Annan, 2012).

Considering EM waves as spherical or planar is valid only in the far-field region where the inverse distance terms dominate. The separation into near-field and far-field is based on the different field characteristics. In the near-field of the antenna the description of the electromagnetic field is very complex due to inductive processes. Thus, one of the fields dominate depending of the source type. In case of the described dipole antenna it is the electrical field. Many researchers have tried to identify the boundary between the two field regions and a common approximation is $\lambda/(2\pi)$. Contrary, in the far-field the two fields exist due to the mutual induction processes and typically none of them dominates over the other. In this region the wave is assumed to act as a spherical wave and as stated can be approximated by a plane wave. Thus, when seeking for a solution to the wave equation, the simplest waves to consider are plane waves (Dobbs, 1985; Feynman et al., 2010; Greiner, 1998; Millard et al., 2002; Huang et al., 2020).

Plane Time-Harmonic Waves

Since both fields satisfy the same wave equation (see Eq. (2-6a) and (2-6a)), the approach is similar and the solution to the other can be obtained by an interchange. Indeed, the solution for the magnetic field can be derived from the Maxwell's equations as soon as the solution for $\boldsymbol{E}$ is derived. Assuming a plane (time-harmonic) electromagnetic wave propagating in the $\pm z$-direction: $\boldsymbol{E}(z,t) = E_0 exp\,(ikz - i\omega t)\,\hat{\boldsymbol{y}}$ and $\boldsymbol{H}(z,t) = H_0 exp\,(ikz - i\omega t)\,\hat{\boldsymbol{x}}$, with the wavelength $\lambda = 2\pi/k$ and the time-period $T = 2\pi/\omega$ (Everett, 2013). By inserting this Ansatz into the wave equation in (2-6a), this leads to the complex wavenumber $k = \sqrt{\epsilon\mu\omega^2 + i\mu\omega\sigma}$ which can be separated into its real and imaginary component $\alpha + i\beta$, see Eq. (2-7a) and (2-7b) (Everett, 2013). The wavenumber can be understood as the spatial frequency as it measures the number of cycles per unit length and is also known as the propagation constant.

$$\alpha = \omega\sqrt{\frac{\mu\epsilon}{2}}\left[\sqrt{1+\left(\frac{\sigma}{\omega\epsilon}\right)^2}+1\right]^{\frac{1}{2}} \tag{2-7a}$$

$$\beta = \omega\sqrt{\frac{\mu\epsilon}{2}}\left[\sqrt{1+\left(\frac{\sigma}{\omega\epsilon}\right)^2}-1\right]^{\frac{1}{2}} \tag{2-7b}$$

From this it follows that the solution for the electric field can be written as:

$$\boldsymbol{E}(z,t) = E_0 exp\,(-\beta z)\,exp\,(i\alpha z - i\omega t)\,\hat{\boldsymbol{y}}. \tag{2-8a}$$

Separating the solution into two exponential terms yields to the two components contributing to the propagation of the EM wave. The presence of the attenuation factor β, related to the imaginary part of the wavenumber, results in the term $exp\,(-\beta z)$ describing the rate of decay of the amplitude with increasing depth z (Everett, 2013). Therefore, it accounts for the dissipation of energy. As this component vanishes for small σ, the conductivity is the underlying cause for attenuation. The reciprocal of the attenuation constant β is referred to as *Skin depth* δ which is the depth of propagation at which the amplitude of an electromagnetic wave has decreased to 37 % of its original amplitude, so it reduced by a factor of $1/e$. In this term e is the so-called Euler's number. Indeed, for GPR measurements the Skin depth is less significant to consider.

On the other hand, the phase constant α accounts for the propagation of the EM wave and thus it is related to the propagation velocity $v = \omega/\alpha$, see Eq. (2-9a). As the conduction current $\boldsymbol{j}_c = \sigma\boldsymbol{E}$ accounts for the attenuation via dissipation of energy, the displacement current $\boldsymbol{j}_d = \epsilon\partial\boldsymbol{E}/\partial t$ is responsible for the propagation via energy storage (Alteköster, 2004; Dobbs, 1985; Everett, 2013; Balanis, 2012).

$$v = \sqrt{\frac{2}{\mu\epsilon}}\left[\sqrt{1+\left(\frac{\sigma}{\omega\epsilon}\right)^2}+1\right]^{-\frac{1}{2}} \tag{2-9a}$$

Two cases can be considered: Lossless $\sigma = 0$ and lossy $\sigma \neq 0$ materials. For the former, the conduction currents become zero resulting in the displacement currents dominating and hence, no energy is dissipated. At once, the imaginary part of the propagation constant β vanishes and thus in a perfect lossless dielectric no attenuation takes place and the electrical field reduces to $\boldsymbol{E}(z,t) = E_0 exp\left(i\alpha z - i\omega t\right)\hat{\boldsymbol{y}}$. In addition, the propagation velocity can be simplified to Eq. (2-10a) with c corresponding to the propagation in free space. Concluding, in a lossless dielectric the propagation of EM wave depends mainly on the two material properties ϵ_r and μ_r. However, typically we consider non-magnetic materials and, in this case, the relative permeability can be set to one. Revealing that, in media where the relative permittivity is lower, the velocity is higher.

$$v = \frac{c}{\sqrt{\mu_r \epsilon_r}} \tag{2-10a}$$

Contrary, lossy materials have an imaginary wavenumber and due to this they encounter attenuation with the strength being determined significantly by the conductivity of the medium. For lossy materials the conduction currents become more important conditioned by σ. For too large conductivities energy diffusion dominates and thus, no wave propagation takes place.

Summarizing, for GPR to work in the wave regime the ratio between the displacement and the conduction current should be larger than one ($\omega\epsilon/\sigma \gg 1$). In the wave regime the Skin depth can be calculated by an approximation of $0.0053\sqrt{\epsilon_r}/\sigma$. Owing to the inverse dependency on the conductivity the Skin depth decreases drastically with an increase in σ and thus the EM wave cannot travel far in conductive environments. Although experience shows that the Skin depth is not a quantitative measure for the depth of penetration. As typically every substance under investigation shows some loss, the conduction currents cannot be ignored. Owing to that, dispersion of electromagnetic waves occur as the propagation velocity becomes frequency dependent. Substantially, $\omega\epsilon/\sigma \gg 1$ is not only achieved when the conductivity is small but also if large frequencies are operated (Alteköster, 2004).

2-2-3 Wave Polarization

Electric and magnetic fields are described as vectors because at any given point in space and at any given time they have a magnitude and a direction. As the electromagnetic wave propagates, the magnitude and direction of these vectors change as a function of time and space. This so-called *polarization* can occur in different directions and forms. Commonly, EM wave polarization refers to the direction of the electric field vector. If one of three orthogonal basis vectors of a Cartesian coordinate system are directed along the axis of propagation z, the electrical field can be separated into another pair of orthogonal vectors E_x and E_y. The magnitude and phase relation between them define the type of polarization: Linear, spherical and elliptical, whereas the former two types are simply special cases of elliptical polarization (Figure 2-2). In the simplest case of linear polarization, the vector does not switch the orientation for any time or space coordinate. Thus, it simply moves along a straight line, see Figure 2-2 c) and when considering the orthogonal electrical field vectors no phase-difference other than a multiple of π occurs. Within linear polarization a distinction is made between vertically and horizontally polarized waves which describes the electrical field vector oscillating along the vertical or horizontal axis, respectively. A linear polarized wave can be created by using a dipole antenna or by passing the wave into a polarizer.

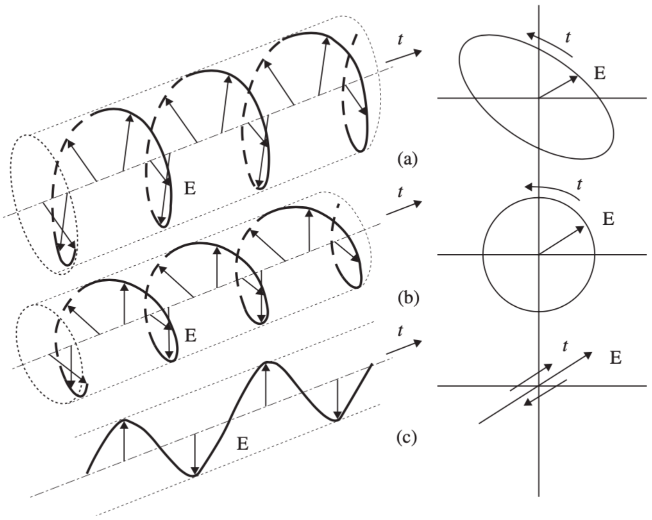

Figure 2-2: Polarization of the resultant electrical field vector ($\boldsymbol{E}$) due to the phase difference between the pair of orthogonal vectors: a) elliptical polarization, b) circular polarization and c) linear polarization (Visser, 2012).

As an example, for such a linear polarized wave consider the plane wave solution in Eq. (2-8a) for the electric field. Here, $\boldsymbol{E}$ can only alternate in the direction of y and thus the electric field is linearly polarized in the y direction. Now consider a phase difference of $\pi/2$ between the two orthogonal components but assume the amplitudes to be equal. In this case circular alternation occurs and thus the electrical field vector sweeps out a circle. Moreover, for non-similar magnitudes or if the phase difference is not exactly $\pi/2$ elliptical polarized waves are encountered. This describes that the electrical field vector traces out an elliptical locus in space. Polarization of the incident electromagnetic wave strongly influences the response measured at a receiving antenna. In order to ensure sufficient energy returned to the antenna, one additionally has to consider target polarization, see Section 2-3-3. Typical types of antennas utilized in GPR measurements are dipole or bow-tie antennas which transmit linear polarized waves. Here, the electrical field vector is oriented along the dipole axis of the antenna (Radzevicius and Daniels, 2000; Altekoster, 2004).

2-3 Boundary Conditions

When the electromagnetic wave impinges at an interface between two media characterized by differences in their material properties the EM components are discontinuous. To investigate how the two fields change at any of the possible boundary surfaces, i.e., dielectric to conductive, less dielectric to more dielectric or vice versa, *Boundary Conditions* (BC) can be derived:

$$E_1^{||} - E_2^{||} = 0, \tag{2-11a}$$

$$H_1^{||} - H_2^{||} = \boldsymbol{K}_f \times \hat{\boldsymbol{n}}, \tag{2-11b}$$

$$D_1^{\perp} - D_2^{\perp} = \sigma_{free}, \tag{2-11c}$$

$$B_1^{\perp} - B_2^{\perp} = 0. \tag{2-11d}$$

Accordingly, it is convenient to start with the Maxwell's equations in integral form and to separate the field quantities into components which are tangential or normal to the interface. Consider a two homogeneous media with ϵ_1, μ_1 and ϵ_2, μ_2: Evaluating Faraday's law over a loop enclosing the boundary but having a width which is neglectable results in a zero surface integral. In addition, the line integral over the closed loop shows no contribution from the two sides, resulting in the boundary condition for the tangential component of $\boldsymbol{E}$ in Eq. (2-11a): The tangential component of the electrical field is always continuous over a boundary. Similarly, Ampère's law in integral form reduces to the general boundary condition in Eq. (2-11b) where $\boldsymbol{K}_f$ represents the surface current density and $\hat{\boldsymbol{n}}$ is the unit vector perpendicular to the interface. Thus, the tangential component of $\boldsymbol{H}$ is only conserved by an amount which is proportional to $\boldsymbol{K}_f$. To derive the boundary conditions for the normal components a thin box which slightly extend in both media yielding to a neglectable flat volume has to be considered. Owing to this Eq. (2-11c) is derived, showing that the normal component of the electrical displacement field is only continuous as the surface charge σ_s vanishes. Applying a similar approach to Gauss' law for magnetic fields yields to the boundary condition in Eq. (2-11d) which describes, that the normal component of the magnetic field varies continuously across a boundary (Griffiths, 2013; Ellingson, 2018; Greiner, 1998). For a detailed derivation with graphical illustrations of the problems the reader is referred to Griffiths (2013) or Ellingson (2018).

2-3-1 Reflection, Refraction and Transmission

An EM wave impinging on a boundary between two linear media (no frequency change) gets reflected back in medium 1 or refracted into medium 2. For simplicity only the derivation for the electrical field is presented. In the general case of oblique incidence which describes the plane wave impinging at the boundary at an angle of θ_I, the plane wave from Section 2-2-2 ($\boldsymbol{E}_I(z,t) = \boldsymbol{E}_0^I exp\left(i\boldsymbol{k}_I\boldsymbol{r} - i\omega t\right)$) breaks into a reflected wave traveling in medium 1 ($\boldsymbol{E}_R(z,t) = \boldsymbol{E}_0^R exp\left(i\boldsymbol{k}_R\boldsymbol{r} - i\omega t\right)$) and a refracted wave propagating into medium 2 ($\boldsymbol{E}_T(z,t) = \boldsymbol{E}_0^T exp\left(i\boldsymbol{k}_T\boldsymbol{r} - i\omega t\right)$) where $\boldsymbol{r} = (x,\ y,\ z)$, see Figure 2-3. The angle of the reflected and refracted waves are referred to as θ_R and θ_T, respectively.

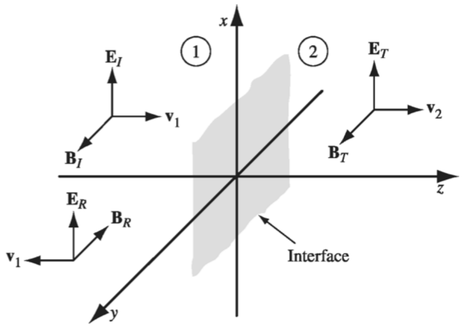

Figure 2-3: EM wave at normal incidence (index I) with its corresponding electrical fields $\boldsymbol{E}$ and magnetic fields $\boldsymbol{H}$ in a medium with velocity v_1. This gives rise to reflected (index R) and transmitted wave (index T), propagating in a medium with v_2 (Griffiths, 2013).

All three waves show the same angular frequency ω as linear materials are considered. Thus, following $\omega = kv$ the wavenumbers (k_I, k_R and k_T) are related via the velocity (v_1 and v_2) in the associated medium. Because the boundary condition in Eq. (2-11a) and (2-11c) have to be satisfied, the exponential factors must be equal and as a result $\boldsymbol{k}_I\boldsymbol{r} = \boldsymbol{k}_R\boldsymbol{r} = \boldsymbol{k}_T\boldsymbol{r}$ at $z = 0$ needs to hold. Separating the components into x and y contributions and assuming that the incident wave vector $\boldsymbol{k}_I$ is oriented such that it lies in the xz-plane ($(k_I)_y = 0$) leads to: $k_I \sin(\theta_I) = k_R \sin(\theta_R) = k_T \sin(\theta_T)$. From $k_I v_1 = k_R v_1$ the law of reflection follows, stating that the angle of incidence (θ_I) is equal to the angle of reflection (θ_R). The law of refraction also known as *Snell's* law results similarly from $k_I = k_R = v_2/v_1 k_T$ and relates the angle of incidence with the angle of transmission. For low loss dielectrics Snell's law is presented in Eq. (2-12a). It shows that when $\epsilon_1 > \epsilon_2$ the angle for the refracted wave is larger than for the incident wave and thus, spreads towards the horizontal (Griffiths, 2013).

$$\sqrt{\epsilon_1}\sin(\theta_I) = \sqrt{\epsilon_2}\sin(\theta_T) \tag{2-12a}$$

The ratio of the energy of the incident to the reflected wave is called reflection coefficient R (Balanis, 2012). For the simplified case of an ideal dielectric and under normal incidence ($\theta_I = 0$) the reflection coefficient approximates to Eq. (2-13a) revealing information about polarity changes of the amplitude. Due to losses R becomes quite complicated for non-ideal dielectrics (Blindow and Kirsch, 2009). Figure 2-3 schematically shows an arbitrary interface lying in a Cartesian coordinate system with the plane wave at normal incidence. Otherwise, the orientation of the electrical field vector relative to the plane of incidence becomes important. Following Figure 2-3, the combined fields in the first medium must satisfy the fields in the second medium. In addition, only contributions parallel to the boundary exist. Consequently, only the tangential boundary conditions need to be evaluated and following Griffiths (2013) this results in the reflection coefficient in Eq. (2-13a). The ratio between the relative permittivity of two interfacing media determines whether the amplitude is reversed or not. If ϵ_2 is larger than ϵ_1 the reflection coefficient in Eq. (2-13a) becomes negative and thus, a reversal of the amplitude in form of a 180° phase shift occurs (Blindow and Kirsch, 2009; Alteköster, 2004; Annan, 2001).

$$R = \frac{\sqrt{\epsilon_1} - \sqrt{\epsilon_2}}{\sqrt{\epsilon_1} + \sqrt{\epsilon_2}} \tag{2-13a}$$

Another fundamental information is obtained from R: Only a fraction of the incident wave gets reflected back to the surface dependent on the relative permittivity of the media and thus can be recorded by the receiver antenna (Annan, 2001).

Reflection From a Buried Conductor

As many objects in GPR application are highly conductive, the reflection coefficient from Eq. (2-13a) cannot be used to determine the properties of the reflection and transmission. Basically, considering large conductivities ($\sigma \to \infty$) in Eq. (2-9a) reveals that the propagation velocity of the electromagnetic waves in such media vanishes. As a result, no propagation can take place.

For a more sophisticated proof follow Griffiths (2013): A perfect conductor ($\sigma \to \infty$) causes a totally reflected wave as the boundary conditions of the electrical field imply. In addition, the boundary condition for the incident and reflected wave suggests a 180° phase shift for the reflected wave.

2-3-2 Scattering and Diffraction

Scattering occurs at localized heterogeneities with a dimension being small compared to the wavelength of the EM wave or at rough surfaces. In general, scattering and diffraction describe that an electromagnetic wave incident on a localized object results in the movement of electrical charges (Osipov and Tretyakov, 2017). Owing to this, a scattered or diffracted wave is created which strongly decreases the intensity of the incident wave and therefore decreases the energy left to travel in the element. This applies to concrete, where irregular shaped coarse aggregates or a large amount of fine aggregates are incorporated to increase the stiffness of the material. Although, the changes in the material properties are relatively small and thus the reflection coefficient in Eq. (2-13a) reveals that the scattered energy will be quite small. In addition, scattering happens at reinforcement bars or tendon ducts in prestressed concrete. Diffraction from discontinuities of reflectors become important, i.e., at the edge of structural elements. As Annan (2012) describes, the scattering response as a function of the size of the object can be separated into three regions showing different behavior. Within the first region the returned energy increases monotonically until the objects dimension is in the order of the excitation wavelength: $\lambda \approx 2\pi R$ with R the radius of the scattering object. For larger dimensions the energy starts to oscillate in amplitude due to the transit time of the created currents, referred to as Mie response. The optical response is described by objects with dimensions that exceed the wavelength by a factor of at least ten $10\lambda < 2\pi R$ resulting in the scattering cross section approximately equal to the geometrical cross section (Blindow et al., 2007; Annan, 2012). Following from this classification, the operating frequency should be large in order to create strong backscattered energy from the target cylinder. However, the EM wave is also sensitive to aggregates within the concrete and thus if the frequency is chosen too large, the excitation wavelength is so small that undesired scattering from a large range of dimensions masks the target reflections. Indeed, in order to increase the signal-to-noise ratio the excitation wavelength should be chosen such that it is considerably larger than the size of the heterogeneity: $\lambda > 2\pi R$ (Annan, 2012; Blindow et al., 2007). In Germany, the size of the aggregates incorporated in concrete varies typically between ≈ 0 mm and 32 mm (DIN EN 12620:2008-07, 2008; Stehno, 1981). For the largest aggregate and a relative permittivity of 6.25 for concrete, the center frequency should be chosen larger than 40 MHz (Annan, 2012).

2-3-3 Target Polarization

Elongated objects such as reinforcement bars or prestressing ducts introduced in Chapter 4 are typical targets for geophysical surveys. Thus, studying the interaction with EM waves is crucial in order to understand the GPR reflection patterns. Commonly, antennas used for GPR emit linearly polarized waves where the polarization direction is primary in direction of the dipole axis. Hence, the polarization direction for an isotropic medium can be modified only by changing the orientation of the antenna (Baker et al., 2007). When the polarization of the scattered wave is perpendicular to the long axis of the receiving antenna, polarization mismatch occurs. Thus, no signal from the localized object creates currents in the antenna (Radzevicius and Daniels, 2000). As the GPR survey conducted for this study only considers common offset data with a small antenna separation (see Section 3-2), it can be assumed that only backscattered ($\theta_R = 180°$) energy has to be investigated (Radzevicius and Daniels, 2000). Cylindrical objects scatter energy depending on the polarization of the incident wave. Accordingly, the polarization of the backscattered signal strongly depends on the scattering characteristics of the subsurface heterogeneity and on the polarization of the transmitter antenna relative to the long axis of the cylinder. For detecting conductive cylinders, two fundamental considerations have to be made: First, strong coupling must occur in order to re-emit enough energy. Second, the backscattered energy must contain sufficient amount of energy polarized parallel to the receiver antenna dipole axis (Radzevicius and Daniels, 2000).

To investigate the effect of target polarization it is convenient to separate the impinging

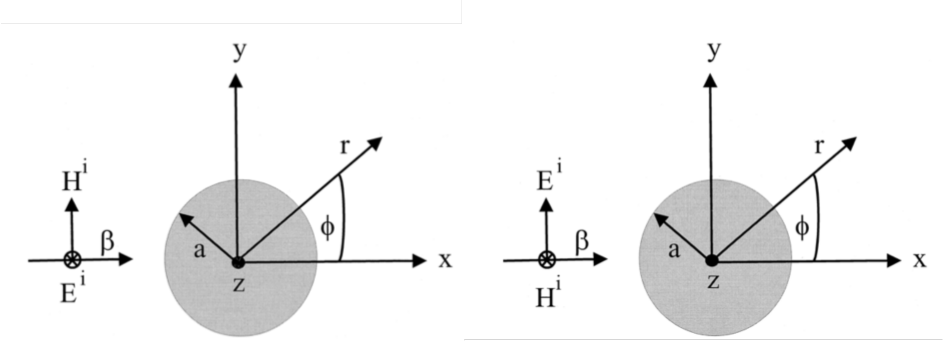

Figure 2-4: Two cylinders in Cartesian coordinate systems. $\boldsymbol{E}_i$ and $\boldsymbol{H}_i$ are the incident electrical and magnetic fields, β is the propagation direction, ϕ the scattering angle and r the radial distance from the cylinder. Left, shows the $\boldsymbol{E}$-parallel polarized wave impinging on the cylinder with radius a, originating from an antenna with its dipole axis parallel to the long cylinder axis. Right corresponds to $\boldsymbol{E}$-perpendicular which is obtained when the dipole axis of the antenna is oriented perpendicular to the long axis of the cylinder (Radzevicius and Daniels, 2000).

electrical field into an $\boldsymbol{E}$-parallel and an $\boldsymbol{E}$-perpendicular component, both shown in Figure 2-4. The left diagram, $\boldsymbol{E}$-parallel excitation, is obtained when the long axis of the antenna (equal to the polarization direction of the incident $\boldsymbol{E}$ field) is oriented parallel to the long axis of the cylinder. Though, for $\boldsymbol{E}$-perpendicular they have to be oriented perpendicular to each other. When the EM wave impinges at the scattering object it interacts with the charges on the surface obeying the boundary conditions introduced in Section 2-3. Analyzing them shows, that the tangential component of the electrical field has to be continuous across the boundary. Consequently, an $\boldsymbol{E}$-parallel incident wave which has a strong polarization component parallel to the long axis of the cylinder, sufficiently couples with it. Moreover, nearly no change in polarization occurs, namely depolarization, as the impinging electrical field of an $\boldsymbol{E}$-parallel polarized wave is aligned with the long axis of the cylinder (see Figure 2-4). In addition, the scattered EM wave is again mainly polarized in the direction of the long axis and thus, parallel to dipole axis of the receiver. Concluding, considerable energy reaches the receiving antenna from the secondary radiator, enabling the detection of the conductive cylinder (Everett, 2013).

In the second case, an $\boldsymbol{E}$-perpendicular wave reaches the scatterer (compare Figure 2-4) with a significantly smaller tangential component. Owing to this no strong coupling occurs and even if small currents are induced, they flow preferentially in the direction of the long axis of the cylinder. Again, this current flow results in a re-radiated field parallel to the long axis of the cylinder. Though, as the receiver antenna is oriented parallel to the transmitter, the backscattered energy acts perpendicular to the direction of the dipole axis of the receiver. As stated before, polarization mismatch for linear polarized waves occurs if the antenna dipole axis is perpendicular to the polarization of the incoming wave. Thus, for this type of setup the cylinder cannot act as a strong secondary radiator and it cannot be detected easily (Everett, 2013).

Obviously, the strength of the scattered field depends on the induced currents and therefore on the size of the conductive cylinder. Figure 2-5 shows the dependency on the radius R for the two components in form of the *Scattering Width* (SW) both normalized to the wavelength.

This SW is derived from the *Radar Cross-Section* (RCS) for 2D objects which is a measure of the cylinders ability to reflect the incident energy in the direction of the receiver antenna Knott (1993). Accordingly, it is the ratio between the power density of the scattered field $\boldsymbol{E}_S$ at the recording unit and the power density of the incident field on the cylinder $\boldsymbol{E}_{inc}$. Due to the cone-like shape of the distributed power in the material, the spreading factor $(4\pi R^2)$ is included in the RCS. For both, $\boldsymbol{E}$-parallel (green) and $\boldsymbol{E}$-perpendicular (blue) polarizations the re-radiated energy increases as the radius of the conductive cylinder becomes larger, see Figure 2-5. However, in the case of $\boldsymbol{E}$-parallel, SW is following a straight line and always shows larger backscattered energy than the $\boldsymbol{E}$-perpendicular polarization. Contrary, $\boldsymbol{E}$-perpendicular oscillates due to the constructive and destructive interference of the creeping wave around the cylinder (Roberts, 1994). For large enough radii the reflection interface increases and thus, the SW of the $\boldsymbol{E}$-perpendicular polarization approaches the green straight line as the backscattered energy of $\boldsymbol{E}$-parallel and $\boldsymbol{E}$-perpendicular become comparable. Consequently, for a 2 GHz signal within concrete with $\epsilon_r = 6.25$ and a corresponding wavelength of 60 mm the typically encountered range of normalized radii is below 0.7.

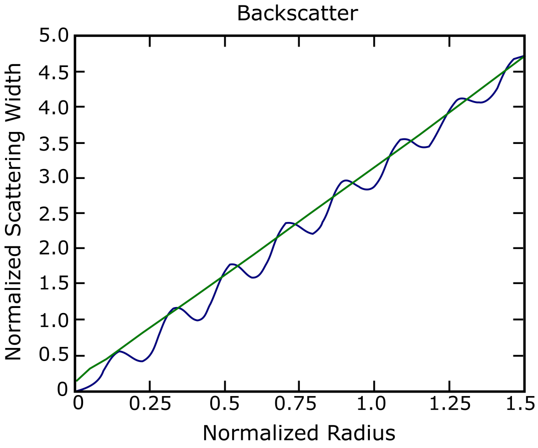

Figure 2-5: Scattering Width for a conductive cylinder in either $\boldsymbol{E}$-parallel (green curve) or $\boldsymbol{E}$-perpendicular (blue curve) polarization as a function of cylinder radius r, both normalized by the wavelength λ, modified after Radzevicius and Daniels (2000).

Since metallic and therefore conductive cylinders are in the focus of the study, other objects are only slightly covered here, but an extensive discussion can be found in Radzevicius and Daniels (2000). The above discussion for induced currents due to $\boldsymbol{E}$-parallel or $\boldsymbol{E}$-perpendicular excitation, holds also for cases when the electrical permittivity of the embedded cylinder is larger than for the surrounding materials. Nevertheless, the SW as a function of the radius becomes more complex showing additionally local minima. For surveys with low-dielectric cylinders such as air-filled plastic pipes within a high-dielectric surrounding, the above discussion does not hold. Indeed, when considering the scattering width both components highly oscillate but still increase for larger radii. It is conspicuous that for those kind of environments $\boldsymbol{E}$-perpendicular works best (Radzevicius and Daniels, 2000).

Concluding, the above discussion showed that a maximum backscattered energy is obtained, when the incident electrical field is parallel to the long axis of the conductive cylinder, emphasizing that in order to detect a cylindrical conductor with arbitrary radius, the $\boldsymbol{E}$-parallel mode should be utilized (Roberts, 1994; Radzevicius and Daniels, 2000; Sahamitmongkol, 2010; Everett, 2013).

Chapter 3

Ground Penetrating Radar

One of the most widely used geophysical methods is Ground Penetrating Radar utilizing short pulses of radiowaves at certain frequencies. It is designed to deliver high resolution results allowing to investigate the shallow subsurface of the earth or building materials. Thus, GPR has different fields of application: Geological, archaeological, engineering and non-destructive testing are usually separated due to their distinct difference in operating frequencies. This Chapter introduces the fundamental principle of the GPR method with additional focus on survey design and the different antenna orientations with their respective purposes. The formation of the characteristic reflection pattern for cylindrical objects, i.e., reinforcement bars and tendon ducts, is discussed in the end of the Chapter.

3-1 Fundamentals

Ground Penetrating Radar in its simple time-domain form, transmits high frequency electromagnetic pulses via the transmitting antenna (TX) into a material under investigation. Based on this, it responds to contrasts in electromagnetic properties, such as the dielectric permittivity ϵ and the electrical conductivity σ. Traveling at a velocity v (see Eq. (2-9a)), primarily dependent on the relative permittivity of the medium and therefore often approximated by Eq. (2-10a), the short pulses eventually get reflected back to the surface, scatter at discontinuities or at buried objects, or simply transmit further into the object (Annan, 2012). Thus, the velocity is the main controlling parameter for retrieving information from GPR data. In any case, the direct and reflected amplitudes are captured by a second antenna, the receiver antenna (RX). Hence, a basic GPR system consists of two antennas one transmitting the EM energy and one receiving it. Representing the recorded energy as a function of traveltime, is referred to as *trace* or *A-scan*, see Figure 3-1. Traveltime describes the time it takes the wave to travel the path from TX to RX including reflections at boundaries. Following Section 2-3-1, reflections from horizontal interfaces can be assumed to follow the reflection and transmission coefficient for low loss dielectrics. The former determines whether a polarity change is expected: When the wave encounters a boundary between material 1 with ϵ_1 and material 2 with $\epsilon_2 > \epsilon_1$ this yields to a negative reflection coefficient R and thus results in a reversed polarity. Therefore, evaluating the reflector with regard to polarity, gives information about the relative permittivity ratio between two media. However, as discussed additionally in Section 2-3-1, the reflection from a conductive body always shows a 180° polarity change (Griffiths, 2013).

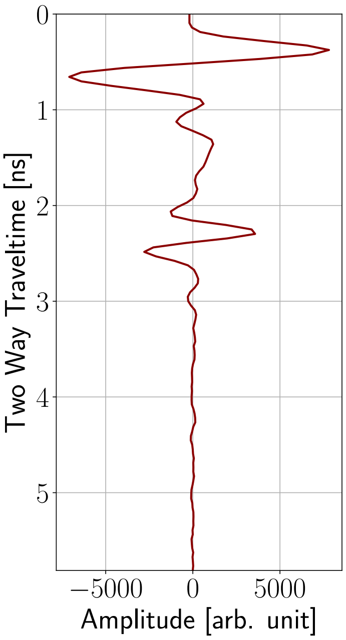

Figure 3-1: Example trace of a GPR survey at a concrete specimen where the direct wave is showing the maximum amplitude (< 1 ns). The reflection from a tendon duct occurs between 2 ns and 3 ns.

The direct wave (first arrival) traveling through air from TX to RX, shows the strongest signal, see Figure 3-1 between 0 ns and 1 ns. This is, because the signal detected by RX experiences energy loss, along the propagation path resulting in a reduction of signal strength (Reynolds, 1997). However, depending on the material, the shape of buried objects and on the antenna orientation, the recording still contains desired energy, as can be seen in Figure 3-1 between 2 ns and 3 ns. As synthetic studies in Gierens (2020) have shown, the depth of embedded objects strongly influence the reflection pattern because shallow reflections can be masked by the direct wave. Strong reflectors close to the surface, i.e., reinforcement bars, eventually cause a large portion of the incident wave to be reflected depending on the spacing between them. High conductive materials, i.e., clay, will cause rapid attenuation of the EM wave which implies limitations on GPR capability for such environments. Nevertheless, in order to enhance deeper target reflections, further processing of the data has to be performed. Standard processing algorithms applied to GPR data include time zero removal, dewow, time gain, background removal and frequency filtering where the order of these steps is not fixed. Since each processing step changes the originally recorded data, it potentially affects the information contained in the data. Indeed, which process is actually applied to the data strongly depends on the data quality, on the requirements for interpretation and on the operator (Everett, 2013).

As the antenna is moved along a survey line the measured traveltimes are recorded as a function of surface position. Displaying the recorded signal for each position results in a so-called *radargram* or *B-scan*, see Appendix B-1 for an example. This representation shows specific magnitudes and shapes depending on the subsurface properties, i.e., for cylindrical objects it results in a hyperbolic shaped reflection pattern, further discussed in Section 3-3.

3-1-1 Total Path Loss

As the radiowave is propagating through a lossy dielectric material it experiences a reduction in signal strength due to many reasons. Generally, it has five fundamental contributions: Material loss, reflection/ transmission loss, scattering loss and spreading loss. Material loss describes the frequency dependent continuous loss of amplitude as the wave propagates in the medium, due to the exponential term discussed in Section 2-2-2. Indeed, signal attenuation is governed mainly by electrical conductivity. In case of concrete, the conductivity depends strongly on the moisture and on the salt content. For larger frequencies and larger conductivities, the attenuation constant increases.

Reflection or transmission losses occur each time when the wave encounters a boundary where it is either transmitted into the underlying medium or reflected back. Scattered signals from localized undesired objects additionally reduce the signal strength of target reflections. This becomes important in concrete with large aggregates compared to the wavelength of the signal. Furthermore, when the target object, i.e., a prestressing duct, is placed below a layer of conducting cylinders, scattering potentially mask the target reflection due to preceding reflection of the energy (Gierens, 2020). A fundamental decrease in amplitude comes from geometrical spreading due to the inverse dependency of the amplitude of a spherical wave on the distance from the antenna, introduced in Section 2-2-2. Materials which show a large velocity, i.e., air or low dielectrics, experience stronger spreading losses for a given time Δt than low velocity media as $v_{fast}\Delta t > v_{slow}\Delta t$.

3-1-2 Vertical and Horizontal Resolution

Commonly, when acquiring GPR data an indispensable aspect to consider is resolution, indicating how precisely an object can be detected, located and characterized. When talking about resolution, two separate terms are discussed: Vertical and horizontal resolution. Vertical resolution strongly depends on the pulse width Δt of the wavelet used as source signal. In order to distinguish between two reflected signals, the spatial separation between them must be large enough to result in a temporal separation being notably larger than the pulse width of the source signal. Otherwise the lower reflection might be masked by the upper reflection due to constructive and destructive interference (Reynolds, 1997). As a general rule, the pulse width of a signal should be kept small to increase the vertical resolution. Briefly stated in Section 3-2, source pulses consist of many frequencies with a center frequency f_c being the spectral maximum of the broad pulse spectrum. This center frequency usually determines the propagation of the signal in the ground or in the structural element. Pulse width and center frequency are inversely related, $f_c = 1/\Delta t$ which is the reason why lower frequency pulses are generate longer wavelets. In addition, the frequency bandwidth Δf is influenced by the width of the wavelet such that a decrease in Δt results in an increase in Δf (Everett, 2013). However, simply using high frequency antennas in all surveys would come at the cost of a small penetration depth due to stronger attenuation of high frequencies. In addition, as loss of high frequencies is dominant, the reflected wave does have a longer pulse width compared to the source wavelet. Indeed, concrete, due to its relatively high conductivity, acts as a low-pass filter (Reynolds, 1997). From the above considerations it follows that narrowing the pulse width, as desired, is obtained by wide-band GPR antennas and high center frequencies. However, a fundamental limitation of GPR is the tradeoff between resolution and penetration depth, determining f_c (Blindow and Kirsch, 2009). As a general rule, two reflectors can be clearly distinguished as their separation is larger than one quarter of the wavelength of the source signal ($\lambda/4$) (Reynolds, 1997; Blindow and Kirsch, 2009). This becomes important for example when reinforcement meshes are built in above the target cylinder as the. For measurements with a 2 GHz antenna and concrete with $\epsilon_r = 6.25$ the two events can only be distinguished when the separation between the rebar and the cylinder exceeds 15 mm.

Horizontal resolution arises from the cone-like shape of the radiated EM energy, see Figure 3-2. As the wave spreads from the TX towards the reflector, the main signal power lies within the first *Fresnel zone* which takes the form of an illumination ellipse. Following Blindow and Kirsch (2009) laterally distinguishing between reflectors requires a separation of at least the diameter of this zone: $d = 2\sqrt{\lambda^2/16 + \lambda z/2}$ (Reynolds, 1997). Accordingly, a small Fresnel zone is preferred to increase the horizontal resolution yielding to small wavelengths and high frequencies. In case of the 2 GHz antenna and a resultant wavelength of 60 mm for concrete, the diameter of the Fresnel zones simplifies to $d = 2\sqrt{225\ \mathrm{mm}^2 + 30\ \mathrm{mm} \times z}$. Accordingly, in order to distinguish between single rebars in reinforcement meshes with a concrete cover of 50 mm the spacing must be larger than 83 mm.

3-1-3 Antenna Types

An antenna is an instrument which radiates and detects electromagnetic energy, i.e., radiowaves, with an antenna type dependent directivity and bandwidth. In general, the antenna is characterized by its three-dimensional radiation pattern, representing how $\boldsymbol{E}$ changes as a function of the direction relative to the radar antenna revealing that the sensitivity disseminates outwards, often approximated as cone-like shape or beam. Accordingly, antenna directivity is a measure of the amount of energy radiated in a certain direction. While in air the antenna pattern is radially symmetric for a dipole antenna in the far field, the interaction with dielectric materials strongly affect the sensitivity. Different types of antennas for GPR application exist. Most commercially manufactured systems contain dipole or bow-tie antennas, both characterized by linear polarization and low directivity. By far the most widely used antenna type is the dipole consisting of two conducting thin rods and a feed terminal in the center between the rods discussed in detail in Section 2-2. The size of the antenna is mainly determined by the required center frequency of the transmitted signal. Commonly, the length is a multiple of half the wavelength (typically one $L \approx \lambda/2$) and therefore decreases as the frequency increases. Owing to this length dependency, the antenna is limited in frequencies to transmit and thus, dipole antennas are typically narrow banded (Visser, 2012). Bandwidth refers to the range of frequencies over which an antenna radiates energy and since GPR application requires large bandwidths in order to generate sharp peaks in time, GPR antennas have to be broad banded. Consequently, dipole antennas in their simple form are less efficient for GPR application (Benedetto and Pajewski, 2015). To overcome this, resistive loading is applied to the antenna which suppresses reflections from the end points and results in the radiation of a single impulse. Bow-tie antennas which are planar dipole-like sheets of metal in a bitriangular form with its feed point at the apex of the sheets, are angle dependent rather than length dependent. Due to the specific shape they employ multiple resonant lengths, i.e., the dipole resonant length plus additional ones on the sides, and therefore they radiate larger bandwidths than dipole antennas. Indeed, a bow-tie antenna has bandwidth limitations due to the abrupt termination at the ends (Daniels, 2009).

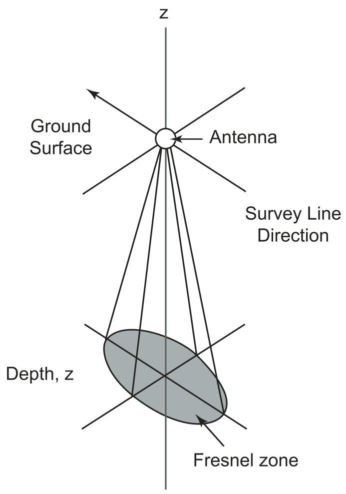

Figure 3-2: Schematic of the Fresnel zone which determines the horizontal resolution (Baker et al., 2007).

3-2 Survey Design and Parameters

Typically, GPR antennas employ a band of frequency ranging from 50 % above and 50 % below f_c. As discussed in Section 3-1-2 the center frequency strongly influences the depth of penetration and resolution. This is why NDT surveys commonly acquire data with relatively high frequencies ($\approx$ 100 to 3000 MHz) whereas GPR applied to geological problems is usually less interested in small heterogeneities but aims to obtain information from deep horizons and thus, lower frequency (less than 500MHz) surveys are conducted. Accordingly, the operating frequency must be fitted to the purpose and environment of each investigation. In addition, the center frequency has an impact on the temporal sampling, the time interval between two points in a GPR trace. Violating the *Nyquist sampling theorem* results in distortion of the discrete wave form, so-called aliasing. Based on this, the time interval should not be larger than one half of the time period of the maximum frequency occurring in the signal ($\Delta t < 1/(2f_c)$). Following the assumption that the largest frequency contained in the signal is 50 % above f_c, the data should be sampled at a rate related to $1.5f_c$ resulting in $\Delta t < 1/(3f_c)$. However, to be on the save side, commonly Δt is chosen even smaller to resolve also higher frequencies ($\Delta t = 1/\left(6f_c\right)$) (Annan, 2001).

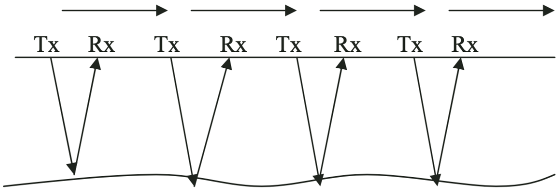

Figure 3-3: Common offset acquisition mode for GPR where a static antenna system is moved with a fixed increment along the surface. TX and RX refer to the transmitting and receiving antenna, respectively (Baker et al., 2007).

In general, two types of antenna setups are distinguished: Monostatic, where one antenna device is used to transmit and receive the EM wave and bistatic, where two antennas are used and one transmits whereas the other receives the energy. Typical collection modes for measurements are the *Common offset (CO)* and *Common Depth point (CDP)* configuration (Everett, 2013). CDP describes a bistatic mode in which the two antennas can be moved independently from each other and thus, the spacing between them can be altered. Indeed, the separation between TX and RX is incrementally increased around a common midpoint and thus, for a nearly horizontal reflector the reflection point in a certain depth is assumed to be fixed. By doing so, the operator gains information about the velocity and the thickness of the top layer medium by either evaluating the direct ground wave or the normal moveout velocity of the reflected wave (Everett, 2013).

Typically employed in surveys, common offset measurements illustrated in Figure 3-3 have a fixed antenna spacing (offset) for the entire measurement. As the set is moved at a fixed increment along the surface of the object the operator gains information about a nearly horizontal reflector. Acquiring data in the CO mode is best for detecting and locating buried objects such as reinforcement bars. The fixed system enables the operator to quickly acquire data along the surface which reduces the costs for a given survey as well as the uncertainty of antenna separation (Blindow et al., 2007; Reynolds, 1997). The orientation of the antennas relative to the survey line plays a huge role in survey design and is addressed in Section 3-2-1.

With regard to antennas there are two factors that need to be considered: Antenna separation and spacing. The latter, important only for bistatic measurements, has an impact on the wave path through the material as for larger spacings the wave has to travel a longer distance and therefore, it is subjected to attenuation for a longer time. Seldom considered but yet important, the separation can be adjusted such that the energy peak of the antenna's radiation pattern is directed to the target. Nevertheless, in most commercial GPR systems the antennas are manufactured in a closed box and thus either a second antenna box is added, or the separation cannot be altered. Spatial sampling however is key in order to avoid aliasing and with this to avoid losing structural information. This becomes important for dipping horizons or for embedded objects as they resemble a continuous reflector and the GPR can only get information at discrete locations. Targets will not be resolved if the spacing between two measurements is larger than defined by the Nyquist sampling theorem yielding to a spacing of less than one quarter of the wavelength of the EM wave in the corresponding medium (Milsom and Eriksen, 2003).

Another quite important survey parameter is the time window for which data at each position should be stored. To determine this parameter the depth (d) of the deepest object must be approximated. This is strongly coupled to the operating frequency because this determines the depth of penetration as well as on the EM velocity v inside the material. Accordingly, the time window should be at least $1.3(2d)/v$ (Annan, 2001).

3-2-1 Antenna Polarization and Orientation

In order to detect buried objects and eventually determine their position, shape and size, enough energy must be re-emitted by the object. Accordingly, the polarization of the antenna relative to the localized heterogeneities is key for getting a strong response, as discussed in Section 2-3-3. In analogy to this, it is common to distinguish the configuration with respect to the embedded object (Everett, 2013; Radzevicius and Daniels, 2000). However, this is impractical as in most surveys the direction and shape of the object is to be determined. Consequently, it is more convenient to define the orientation of the GPR antennas with respect to the profile direction. Since the topic of antenna orientation is controversial, different types of definitions exist and thus, the reader has to be aware when comparing results from different studies (Baker et al., 2007). As in GPR the electrical field is the field of interest, the nomenclature for this survey is adapted from Baker et al. (2007). Therefore, prior to describing actual antenna orientations it is advisable to understand the origin of the nomenclature by investigating antenna polarizations. In Figure 3-4 the two principal polarizations are presented. On the left, the electrical field vector pointing into or out of the paper, is contained in a horizontal plane (xy-plane) which is perpendicular to the plane of incidence (yz-plane). Whereas on the right side $\boldsymbol{E}$ is moving in the yz-plane and thus the electrical field is in a vertical plane parallel to the plane of incidence which is also in the yz-plane. For the former the term *E-horizontal (EH)* is used and for the latter *E-vertical (EV)*. Again, other names exist, i.e., Transverse electric (TE) and transverse magnetic (TM) or E-polarization and H-polarization. To point this out, the transmitter antennas generate both kind of polarizations. For example, see Figure 3-4: EH polarized waves are generated in the yz-plane and EV polarized waves in the xz-plane but due to antenna reciprocity only EH waves will be recorded.

After clarifying the terminology for antenna polarizations, the typically employed antenna orientations can be presented. Besides the orientation relative to the second antenna the orientation relative to the survey line is of much greater interest for most available antenna

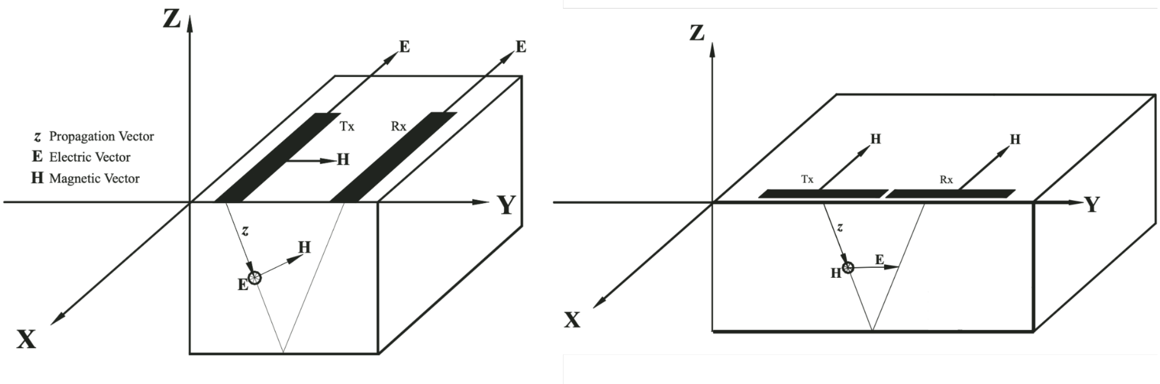

Figure 3-4: Different antenna polarization directions employed in GPR. E-horizontal (left) where the electrical field vector $\boldsymbol{E}$ is in a horizontal plane perpendicular to the plane of incidence and E-vertical (right) where $\boldsymbol{E}$ is in a vertical plane parallel to the plane of incidence. In both, the magnetic field $\boldsymbol{H}$ is always in a plane perpendicular to $\boldsymbol{E}$. (Baker et al., 2007).

types. In regard to the former, GPR antennas can be oriented in broadside (broad side towards each other), end-fire (end points towards each other) or crossed dipole configuration (broad sides perpendicular to each other). Broadside acquisition modes give rise to EH (Figure 3-4 Left) polarized data whereas in end-fire mode EV (Figure 3-4 Right) polarized data are obtained (Baker et al., 2007). Configurations with a crossed dipole are less common as most commercially available antennas are in a fixed casing and thus cannot be reoriented relative to each other.

More importantly, the antenna orientation can be given with respect to the survey line direction. Focusing on broadside antennas (EH polarization) as they show higher signal-to-noise ratios and are therefore used for the measurements in this work, reveals two cases: *Perpendicular broadside (PR-BD or PR)*, dipole axes parallel to survey direction and *parallel broadside (PL-BD or PL)*, dipole axes in right angles to survey direction (Baker et al., 2007). Comparing the result with Section 2-3-3 reveals that the individual response for both, perpendicular broadside and parallel broadside, from a conductive cylinder essentially depends on the orientation of the cylinder relative to the survey line.

3-3 Reflection Pattern for Conductive Cylinders

Reinforcement bars and tendon ducts, typically found in concrete, can be modeled as conductive cylinders where the threading surrounding the steel is neglected. When the antennas in common offset mode are step wise moved along the survey line perpendicular to a buried conductive cylinder (Figure 3-5 (a)), at some point the edge of the radar beam strikes the embedded object and scatters back to the surface antennas (Bungey et al., 1994). At this point the antenna-cylinder separation is larger compared to a positioning vertically above the cylinder. When the antennas approach further, the distance between TX-RX and the conductive cylinder decreases, and so does the traveltime. Directly above the cylinder the traveltime is smallest as the distance is smallest. From this point the apparent depth increases again until no reflection occurs anymore. Obviously, the signal strength is largest for the trace vertically above the cylinder, as the larger the distance a wave travels the more it gets attenuated in the material. Illustrated in Figure 3-5 (b), the amplitudes as a function of traveltime are plotted as function of the distance along the line, revealing a hyperbolic outline. To emphasize, the shape of the hyperbola depends on the radius of the cylinder, the depth underneath the surface, the orientation of the cylinder relative to the antenna and the relative permittivity of the medium. In general, the slope of the corresponding asymptotes is related to the propagation velocity of the medium surrounding the cylinder (Shihab and Al-Nuaimy, 2005; Utsi, 2017; Yuan et al., 2018).

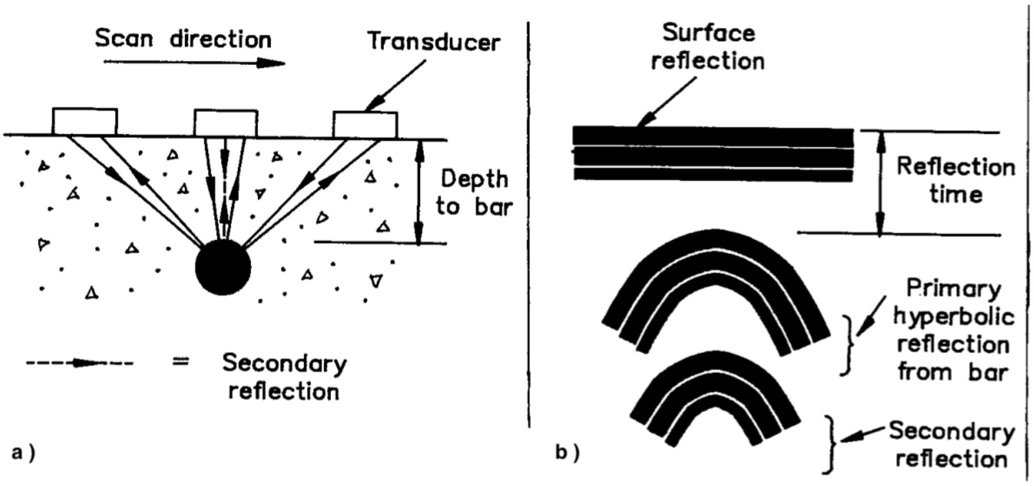

Figure 3-5: Schematic illustration of the formation of the characteristic hyperbolic pattern for scattering from an embedded cylinder (b). In a) antennas with a common offset are moved along the survey line approaching the cylinder. In b) the direct wave as first arrival and the primary as well as secondary (seldom actually recorded) reflections can be seen (Bungey et al., 1994).

Chapter 4

Reinforced and Prestressed Concrete

This Chapter provides the fundamental theory of nonreinforced, reinforced and prestressed concrete. In the end, a brief description of the tasks that are addressed in *Non Destructive Testing (NDT)* is given.

4-1 Fundamental Theory

Reinforced and prestressed concrete is a compound of concrete and steel and is used to overcome the two major weaknesses of simple nonreinforced concrete: It is brittle and has low tensile strength (Akroyd, 1962). Since structure design is a challenging and complex topic, this Chapter only covers the basics. For further information the reader is referred to the many textbooks that have been released about prestressed concrete, i.e., Akroyd (1962), Almeida et al. (2005), Geßner et al. (2016), Lau and Lasa (2016) and Naaman (2001).

Concrete is a mixture of four primary ingredients: Water, cement, fine as well as coarse aggregates, i.e., sand, gravel, or crushed rocks and other additives. In general, the key constituents are cement and water. Initially, cement, made by grinding crushed materials after being in a kiln for a certain time, is a loose powder which develops its strength by adding water to it. This is due to hydration which describes the process of water molecules being bonded to compounds of the cement and thus, becoming part of the cured cement (Akroyd, 1962). However, simply using cement would not make a good working material as some water which is not chemically fixed, dries out causing contraction of the total volume namely shrinkage. This would be undesired as it eventually introduces cracks and deformation. Accordingly, to overcome the shrinkage issue and to fill up the bulk of concrete by a cheaper material, aggregates are used as a filler yielding to an increased concrete strength (Akroyd, 1962). It is obvious that the more water is added the more easily the mixture can flow in the desired forms. However, this added workability reduces the strength of the cured concrete. This emphasizes, that modifying the mixture controls the concrete properties and finding a composition that fits the structures requirements is challenging. For further information on the topic the reader is referred to Akroyd (1962), Lau and Lasa (2016), Naaman (2001) and Zilch and Zehetmaier (2010).

Merely the properties of concrete in the hardened state are important for NDT problems addressed in this thesis, even though they are influenced by the properties in the construction state. Besides workability and durability, three fundamental properties that need to be considered in construction design are: Strength, creep and shrinkage (Akroyd, 1962). As discussed, shrinkage occurs as water in voids dissolves, eventually resulting in cracks and deformation. Long term loads on concrete, basically result in deformation increasing with time, which is called creeping. By far, the resistance to rupture is the most fundamental characteristic and the two types of stress considered are: Compression and tension. While concrete can easily be exposed to compressive forces, already very low tensile stresses will cause failure (Akroyd, 1962; Naaman, 2001; Zilch and Zehetmaier, 2010). Figure 4-1 on the top shows the resistance of simple concrete to loads: The top of the beam is subjected to compressive stress whereas the bottom experiences tensile stress. Thus, cracks occur at the bottom of the beam and propagate upwards until the beam fails. Clearly undesired, propagation of cracks happens quite rapidly with nearly no indication prior to the catastrophe (Zilch and Zehetmaier, 2010).

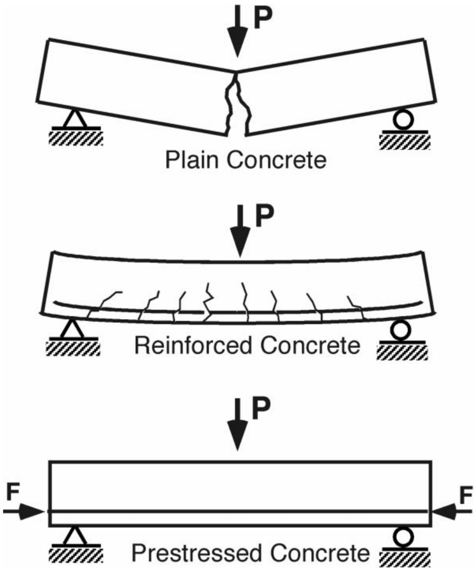

Figure 4-1: Comparison of nonreinforced (top), reinforced (middle), and prestressed concrete (bottom) with the help of a beam subjected to external loading. The plain concrete collapses without showing indications in advance, the reinforced beam builds cracks and carries the load by means of bending, the prestressed concrete carries the load without cracking and bending Naaman (2001).

As structural members rarely do only experience compression as indicated in the example with the beam, the need for compensating for low tensile strengths arises. By adding steel reinforcement bars, primarily where tensile strength is expected to reach an undesired value, a composite material where concrete mainly takes up compressive stress and reinforcement bars resist tensile stress is created (Naaman, 2001; Zilch and Zehetmaier, 2010). Nevertheless, Figure 4-1 shows another phenomenon: The beam bends and flexes under the applied load before it even fails giving rise to deformation. As steel lengthens with stress no significant tension can be taken up by the rebar until cracks occur (Geßner et al., 2016; Naaman, 2001).

A simple round, threaded steel rod commonly used as rebar allows the two compounds to deform almost equally when they are exposed to loads (Zilch and Zehetmaier, 2010). Typically, reinforcement bars are distributed in different depths and mainly in two orthogonal directions. By choosing a problem-specific rebar diameter (see Table 4-1) and density the size of the cracks can be influenced in a way such that a sufficient serviceability and durability is generated. Since it is essential for rebars to be surrounded by concrete to prevent corrosion, the largest aggregate has to be smaller than the reinforcement bar spacing (DIN EN 12620:2008-07, 2008). Besides the improved tensile strength reinforced concrete has a second advantage which becomes clear when comparing the top of Figure 4-1 with the reinforced bar in the middle. It is obvious that in the nonreinforced case the failure is not noticed by any cracks prior to it whereas in the reinforced beam the formation of cracks can be traced before a complete loss of the beam (Zilch and Zehetmaier, 2010).

In conclusion, rebars change the type of failure from a brittle mode where no warning occurs to a ductile mode where cracks in the concrete can indicate a weakness of the structure causing a complete loss of the construction in a later stage. Hence, prestressed concrete provides the possibility to identify the problem in order to prevent the catastrophe (Naaman, 2001; Geßner et al., 2016; Wu, 2006).

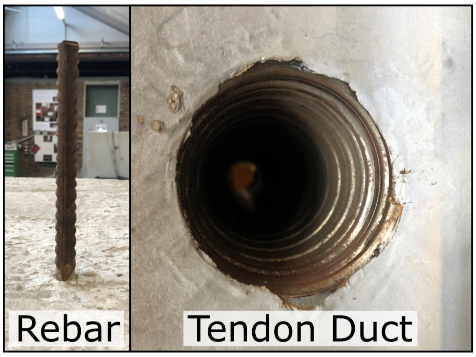

Figure 4-2: Picture of a typical reinforcement bar (∅ 12 mm) and tendon duct (∅ 65 mm).

In general, the design criteria for a construction is not only to withstand the load but also preventing deflection, hence providing serviceability. Motivation for this is primarily, that as cracks appear, it allows water or contaminants to infiltrate the concrete which could be the reason for reinforcement corrosion and hence for weakening of the element (Lau and Lasa, 2016). Furthermore, when structural members start to move, elements that are attached to it, can start to fall off being a huge safety concern. A simpler reason is perception: Deflecting structures do not give a feeling of safety. A load balancing system which uses prestressed steel rods to overcome the small load bearing capacity of nonreinfoced concrete and to prevent from cracking and deformation that occurs in simple reinforced concrete is therefore preferable (Naaman, 2001; Zilch and Zehetmaier, 2010). This balance is achieved by imposing a state of stress via tensioning of the steel rods, counteracting the effect of external applied loads. Thus, anchorage forces precompress the element which increases the compressive stress and decreases or even cancels the tensile stresses once the structural member is put into service (Almeida et al., 2005; Geßner et al., 2016; Zilch and Zehetmaier, 2010). Again, consider Figure 4-1, the beam at the bottom represents the prestressed structure. Contrary to the nonreinforced and reinforced cases, due to balancing the stresses the beam does not deflect when load is applied. Only if large tensile forces are applied to the element, cracks start to form (Naaman, 2001). Such internal stress leads to a much higher cracking resistance, improves the stiffness, reduces the amount of steel and concrete needed for the construction and finally increases the load bearing capacity for a given structure span and dimension (Almeida et al., 2005; Naaman, 2001).

Prestressing refers to the fact that the concrete is stressed prior to applying any load. Additionally, one commonly distinguishes between *pretensioned* and *posttensioned* systems. In this case the prefix corresponds to the moment of stressing relative to the concrete curing and hardening. Hence, an element is pretensioned when it is stressed before the concrete has hardened and posttensioned when it is stressed afterwards (Almeida et al., 2005; Naaman, 2001).

Table 4-1: Typical diameters of reinforcement bars and tendon ducts further described in the text (Sharma and Kind, 2018).

Type of Reflector	Diameter [mm]
Rebar	6 – 40
Tendon duct	50 – 130

In pretensioned concrete prior to casting the concrete, tendons are stressed and anchored to fixed bulkheads or molds. After hardening of the concrete, the applied stress is released and by the bond between the two materials the concrete gets compressed taking up the stress from precompression. Pretensioning allows factory production for parts of the construction and potentially reduces costs as standard cross-section elements can be tensioned by mass production (Almeida et al., 2005).

Posttensioned concrete, where the tendons are stressed after the concrete has reached the hardened state, is usually use in cast-in-place construction. In order to generate posttensioning, commonly metal ducts are used as place holder within the liquid concrete (Almeida et al., 2005; Zilch and Zehetmaier, 2010). After hardening the tendons can be placed inside the duct and by anchoring the ends at the concrete member stress is applied. Bonding is ensured by filling up the space in the duct with mortar grout, for example. This guarantees that the tendon force can be transferred throughout the entire length of the tendon. Another advantage of grouting is, that the tendons are protected from corrosion (Almeida et al., 2005).

Since steel tendon ducts are in the focus of this thesis, only posttensioned concrete is considered. Seldom, the tendon duct is made of plastic and not of steel (Almeida et al., 2005) which has a dramatic impact on the radar response since no total reflection takes place anymore (Section 3-3). Furthermore, for GPR investigations the main difference between steel reinforcement bars and tendon ducts is the difference in diameter, see Table 4-1 for examples.

4-2 Tasks for Non Destructive Testing

Civil engineering structures such as tunnels, bridges, buildings and the like, are often made from prestressed concrete. Eventually the elements start to degrade owing to initial defects, aging, environmental conditions, extreme loads like the increase in mobility, water infiltration and concrete cracking (Li et al., 2009; Wang, 2018). On occasion, fires and earthquakes additionally destroy the stiffness of a structural member (Li et al., 2009). These parameters influence the element such, that the concrete exceeds its purpose of design resulting in sustainably damaged elements. Methods to sufficiently evaluate the safety and durability of those facilities are key for maintaining important infrastructures. Any failure will not only imply the loss of the structure but also brings a significant damage to society and to economy (Wang, 2018). Since adaptive construction works should not destroy the element further, exact positions of embedded objects like rebars and tendon ducts are critical. However, construction plans are sometime not entirely available as they got lost or even irrecoverably destroyed (Dérobert et al., 2018). On the other hand, the plans eventually do not fit the actual built configuration due to several reasons. This means, that rebar meshes might be less dense, are smaller in diameter or in general that the objects are not perfectly in place. Moreover, due to corrosion of reinforcement the diameter eventually changes and thus the entire structure is not capable to take up the desired loads anymore (Lau and Lasa, 2016). Consequently, non-destructive testing is key to maintain infrastructures at low cost as it allows to illuminate the structural element without destroying it. Different methods for evaluating such problems exist. Indeed, GPR employed at relatively high frequencies is a common and efficient method to gain information about heterogeneities in concrete (Annan et al., 2002; Dérobert et al., 2018; Li et al., 2009). This is because GPR offers high resolution data for shallow investigations.

Chapter 5

Materials and Method

To assess the classification of reflectors in reinforced concrete, characteristic features of rebars and tendon ducts are determined. For this purpose, attributes were tested using data measured at four concrete specimens each having their distinct structure and thus providing a broad range of intrusions. Five data sets under controlled environments are considered: Scanner measurements create data with high spatial sampling rates while manual measurements conducted within this survey describe low spatial sampling rates. An exception is the data set E which was recorded on-site at a bridge in Northwestern Germany. The test specimens (A, B, C and D) are introduced in the beginning of the Chapter, followed by a description of the GPR acquisition system from *Geophysical Survey Systems, Inc. (GSSI)*. At the end of the first half, the data preparation for the attribute analysis is presented with special focus on the extraction of hyperbolic events within the data sets. The second part of this Chapter introduces attribute analysis and presents the approaches for this thesis.

5-1 Concrete Test Specimens

The considered concrete specimens, which were already fabricated in the laboratory of BAM, consist of various sizes of reinforcement bars and tendon ducts within different mixtures of concrete. Each specimen provides different concrete covers and diameters to address the influential effects on the GPR response. Figure 5-1 contains the schematic of the four specimens illustrating the structural diversity and the difference in concrete covers ($h = 30$ mm to $h = 240$ mm). The diameter range for rebars varies between 6 mm and 28 mm whereas the diameter for tendon ducts is in a range between 65 mm and 86 mm (see Appendix A for a summary). Accordingly, a sufficient evaluation of the correlation between certain attributes and element classes can be performed by taking geometrical properties into account. Limitations in diameters and concrete covers result from the availability of concrete specimens at BAM. Material parameters commonly encountered in reinforced concrete are already discussed in Section 2-1-2 and summarized in Table 5-1. Concrete with a relative permittivity of 6.25 leads to an EM wave traveling at a velocity of 120 mm/ns and when considering a conductivity of 0.025 S/m it obeys the wave regime assumption introduced in Section 2-2-2. On the other hand, steel with its strong conductive behavior results in total reflection of the EM wave.

Table 5-1: Material parameters of the commonly encountered compounds: Relative Permittivity (ϵ_r), electrical conductivity (σ) and relative Permeability (μ_r) (Gierens, 2020; Annan, 2001).

Material	ϵ_r	σ [S/m]	μ_r [Vs/Am]
Air	1	0	1
Concrete	6.25	0.025	1
Steel	∞	6×10^6	100

The 1200 mm × 1200 mm × 200 mm test specimen A contains upper and lower reinforcement with different diameters (10 mm and 6 mm) and mesh sizes (15 mm and 10 mm), see Figure 5-1a. As can be seen, both reinforcement meshes contain rebars in both directions on perpendicular grids. Obviously, due to the large concrete cover ($h = 164$ mm) the lower rebar mesh is of less interest for the survey. Only the upper mesh ($h = 30$ mm) is in a range which can be properly observed by the radar wave with the considered center frequency of 2 GHz. Additionally, a tendon duct is placed below the first reinforcement layer in the center of the element. A styrofoam sheet can be identified in the right half of the specimen. It is not important for this study as it does only cover part of the space below the first rebar layer and does not intersect with the tendon duct.

Within specimen B four tendon ducts with a diameter of 80 mm are incorporated in a block of 2000 mm × 800 mm with different thicknesses of 570 mm, 450 mm, 330 mm and 210 mm. Accordingly, the specimen has a step profile as indicated in Figure 5-1b: The back wall of the specimen appears at variable depth. Further, each of the prestressing ducts lie in a different depth below the surface.

In Figure 5-1c, a schematic of specimen C with a dimension of 2000 mm × 1500 mm × 500 mm is presented which is partially reinforced on both, front and back side and partially nonreinforced. A tendon duct is positioned in the center with a depth of $h = 160$ mm. Six styrofoam balls with different diameters and variable concrete covers are included. As these covers are quite thick, the response in the data will be rather small for the chosen frequency.

Since the aforementioned concrete specimens contain rebars in comparatively shallow depths and dense grids, concrete specimen D (1500 mm × 1500 mm × 660 mm) is considered because single rebars with different diameters in a depth range between 60 mm and 180 mm are installed (Figure 5-1d). This gives the opportunity to investigate the response from each rebar with nearly no interference from neighboring objects and low impact of the direct wave arrival.

As an exception to the measurements under controlled environments, real case data acquired at a bridge in Northwestern Germany (survey code E) are analyzed. The considered survey area has a dimension of 4000 mm × 700 mm where the long axes of the grid was oriented perpendicular to the long axes of the bridge. From construction plans it is expected that the data set contains reflections from reinforcement bars, tendon ducts and from hollow bodies.

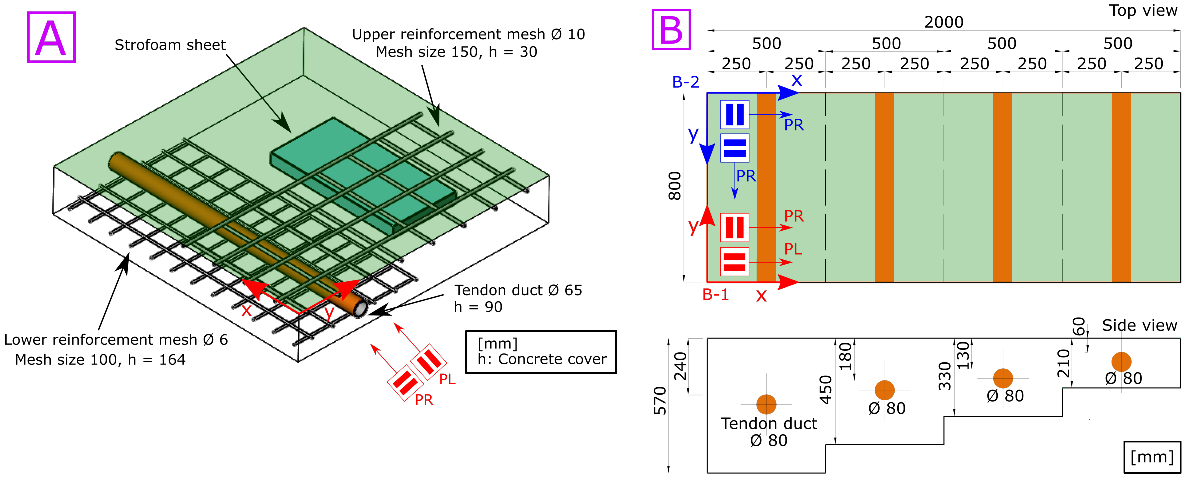

(a) Concrete specimen *A*.

(b) Concrete specimen *B*.

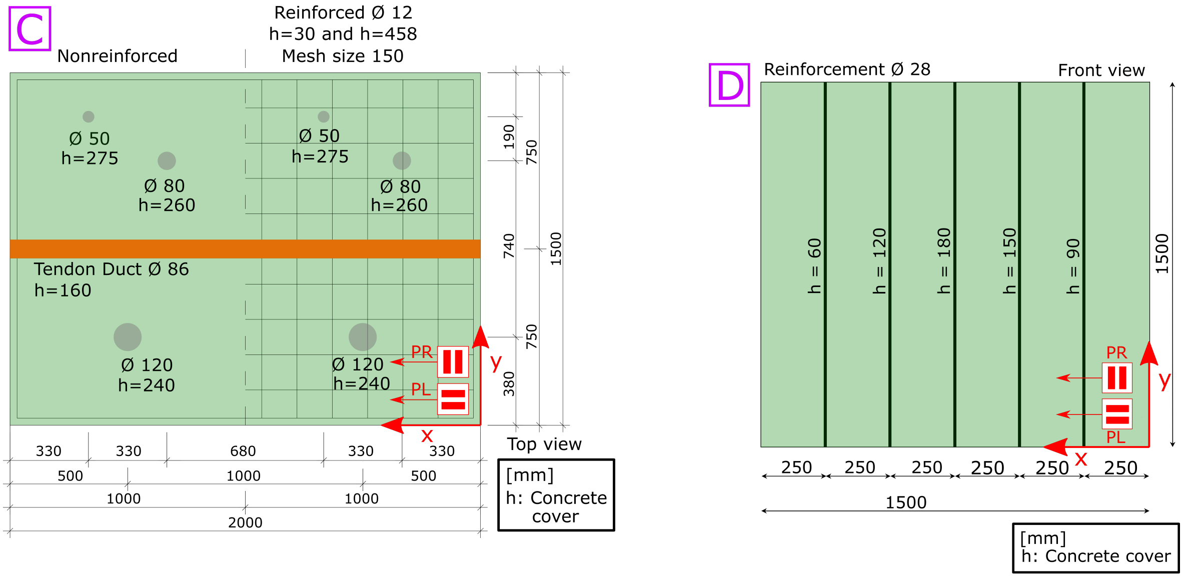

(c) Concrete specimen *C*.

(d) Concrete specimen *D*.

Figure 5-1: Schematic representation of the concrete specimens with the corresponding measurement coordinate system (red) and the antenna configurations in red for scanner measurements and blue for the manual measurement. The acquisition surface is marked in green; reinforcement bars are illustrated in black and tendon ducts in orange. The unit of the dimensions is in millimeter (mm).

5-2 Measuring System and Data Acquisition

Within this study, a GSSI SIR® 20 (SIR 20) measurement system employing a control unit connected via a cable to the laptop, was used to acquire radar data. The SIR 20 is able to work with different antennas in three acquisition modes: Survey wheel, free run (a predefined number of scans per second) and point mode (antenna is placed at a distinct location and one particular scan is performed). The former mode utilizes a wheel as distance encoder such that the collected A-scans have a constant spacing independent of the speed of the operator. Thus, this is the typical acquisition mode for common offset measurements. As required for proper GPR measurements, different parameters can be regulated within the system. See Section 3-2 for a further description of the parameters with respect to electromagnetic wave theory and Geophysical Survey Systems, Inc. (2017) for a description of SIR 20 settings. First, the time range (t_{max}) has to be set according to the relative permittivity (Eq. (2-10a)) and the desired depth of penetration ($2d = t_{max}v$). With the approximated EM wave velocity for concrete (120 mm/ns) and a time range between 6 ns to 12 ns, a sufficient depth range up to 360 mm and 720 mm can be investigated, respectively. As the depth of penetration is limited by attenuation and other losses (Section 3-1-1), large time ranges do not contain any desired energy. Thus, the considered time span is sufficient to cover the range of potential reflections. To digitize the radar signal, different sampling densities (number of samples per scan: n_{sample}) can be set: 128, 256, 512, 1024 and 2048. Selecting this number determines the temporal sampling interval via $\Delta t = t_{max}/n_{scan}$ which on the other hand has to fulfill the Nyquist sampling theorem ($\Delta t = 1/(6f_c) = 0.083$ ns for $f_c = 2$ GHz) as discussed in Section 3-2, yielding to a minimum number of samples of 73 for 6 ns and 145 for 12 ns. Further, the number of scans per second, meaning the speed at which the GSSI unit is collecting data, is a parameter influencing the acquisition speed in survey wheel mode but not the distance spacing. The parameter that actually determines the spatial sampling interval is the number of scans per meter which likewise should not exceed the Nyquist sampling interval (Section 3-2) leading to a maximum spacing of 15 mm with a wavelength of 60 mm for a 2 GHz signal in concrete. As larger frequencies and thus smaller wavelength are present in the signal, the spacing is commonly chosen smaller. Nevertheless, this value is quite small and thus, for measurements outside controlled environments it is typically only satisfied in inline direction but not for survey line spacing.

With the SIR 20 it is possible to acquire data in a three-dimensional (3D) block implying the collection of data in x- and y-direction. By presetting the maximum extend in each direction (x_{max} and y_{max}) and the spacing between the survey lines for both directions (Δx and Δy), the 3D mode enables the operator to quickly acquire data line by line due to an automatic termination at the end of each line and a time-saving relocation to the next line. Each survey line is stored with an incrementally increasing leading number. After completion of the measurement, the operator can choose to create a 3D data set resulting in a sequential combination of the individual files to a joint file. This has to be considered when importing the data. In both cases the file format for storing GSSI data is a binary format (*dzt*) containing header information, specifying the predefined survey parameters, and the data values.

Different types of data sets are investigated: Structure scanner measurements at a dense grid and manual measurements being closer to real case surveys. For each test specimen a series of structure scanner measurements with high spatial sampling rates are available and can be used for studying attribute capability. As these were collected from members of *BAM-Division 8.2*

(Non-destructive Testing Methods for Civil Engineering), the process of acquisition is only briefly described. The surveys were conducted using a structure scanner where the antennas with center frequency of 2 GHz were mounted on axes in both orientations: Parallel and perpendicular broadside, to be automatically moved precisely along parallel profiles in x-direction in meandering mode. This means, that after a B-scan is recorded the measurement direction is flipped compared to the initial direction. The amount of data points for each antenna orientation is equal, rarely the case for on-site data. For distance information along the profile, an encoder is attached to the drive motors of the horizontal and vertical axis registering a signal if the axis is moved similar to the functionality of a survey wheel (Schubert, 2011). By using a structure scanner an extraordinary high spatial sampling rate was achieved such that the Nyquist criterion is fulfilled for both directions. Finally, the individual data files were assembled to a single 3D data file. As the measurement grid and survey parameters are different for each survey, a summary of the parameters is presented in Table 5-2. The survey code is derived from the concrete specimen at which the measurements were conducted. Scanner measurements (A, *B-1*, C and D) are described by the abbreviation SC in the column describing the mode of acquisition and manual measurements are described by MA.

Table 5-2: Survey parameters of the measurements at the different concrete specimens where t_{max} refers to the time range, Δt to the temporal sampling interval, Δx to the spatial sampling interval in x-direction and Δy to the spatial sampling interval in y-direction. The abbreviation SC and MA describe structure scanner or manual measurements, respectively.

Survey code	Mode	t_{max} [ns]	n_{sample}	Δt [ns]	Δx [mm]	Δy [mm]
A	SC	6	256	0.024	2.5	5
B-1	SC	12	256	0.047	2.5	5
C	SC	10	256	0.039	2	10
D	SC	10	256	0.039	2	5
B-2	MA	12	512	0.023	PR: 5 PL: 50	PR: 50 PL: 5
E	MA	11	512	0.021	PR: 5 PL: 100	PR: 100 PL: 5

In order to generate data being closer to real case data acquisition a less dense manual measurement at the test specimen B was conducted, referred to as *B-2* in Table 5-2. The survey settings were handed over to the GSSI SIR 20, followed by a distance calibration to set the encoder wheel increment properly. A poster containing the survey grid was placed on the surface of the specimen (Figure 5-2). So, the antenna was moved along these lines which increases the spatial accuracy and decreases the acquisition time. For real case studies, acquisition time is a key element and thus, only data in PR orientation were acquired since PL requires to switch the position of the survey wheel relative to the antenna. To approximate the missing PL configuration, measurements in both x- and y-direction were conducted using the PR-BR orientation. As visualized in Figure 5-2 the PR orientation in y-direction yields to PL data in the x-direction. Commonly, the survey line distance is smaller than the inline sampling and thus, this results in a different spatial sampling interval for the two configurations, see Table 5-2.

The data set *E* was collected by the members of BAM Division 8.2 using a lifting platform to be able to perform the measurement from the bottom side of the bridge. Data were acquired using the SIR 20 with a 2 GHz antenna with the two polarizations achieved similar to the description for *B-2*. Thus, the spacing between the traces is dependent on the considered antenna orientation as described in Table 5-2.

5-3 Preprocessing

GPR data measured with the GSSI system are stored as binary file in *dzt*-format. Therefore, a function, according to Bertram (2017) originally developed for MATLAB and available at BAM-Division 8.2, was implemented in *Python* (Version 3.8.2) a programming language based on Van Rossum and Drake (2009), to convert the binary information to ASCII values. The python codes developed for the purpose of this thesis are summarized in Appendix C. As the received electromagnetic wave is passed on to the receiving electronics via a voltage signal, the stored amplitude values are related to the measured voltage although a conversion factor for SI units is unknown. Thus, the amplitude values are presented in arbitrary units (arb. unit) oscillating more or less symmetrically around the zero line. When importing the data, the function *readDZT.py* hands over the data and header values. Besides the relative or absolute path to the file, some additional parameters have to be predefined: The minimum and maximum coordinate of each axis and the spatial sampling rates as well as the center frequency of the operated antenna. Especially when importing a 3D data file, the manual input of the x and y coordinates is required as the values stored in the header are erroneous whereas for the two-dimensional (2D) files the coordinates can be extracted from the header.

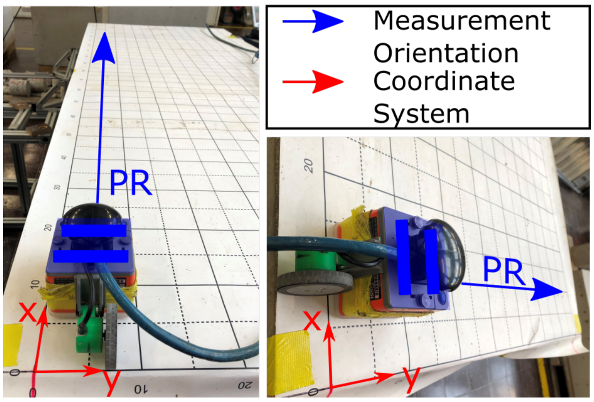

Figure 5-2: Process of data acquisition for measurement *B-2* to obtain the two polarizations for both coordinates x and y.

After importing the 3D data files for both antenna orientations the amplitude values are contained in a 2D matrix each. The first dimension corresponds to the time axis and the second axis is simply related to the trace indices of the radargram conjunction. Consequently, both data vectors have to be re-sorted into 3D matrices with the second dimension for the y-axis and the third dimension for the x-axis. By doing so, evaluating the data with respect to individual dimensions becomes easier. Owing to the meandering data acquisition mode for the four structure scanner data sets (A, *B-1*, C, D), every second horizontal (in x-direction) radargram has to be flipped. The processing for 3D files is summarized in the python code *A01_preprocess_3D_DZT*. Using *A01_preprocess_2D_DZT* imports individual files each containing a single transect in either x- or y-direction and results in a list object containing all radargrams. Therefore, the two functions *get_data_PR_lines.py* and *get_data_PL_lines.py* can be used to extract the horizontal and vertical measurements and sorts them into two individual 3D matrices for PR and PL.

As the processing should be kept small in order to reduce the computational overburden, only the absolutely necessary processing steps are applied. Since determining the depth of the buried object is not a primary subject of this study, time zero removal was not applied but could be easily added if required. Nevertheless, in order to suppress very low-frequency (wow) components a running average filter along the time axis in form of the arithmetic mean was calculated and subtracted from the data (*dewow.py*) (Szymczyk and Szymczyk, 2013; Cassidy, 2009). Sliding windows have to be determined carefully with respect to the center frequency and the time sampling rate of each measurement. For this survey the best results were achieved for a window size corresponding to three times the time period of the wave ($3/f_c = 1.5$ ns). However, dewowed data need to be considered carefully because this processing step sometimes causes undesired reverberations (Benedetto and Pajewski, 2015). In addition, background removal using the function *dir_rem.py* has to be considered to damp flat horizons and emphasize scattering and diffraction events within the section by constructing a reference trace and subtracting this from each trace in the radargram (Szymczyk and Szymczyk, 2013; Cassidy, 2009). For the surveys *A*, *B-1*, *D* and *B-2* the median over all traces within the radargram was chosen as reference trace, while for measurement *C* only a median over all traces resulted in a proper image. Consequently, continuous reflectors are eliminated which is desired for the direct wave but can be undesired if the target reflection resembles a horizontal reflector. Hence, this processing step is key when considering shallow reflections as in *A* and *C* because the direct wave has the strongest signal, masking target events.

5-3-1 Hyperbolic Reflection Specific Processing

Since high frequency data require small time sampling intervals, the computational effort for evaluating the entire data set is extensive. Accordingly, prior to investigating the reflection specific attributes a cutout containing the reflection event is created, exemplary illustrated in Figure 5-3 a) to b). This is achieved by either manually introducing the corners of the cutout after inspecting the radargrams or by interactively selecting a region of interest (*select_region.py*) within a separate window via an open source computer vision library (Bradski, 2000).

Obviously, the hyperbolic reflections like the schematic in Figure 5-4 are visible only if a profile is considered where the antennas are moved perpendicular to the cylindrical intrusion. In addition, the desired region should also be selected from a radargram with the antennas oriented parallel to the long axis of the cylinder. Then the function *A02_extract_reflector* automatically extracts the corresponding cutout for the second antenna configuration. Special care has to be taken when dealing with measurements where the amount of data differs for the two configurations, i.e., for most manual measurements. In this case the region of interest should be selected from the radargram with a denser sampling interval, see Figure 5-4 gray traces. As indicated by green traces in this figure, it is common that the second antenna orientation (typically PL), is only available on a fraction of the positions. Hence the corresponding cutout for the second orientation has to be evaluated with respect to overlap positions (green stars) using the *horiz_lines_PL.py* function.

Multiple reflections are extracted from the six data sets:

- Measurement A: Four rebars (A-Rebar 1 to A-Rebar 4) and one tendon duct (A-Duct).
- Measurement B-1: Four tendon ducts (B-1-Duct 1 to B-1-Duct 4).
- Measurement C: Six rebars (C-Rebar 1 to C-Rebar 6) and one tendon duct (C-Duct).
- Measurement D: Five rebars (D-Rebar 1 to D-Rebar 5).
- Measurement B-2: Four tendon ducts (B-2-Duct 1 to B-2-Duct 4).
- Measurement E: Six objects with supposedly unknown origin (E-Object 1 to E-Object 6).

A summary describing the coordinates of the cutouts is shown in Appendix A. Due to the interaction with the direct wave, the events A-Rebar, B-1-Duct 4, B-1-Duct 3, and C-Rebar consider background removed data.

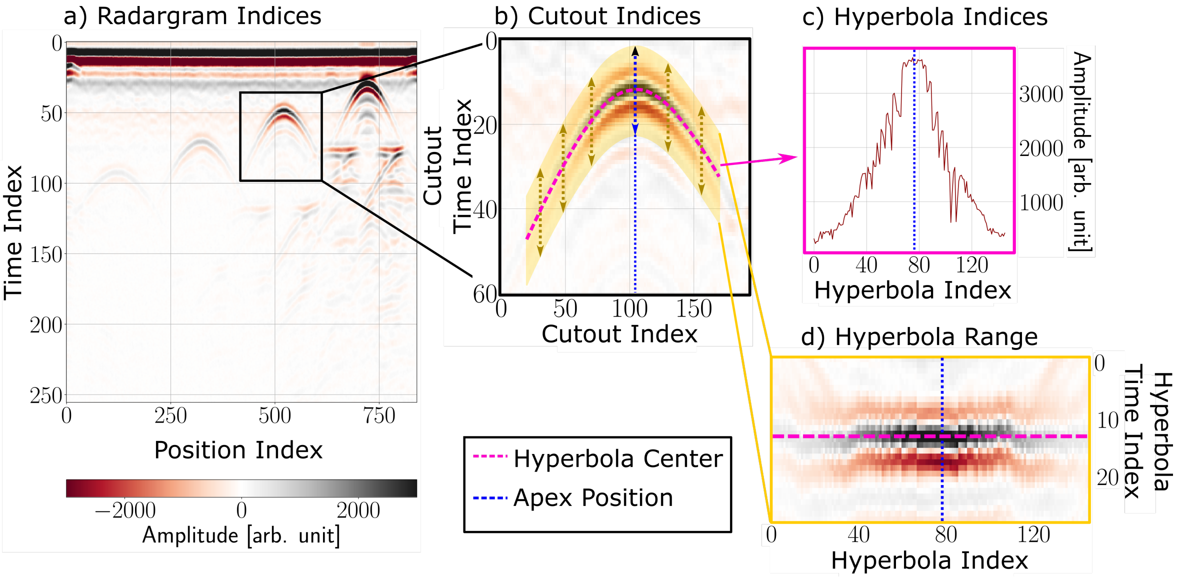

Figure 5-3: Flow chart of the data preparation, illustrated using the data from measurement B-1. a) The dewowed radargram with the cutout window for the reflection hyperbola specific attributes marked by a black rectangle and shown in detail in b) relative to the cutout indices. c) The amplitude variation along the selected hyperbola (pink line in b)) with the corresponding hyperbola indices on the x-axis. d) The time window around the hyperbolic reflection marked by a yellow shaded area in b). Again, the x indices are related to the hyperbola selection and the y indices to the time window.

For some attributes it is required to consider only the matrix entries corresponding to the hyperbolic signature. Many researchers have implemented algorithms to automatically find these positions (Yuan et al., 2018; Dou et al., 2016; Qiao et al., 2015). However, this is beyond the scope of this work as the position of the reflection is known from visual inspection or prior knowledge. Thus, within *A02_extract_reflector* the function *choose_hyperbola.py* which is based on the user interface toolkit contained in *Matplotlib* (Hunter, 2007) can be used to interactively select the reflection from a rebar or tendon duct within the cutout, see Figure 5-3 b). For this, the operator has to select the maximum amplitude (pink line) as this has proven to yield more stable amplitudes. The algorithm hands over the pixel position as long as the mouse button is pressed and thus repetitive time indices for each position index are created. As this resembles redundant information, the multiple time indices per position index have to be reduced to a single time index. Accordingly, the arithmetic mean of the time indices is computed and substituted within the function *reduce_ind.py*. The apex position is then calculated by determining the minimum time axis position of the selected hyperbola indices. Subsequently, the apex position is used to find a common center position for the hyperbolas of the two antenna orientations (*relate_indices_PR_PL_hypers.py*). Again, for unequal data points the indices of the first orientation have to be reduced to exist only at positions of overlap (Figure 5-4). Since it is more practical for further data evaluation, the position and time indices of the chosen hyperbola are relative to the cutout image (Figure 5-3 b)) while the apex position is relative to the hyperbola indices. Figure 5-3 c) indicates the hyperbola indices by showing the amplitude variation along the hyperbola. In order to increase the number of samples the program *A02b_extract_multiple_reflectors* takes the selected hyperbola and relates them to B-scans showing the same reflection (*create_set.py*). Due to interference with adjacent cylinders this is a quite complex process as some radargrams do not show a hyperbolic signal. Accordingly, pixels referring to time steps before and after are investigated with respect to the amplitudes to find the maximum amplitude in the considered time range (*find_yvals.py*). Next, using *hyperbola.py* and *fit_hyperbola.py* a hyperbola is fitted to the resultant indices to neglect too flat signatures.

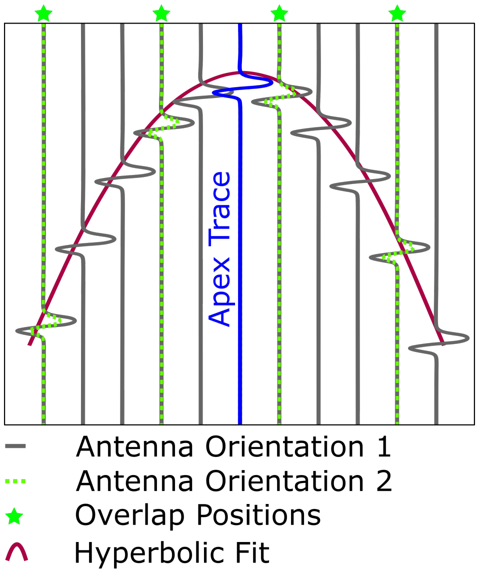

Figure 5-4: Schematic of a hyperbolic reflection (purple curve) for two antenna orientations with unequal spatial sampling rates; Gray traces indicate the first orientation with high spatial sampling rate, green corresponds to the second. Green stars highlight the positions where both orientations overlap. The blue trace marks the apex position.

After the hyperbola position is defined via the pixel indices, a range around the signature is extracted using the function *amplitude_range.py*. On the time axis, the range is defined by a window slightly larger than two times the pulse width $\Delta t = 1/f_c$ of the source signal symmetrically above and below the hyperbola center (the pink line in Figure 5-3 b) and d)). Along the x-axis the range relates to the selected hyperbola indices resulting in the image in d).

5-4 Classification Attribute Analysis

Besides amplitude and travel time analysis the need for more effective tools to enhance the interpretation quality of GPR signals arouse in recent years. Attribute analysis, visually enhancing areas of energy change via amplitude, frequency and phase information, is standard for seismic acquisition especially in the oil industry. They describe quantitative information extracted from the time history of each trace to enhance and isolate heterogeneities in the data set and by this increases the accuracy of subsurface interpretation. The derived features describe characteristics of the reflector and thus enable the distinction between the typical intrusions in concrete: Rebars and tendon ducts. Indeed, due to the more complex radar wave propagation, for GPR data attributes were seldom considered (Cassidy, 2009). Nevertheless, many researchers such as Böniger and Tronicke (2010); Zhao et al. (2013) and Castro et al. (2014) have successfully applied attribute analysis to GPR data in archaeological and geological context whereas Chang et al. (2009); Doğan and Turhan-Sayan (2016); He et al. (2009); Leucci (2012); Park et al. (2018); Dos Santos et al. (2014); Shihab and Al-Nuaimy (2005) and Utsi and Utsi (2004) use attributes to characterize hyperbolic patterns within GPR signals. Contrary, additional studies in Morris and Glisic (2017); Zanzi and Arosio (2013) and Bertram (2017) have shown that the encouraging results obtained in underlying studies are not promising enough to be used for real case applications as they yield to inconclusive results. In addition, the classification of these reflection patterns is not addressed and thus, still challenging.

This Sections provides an overview of the attributes tested for the purpose of identifying classification characteristics and hence, assesses the modifications compared to existing studies. A summary of the considered attributes with the expected properties is shown in the following table:

Table 5-3: Summary of the considered attributes with the expected properties.

Attribute	Expectation
Reflection attribute	Enhances individual strong reflections.
Propagation attribute	Sensitive to reflections in different depths; Still the strongest reflection has dominant imprint.
Cumulative energy	Measure of the signal strength; Deeper reflections do not get lost.
Amplitude variance	Difference in the scattering response for the two orthogonal polarizations is related to the reflector type.
Orthogonal polarization amplitude ratio	Relationship between the amplitudes for the orthogonal polarizations is different for the two reflector groups.
Autocorrelation	Reveals information about the reflector type via the periodic behavior of the apex trace.
Peak-to-peak ratio	Differences in the peak-to-peak ratio are related to the reflector type; ratio eliminates depth dependency.
Amplitude Reverberation	Time differences between the backscattered energy and the creeping wave reveal information about the diameter range.
Geometry of the hyperbola	Shape of the hyperbola gives information about the diameter range.

In the beginning reflection and propagation attributes are discussed, followed by the cumulative energy and the attributes addressing the polarization dependent amplitude variation. Next, the hyperbola geometry related attribute is presented. The end of the Section contains a short overview of logistic regression which is used to create decision lines between the two data point groups (rebars and tendon ducts).

5-4-1 Amplitude Based Attributes

Evaluating variations of amplitudes, oscillating almost symmetrically around the zero position, is the standard investigation technique for GPR surveys. Although they are strongly influenced by many factors such as material properties, the depth of a reflector and the antenna separation. Accordingly, different amplitude based attributes are evaluated with respect to the aim of this survey: Characterizing the reflectors with respect to a category of embedment.

Reflection and Propagation Attributes

The first class of attributes applied in the time domain involves full time history data over the entire survey area and is computed using *A10_refl_prop_attribute* and *A10_refl_prop_attribute_features*. The two generic terms reflection and propagation attributes can be further subdivided as summarized in the following:

- Reflection Attributes: Maximum amplitude, maximum absolute amplitude and maximum intensity.
- Propagation Attribute: Total trace area, total absolute trace area and total energy.

To the best knowledge of the author, reflection and propagation attributes where never directly applied to obtain diameter information of cylindrical objects. Generally, reflection attributes are calculated examining a single energy for each trace and thus only evaluate the particular extreme amplitude (Morris et al., 2019). Only the part of the energy propagated within the concrete should be considered and thus, the background removed data are used to eliminate the imprint of the direct wave energy. Three reflection attributes within each A-scan are commonly evaluated: Maximum amplitude, maximum absolute amplitude and maximum intensity. As expected, the first two attributes gave the same results. So, investigating both does not add information. Squaring the amplitudes for calculating the intensity enhances the contrast between the signal reflected from the target and the undesired scattering. Yet, for the considered data sets measured at the specimens A, B, C and D this did not result in more detailed information and hence, only the maximum absolute amplitude is computed and presented in Section 6-2 and Appendix B-3.

Contrary to the single point information gained with reflection attributes, propagation properties include amplitudes over the entire time history and therefore the dewowed data without a background removal can be considered. In Morris et al. (2019) the total (absolute) trace area being the integral of the amplitudes along the trace and the total energy being the integral over the intensity enable the distinction between two concrete mixes. Moreover, Queiroz et al. (2012) considers propagation attributes in combination with others to solve the inverse problem of classifying different intrusions. Consequently, this attribute is expected to be more sensitive to smaller amplitude variations. Within this study, investigation of the three propagation attributes showed that evaluating only the total absolute trace area is sufficient as the other two attributes do not increase the information content. Accordingly, Section 6-2 and Appendix B-3 show the results for the total absolute trace area computed for each data set.

In addition, in order to identify features within the reflections, the peak position related to the event is extracted from the maximum absolute amplitude and from the total absolute trace area. This is performed for both polarizations and thus, the relationship between the extracted values is evaluated (Section 6-2).

Cumulative energy

Cumulative energy integrals are defined as the squared sum of the amplitude over a specific time window which is strongly related to the dominant frequency of the signal. It is commonly applied to emphasize reflectors characterized by irregular amplitudes and thus can be used to highlight discontinuities (Castro et al., 2014; Böniger and Tronicke, 2010). Generally, the window size has to be determined carefully as too short windows result in amplitude spikes and too large windows introduce artifacts and consequently decreases the resolution of the image (Forte et al., 2010). Böniger and Tronicke (2010) suggests a time window length $2N+1$ (N time sample index) corresponding to two wavelengths of the dominant frequency and thus taking equal-weighted samples around each time step (t) into account:

$$E_{T_{m,n}}(t) = \frac{1}{2N+1} \sum_{i=-N}^{N} T_{m,n}(t+i)^2 . \tag{5-1}$$

In this equation $T_{m,n}$ refers to the trace with x coordinate index n and y coordinate index m. By applying this window to each time sample within every single trace of the data set, an energy cube is created. Indeed, due to the finite window size, samples for times smaller than half the window size cannot take the full extend into account, although this is of less importance since these samples mainly correspond to the time span of the direct wave. Similarly, for large time steps the signal commonly does not contain relevant energy. Since hyperbolic reflections are characterized by an abrupt increase in the amplitude and an amplitude variation along the hyperbolic signature, the cumulative energy attribute has the potential to differentiate energy variations from different reflectors. The cumulative energy attribute is also computed within the program *A10_refl_prop_attribute*. Similar to the reflection and propagation attributes, the energy values corresponding to the hyperbolic event are extracted and analyzed with respect to the relationship between the two polarizations (*A10_refl_prop_attribute_features*).

Amplitude Variance

Visual investigation of GPR transects obtained at concrete specimens (Figure 5-3 a)) and within synthetic studies such as in Sharma and Kind (2018) reveal a gradual change of the amplitudes along the hyperbolic signature assuming to transverse the cylinder orthogonally. This is because the response from the buried cylinder is strongly related to the illumination ellipse of the antenna relative to the position of the cylinder, as described in Section 3-3. Specifically, the amplitude variance depends on the amount and intensity of the reflected signal, on the depth of the reflector and on the antenna characteristics. Following Chang et al. (2009) the spread of the power reflectivity along the hyperbola (square of the reflection coefficient R from Eq. (2-13a)), reveals information about the diameter of the cylinder. As the exact material properties are unknown, they determine the relative permittivities via the ratios of amplitudes at the interfaces air to concrete and concrete to steel. Although, they do not consider the significant electrical conductivity of steel and thus the breakdown of the approximation to obtain R, they do obtain promising results within 7 %. In addition, it is most unlikely that a sharp increase in the power reflectivity can be observed due to the interference with neighboring events or scattering noise and due to the deviation of the antenna radiation pattern from that of a simple illumination ellipse. Consequently, the approach is modified such that simply the amplitude variance is investigated by analyzing the change along the hyperbola for the different elements. Bertram (2017) studies the potential of fitting a Gaussian distribution to relate the spread of the amplitudes to the rebar diameter ($d = 12$ mm and $d = 28$ mm) for the polarization showing maximum amplitudes. It was shown that the difference originated mainly from the change in traveltime as the illumination ellipse increases in radius the deeper the wave travels and thus, the response from deeper cylinders occur for a larger position range than for shallow cylinders resulting in a larger spread for deep objects. Accordingly, no correlation with respect to the cylinder diameter could be derived.

As a result, this attribute is evaluated by comparing the amplitude variance for the two antenna orientations using *A03_amplitude_variance* since the traveltimes for a particular object are equal. Therefore, the hyperbolic signature is extracted following the description in Section 5-3. To remove part of the impact of the depth dependent amplitude and to create comparable results, the two orientations are normalized with the following Eq. (5-2). In this equation A refers to the particular amplitude value and the indices *min*, *max* and *norm* describe the minimum, maximum and normalized amplitude, respectively.

$$A_{norm} = \frac{A - A_{min}}{A_{max} - A_{min}} \tag{5-2}$$

First, individual normalization (*normalize_ampl_range.py*) allows to recognize differences in the Gaussian shape for the two orientations. Individual refers to the fact that each polarization $\boldsymbol{E}_{inc}$-parallel and $\boldsymbol{E}_{inc}$-perpendicular is normalized independently of the other. Furthermore, normalization with respect to the antenna orientation where the incident electrical field is parallel to the long axis of the cylinder is computed (*normalize_ampl_range_Eparallel.py*). This means that the $\boldsymbol{E}_{inc}$-perpendicular polarization is normalized by using the maximum and minimum value of $\boldsymbol{E}_{inc}$-parallel. This method provides information about the absolute amplitude deviations and therefore can be used to analyze differences in reflection strength between the two components. The results of this attribute are shown in Section 6-2 and in Appendix B-3. Though, it requires the knowledge of the cylinder orientation which in simple cases can be determined by visually investigating the amplitudes of the hyperbola, similar to the analysis in Van Gestel and Stoffa (2001). However, for the measurements at the four concrete specimens the exact position and orientation is known.

Orthogonal Polarization Amplitude Ratios

As described in Section 2-3-3 the energy scattered from a steel bar exhibits a dependency on the antenna orientation relative to the cylinder and on the diameter of the object. This was modeled by Roberts (1994) for cylinders in the far field. Accordingly, the angle dependency influences the recorded amplitudes such that for broadside antennas a maximum is observed for the incident electrical field being parallel to the cylinder and a minimum is observed for $\boldsymbol{E}_{inc}$-perpendicular. Following Annan (2001) the re-emitted power depends on the radar cross section which in turn is dependent on the diameter. For the $\boldsymbol{E}_{inc}$-perpendicular configuration and an infinitely small diameter the tangential component of $\boldsymbol{E}_{inc}$ at the cylinder interface approaches zero and thus no energy can be re-radiated, Everett (2013). On the other hand, the reflected energy is dependent on the trajectory of the wave traveled in concrete. For larger distances the wave experiences more attenuation resulting in a reduction of energy. Hence, to create an attribute independent from the concrete cover the amplitude ratio for the two polarizations can be investigated using the script *A03b_amplitude_polarization_comparison*. Zanzi and Arosio (2013) emphasizes that the diameter can only be determined properly if the objects are within the low frequency region of the Radar Cross Section Ratio for the two configurations as in this region the ratio obeys a monotonic increase. Whereas for measurements within the resonance region (larger than $2\pi r/\lambda$ with r the cylinder radius), the ratio oscillated due to interference with the creeping wave and thus, the ratio is ambiguous. The low frequency approach for measurements with a center frequency of 2 GHz is valid only for objects with a diameter of less than 20 mm. Nevertheless, Utsi and Utsi (2004) and Leucci (2012) obtained successful results for the diameter estimate of embedded conductive cylinders with an accuracy of 20 % and 6 %, respectively. Since the exact value of the diameter is not needed in order to classify the two types of reinforcement, the approach can be used to determine a range for the two classes. Accordingly, the apex trace of the hyperbola region illustrated by the blue dashed line in Figure 5-3 d) is considered for each antenna orientation. To take the variation along the hyperbola into account, a range of ten traces around the apex is extracted and visualized in Chapter 6. Further, the amplitude corresponding to the apex position of the hyperbola is analyzed. Again, the amplitudes normalized with respect to $\boldsymbol{E}_{inc}$-parallel are used.

As part of the polarization attribute the arithmetic mean of the normalized hyperbola region (Figure 5-3 d)) is computed along the x-axis resulting in a single one-dimensional representation of the region (*A03b_mean_amplitude_polarization_comparison*). It is expected that more robust amplitude comparisons are created as the impact of outliers is reduced.

Autocorrelation

Autocorrelation measures the similarity of a time series with itself shifted by an amount τ and by this identifies regularities and periodicities within the signal (Farrar and Worden, 2013). Thus, the resultant dimensionless function can take values between one (perfect positive correlation) and minus one (perfect negative correlation) and is independent of the scale of the input series. A value of zero is returned in cases where no correlation between the data points exist. In any case, the maximum value is created for a zero lag because the versions are identical. According to Hyndman and Athanasopoulos (2018) two effects can occur: Trending or repetition. Trends in the autocorrelation describe that the peak positive value for zero lag slowly decreases for increasing lags. On the other hand, repetitive data result in an oscillating autocorrelation function. Hence, for increasing lags the values increase and decrease following a specific behavior. Obviously a combination of both phenomena can occur. Farrar and Worden (2013) state that the autocorrelation function can be used to obtain more information compared to investigating the time history. Indeed, the function itself does not provide information without the knowledge of the source wavelet. As determining the source wavelet involves complex processes, a relationship without incorporating this effect is searched. No study was available that investigated autocorrelation functions of GPR traces with respect to the determination of diameters. Therefore, to deduce a classification algorithm from the similarity the autocorrelation is computed for the apex trace of the hyperbola range, see Figure 5-3 d) the blue trace. Afterwards, a relationship between the two antenna orientations is investigated. For each individual event a straight line is fitted to the resultant point clouds and the slope of this line is related to the TWT at the apex (see Section 6-2). This is accomplished by using the python code *A07_autocorrelation* which in turn uses the function *autocorr.py*. The line fit is based on linear least squares regression using the Python package Virtanen et al. (2020).

Peak-To-Peak Response

Among other parameters, i.e., the concrete properties and concrete cover, the amplitude of the reflected signal from a buried cylinder is a function of the diameter. An increase in the size of the cylinder results in an increase in amplitude of the corresponding reflection hyperbola. Consequently, Eisenmann et al. (2013) formulate that the amplitude at the apex of the hyperbola can be used as a measure for the diameter. Indeed, the travel path differences between embedded objects has a powerful influence and hence, cannot simply be neglected. Though, Eisenmann et al. (2013) proposes to investigate the peak-to-peak amplitude response showing the potential for distinguishing various rebars independent of the travel path. A problem arising when dealing with shallow buried elements is the interaction with the direct wave. Hence, contrary to Eisenmann et al. (2013) by using *A08_peak_to_peak* the trough value for the present study is evaluated at a time instance later than the peak amplitude of the apex trace. Following this procedure the ratio between the two peak amplitudes is computed, again for both polarizations. Then, these ratios are investigated with respect to the TWT where each polarization is treated independently.

Amplitude Reverberations

In radargrams with high signal to noise ratios, typically two distinct events originating from the buried conductive cylinder can be observed. This is primarily, the backscattered reflection energy which can be seen for the shallowest reflection in Figure 5-3 a) at a time index of approximately 22. In addition, at a time index of about 50, corresponding to the time instance $(2+\pi)r/c$ seconds after the primary reflection (r: radius of cylinder, c: speed of light), a weaker hyperbolic signature can be identified. This represents the wave which is guided by the curved surface of the cylinder and thus, propagates around the cylinder at the speed of light until it finally travels back in the same direction as the backscattered energy (Franz and Klante, 1959; Scheers, 2001; Aldami and Karim, 2011). The impact of the creeping wave strongly depends on the frequency range of the antenna. It becomes important mainly in the resonant region where the wavelength of the signal is in the order of the size of the object. Accordingly, in this region constructive and destructive interference with the primary reflection occurs (Aldami and Karim, 2011; Zanzi and Arosio, 2013). For measurements with 2 GHz antennas this holds for diameters larger than 20 mm (Sharma and Kind, 2018). Following this theory, the temporal distance between the first reflection and the creeping wave reflection supposedly can be correlated to the diameter of the cylinder. The impact of the concrete cover thickness and the concrete properties is assumed to be eliminated due to the formation of the time difference. Accordingly, within *A09_reverberation* the amplitude related to the apex of the reflection and the amplitude at the time instance $(2+\pi)r/c$ seconds later are investigated.

5-4-2 Geometry of the Hyperbolic Signature

A conductive cylinder causes a hyperbolic reflection response in the GPR radargram if the antennas traverse the cylinder orthogonal, see Section 3-3. In general, the peak amplitude at the apex defines the horizontal position and in analogy the depth of the cylinder can be approximated by a time to depth conversion assuming an appropriate relative permittivity of the surrounding material. However, the aim of the present study is to determine the affiliation of a reflector to an object class which can be addressed by investigating the shape of the hyperbolic signature. A simple relationship between the antenna position x and the two way traveltime t satisfies the hyperbola equation in Eq. (5-3a) with t_0 and x_0 being the temporal and spatial coordinates of the apex (Qiao et al., 2015; Shihab and Al-Nuaimy, 2005). From this equation it follows, that many factors contribute to the formation of the hyperbolic signature: ϵ_r of the surrounding influences the propagation velocity v and the depth $t_0 v/2$ of the cylinder. Obviously, this model is only valid for point reflectors with zero radius which is a significant limitation as the considered cylinders have a finite radius. Considering a fixed target position ($x_0 = 0$, t_0) and fixed velocity, Figure 5-5 shows the result of the hyperbola for either zero ($r = 0$) or finite radius ($r \neq 0$). The variable R in Figure 5-5 is equal to the variable r which is used for the radius elsewhere. Obviously, the asymptotes have their intersection point at $t = 0$ for zero radius whereas it is shifted to $t = 2r/v$ for nonzero radius. In addition, when considering a zero radius the hyperbola becomes broader which could be attributed to an increase in the velocity if the asymptotes are considered to intersect at $t = 0$. As a result, Shihab and Al-Nuaimy (2005) suggests generalizing the standard equation to also include the radius yielding to an increase in the number of unknowns, see Eq. (5-3b). However, they formulate an approach based on the least-square method to determine the radius and velocity and obtain the diameter

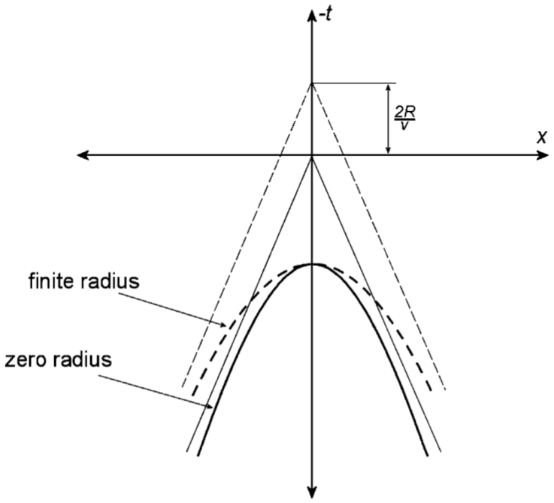

Figure 5-5: Schematic of two reflection hyperbolas with $R = 0$ (solid curve) and $R \neq 0$ (dashed curve), where x is the antenna position, t the two way traveltime, R the radius of the cylinder and v the propagation velocity. The straight lines correspond to the asymptotes.

with an accuracy of 9 %. Similar results are produced by the study in Leucci (2012) where the author applies the fitter resulting in a diameter estimate within 8 %. On the other hand, Bertram (2017) analyzed the reflection patterns for two diameters and various depths and obtained unsuccessful results independent of the depth. Moreover, the author points out that the generalized hyperbola equation in Eq. (5-3b) does not consider the antenna separation which would have a strong impact on the geometry for shallow buried cylinders.

$$\frac{t^2}{t_0^2} - \frac{4\left(x - x_0\right)^2}{v^2 t_0^2} = 1 \tag{5-3a}$$

$$\frac{\left(t + \frac{2r}{v}\right)^2}{\left(t_0 + \frac{2r}{v}\right)^2} - \frac{\left(x - x_0\right)^2}{\left(\frac{vt_0}{2} + r\right)^2} = 1 \tag{5-3b}$$

Hence, the approach for the present study is to use Eq. (5-3a) for fitting a hyperbola to the picked time and position coordinates (Section 5-3) since this keeps the computational effort small (*A05_hyperbola_geom*). As the parameters t_0 and x_0 stay constant, it is expected that the resultant velocity is a function of the diameter, among others. Following Shihab and Al-Nuaimy (2005), the estimated velocity is slightly larger compared to the actual propagation velocity of the EM wave in the surrounding. Indeed, the exact dielectric permittivity and accordingly the exact propagation velocity is unknown which limits this analysis.

5-4-3 Logistic Regression

The attribute analysis provides dichotomous data which means that every point is associated with one single class and no point should simultaneously belong to two groups. Thus, to analyze the classification of reflectors binary logistic regression is a helpful tool since it can be used to determine the probability of data points to fall into a specific category (0-false, 1-true) (Park, 2013). Contrary to linear regression where the relationship between the input and output is assumed to be linear and thus, can be used to predict a continuous value, logistic regression determines whether something is true or false (Park, 2013). To do so, multiple independent data points are investigated with respect to a category dependent variable (0 or 1). Accordingly, the parameters α and $\boldsymbol{\beta}$ should be determined obeying the function in Eq. (5-4) for every data point $\boldsymbol{x}$. In this equation p_i is the probability of the event occurring and $1 - p_i$ is the probability of the event not occurring, i.e., a data point being related to a rebar or not (Niu, 2018). α is the intercept and β the regression coefficient for the independent variable $\boldsymbol{x}$.

$$\log\left(\frac{p_i}{1 - p_i}\right) = \alpha + \beta_1 x_{i,1} + \beta_2 x_{i,2} + \cdots + \beta_n x_{i,n} \tag{5-4}$$

Performing logistic regression uses a so-called logistic function which determines the probability and therefore varies between zero and one. It fits the parameters α and β and thus, approximates a linear function mapping from the sample data to class scores (Park, 2013).

The implementation of logistic regression in Python, using the *scikit-learn* package, requires the input of the independent variable, which is described by the data points extracted from measurements with high spatial sampling rates, and the dependent binary variable, which contains the binary value corresponding to the type of reflector (zero for rebar and one for tendon duct) (Pedregosa et al., 2011). This so-called training data is used to estimate a relationship between the two variables. Accordingly, a decision line is created that divides the entire plot area into two sectors, one for each reflector type. For this study the sectors are colored red for tendon ducts and black for rebars. Then, the obtained result can be applied to the so-called test data which is for this study the data points related to the manual measurement *B-2* or to the on-site data set *E*. In particular, if the data points fall in the red shaded sector, the points are classified as tendon duct, while in the black shaded sector they are classified as rebar. Normalization in the context of logistic regression is key as it prevents numerical dominance. This means, that a scale difference in the components of the independent variable might cause the algorithm to falsely determine the direction of maximal variance (Pedregosa et al., 2011).

Chapter 6

Results

This Chapter begins with a short presentation of the results from the data preprocessing with a comparison between the dewowed and background removed data sets. Next, the different analyzed attributes are shown. They are first applied to spatially dense measurements (*A*, *B-1*, *C*, and *D*) as they provide more detailed information and the same amount of data for both antenna orientations. After a sufficient correlation of the attribute with the reflector type, the extracted feature is tested for the manual measurement (*B-2*). If attributes are applicable for the real case data set *E* the graphs also show the results for this data set. Logistic regression is applied to those attributes which indicate a distinction between the reflector groups.

6-1 Preprocessing Results

Figure 6-1 presents radargrams for the measurement at specimen *A* traversing the rebar mesh, consisting of four rebars, in the direction perpendicular to the survey line. For the PR antenna orientation which is shown in Figure 6-1a and 6-1b the dipole of the antenna is oriented parallel to the cylinders (recall Figure 5-1a) and thus for the considered rebars the PR orientation corresponds to the $\boldsymbol{E}_{inc}$-parallel polarization. Consequently, the incident electrical field for the PL antenna orientation in Figure 6-1c and 6-1d acts perpendicular to the rebars, yielding to $\boldsymbol{E}_{inc}$-perpendicular polarization data with generally lower reflection amplitudes. As the conversion from antenna orientation to polarization is dependent on the direction of the cylinder axis relative to the antenna dipole, Appendix B-2 comprises a table summarizing the relationship for the considered hyperbolic reflections.

In Figure 6-1a and 6-1c, the dewowed radargrams show the distinct direct wave for an arrival time smaller than 1 ns, followed by the hyperbolic reflections from the four rebars which is less pronounced in $\boldsymbol{E}_{inc}$-perpendicular. It can be seen, that for both orientations the direct wave influences the reflection signature, especially for the earlier regions close to the apex. Indeed, the impact is stronger for the $\boldsymbol{E}_{inc}$-perpendicular polarization in Figure 6-1c. In addition, the flanks of adjacent rebar reflections interfere constructively and destructively yielding to an increase or decrease in amplitude, respectively. From the inclined position of the hyperbolas towards the right of the radargrams it can be educed that the rebar mesh is slightly tilted within the concrete and thus, the concrete cover is not constant. Furthermore, below the reflection patterns in Figure 6-1c and 6-1c a nearly horizontal reflector originating from a rebar parallel to the survey line appears. Due to the polarization of the incident electrical field this reflector is strong in the PL orientation but not visible in the PR orientation. Towards both sides of the radargram an increase in amplitude due to the reflection from the edges of the specimen arises.

The background removal in Figure 6-1b and 6-1d clearly shows that the strong direct wave is eliminated, although towards the right the horizontal reflector is still apparent. As the reflection from the parallel rebar around 2 ns in the PL orientation (Figure 6-1c and 6-1d) is not exactly horizontal, it is not removed either. Indeed, the hyperbolic signatures sharpened and thus, the apex positions stand out from the surrounding. Moreover, the flanks can be seen with little more detail but still interference is dominant. For completeness, radargrams for the remaining scanner and manual measurements are presented in Appendix B-1 where the above considerations apply similarly. Further it can be seen, that for measurements at specimens B and D interference between adjacent cylinders does not occur.

To establish a classification algorithm, certain reflectors are extracted from the radargrams following the description in Section 5-3-1. This is visualized in Appendix B-1 where blue and pink rectangles mark rebar and tendon duct reflections, respectively. Within the on-site data set E six reflectors are selected which are annotated with green rectangles due to the unknown origin.

6-2 Amplitude Based Attributes

The maximum absolute amplitude and the total absolute trace area for the measurement A can be seen in Figure 6-2a and 6-2b, respectively. Due to the larger reflection energy, merely the upper rebar mesh in the left part of each image and the tendon duct as the horizontal anomaly at around y index 180 can be identified. Although the tendon duct shows only weak amplitudes in both attributes as the impact of deeper objects diminishes. Comparing PR and PL for both attributes confirm that the reflection strength is different depending on the orientation of the cylinder. Horizontal cylinders, such as the tendon duct, result in stronger amplitudes in the PL configuration as the incident electrical field acts parallel to these objects. Accordingly, the signatures are broader than those of the vertical cylinders. Equivalent, the PR orientation in Figure 6-2a and 6-2b on the left proves that vertical cylinders are enhanced within this orientation and thus, obscure the horizontal objects. For both antenna orientations, the area of the tendon duct which is covered by the rebar mesh is masked due to stronger amplitudes. As the total absolute trace area in 6-2b also contains energy from the lower rebar mesh, the values seem dispersed and no clear separation between the two meshes can be made.

In addition, investigating the two polarizations of the maximum absolute amplitude in Figure 6-2a again shows that the individual rebars can be more clearly delineated within the PL orientation. This is probably because the horizontal rebars are placed below the vertical rebars. Thus, due to the amplitude decrease for deeper reflectors and the sensitivity within the

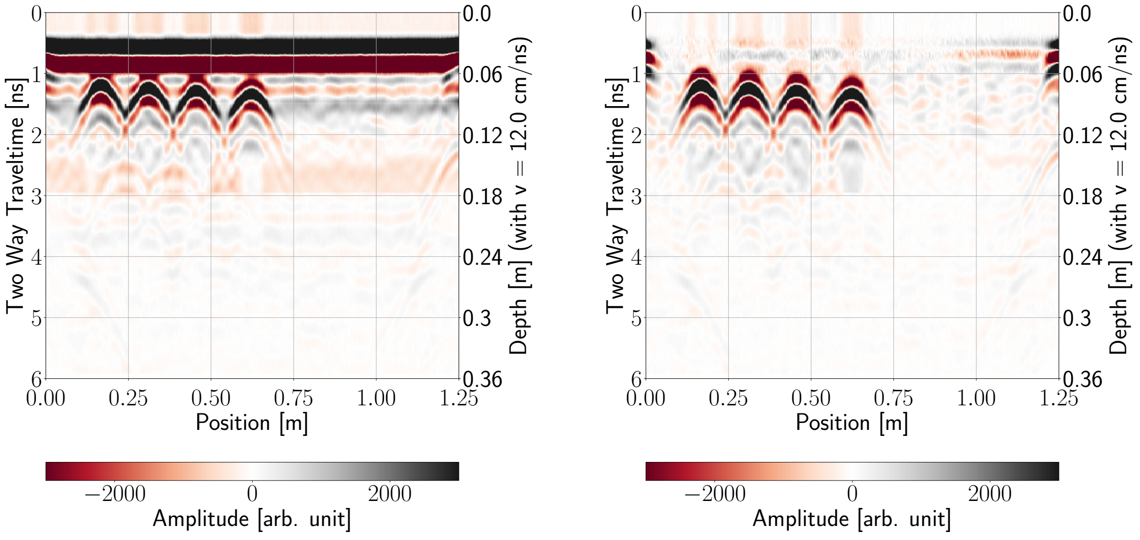

(a) Dewowed $\boldsymbol{E}_{inc}$-parallel data.

(b) Background removed $\boldsymbol{E}_{inc}$-parallel data.

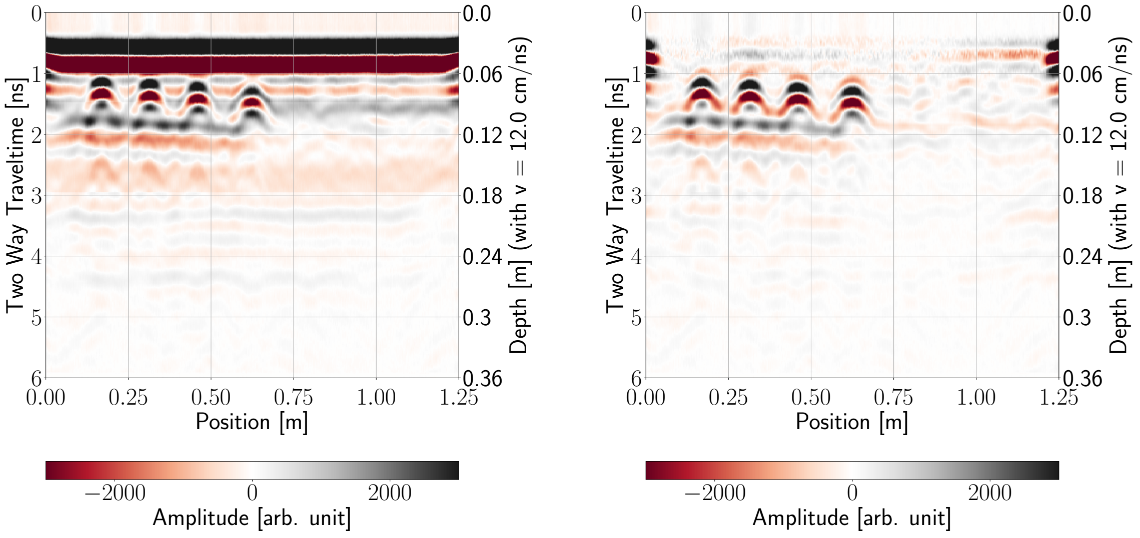

(c) Dewowed $\boldsymbol{E}_{inc}$-perpendicular data.

(d) Background removed $\boldsymbol{E}_{inc}$-perpendicular data.

Figure 6-1: Comparison of the dewowed and background removed radargrams (y-axis index 125) for the two antenna orientations PR in a) and b) and PL in c) and d). The PR and PL antenna orientations result in the $\boldsymbol{E}_{inc}$-parallel and $\boldsymbol{E}_{inc}$-perpendicular polarizations, respectively. The hyperbolic reflections correspond to the upper reinforcement mesh with a diameter of 10 mm. No time zero removal was applied.

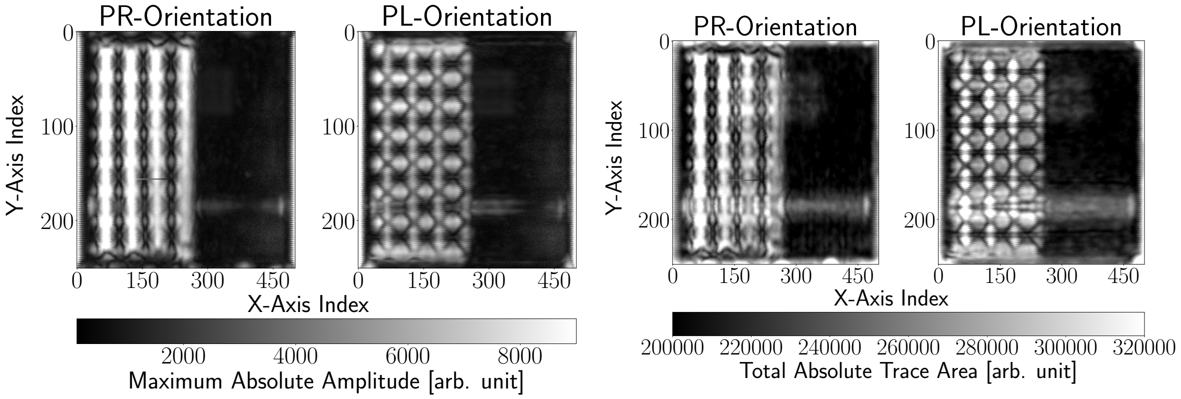

(a) Maximum absolute amplitude.

(b) Total absolute trace area.

Figure 6-2: Reflection and propagation attributes for measurement *A* in a) and b), respectively. The PR antenna orientation is shown on the left and the PL orientation on the right.

PL orientation, the distinction between the elements can more easily made. Accordingly, the areal representation of the discussed attributes can merely be used to identify the geometry.

A scatter plot with logarithmic axis is evaluated which represents the maximum absolute amplitude for positions related to the extracted reflector. This is shown in Figure 6-3a where the $\boldsymbol{E}_{inc}$-perpendicular polarization is plotted as a function of $\boldsymbol{E}_{inc}$-parallel. To increase the number of samples several data points along each reflection are considered. It reveals that generally the data lie close to or below the angle bisecting line (not indicated in Figure 6-3a). This is expected as for cylindrical objects the $\boldsymbol{E}_{inc}$-perpendicular polarization creates weaker reflections. However, due to the diameter dependency the data corresponding to tendon ducts (red) approach the bisecting line as the values for the two polarizations become comparable. In contrast, reinforcement reflections (black) cause the data to deviate towards small $\boldsymbol{E}_{inc}$-perpendicular values.

Logistic regression is applied following the description in Section 5-4-3. The resultant decision line can be seen in Figure 6-3a where the red shaded area describes the feature of tendon ducts and the black shaded area the feature of rebars with an accuracy of 93.5 % for the training data set. Applying this classification to the three upper most tendon ducts of the manual measurement *B-2* shows a good correlation (see bright red stars in Figure 6-3). For each duct five positions are evaluated yielding to clusters due to the depth dependency. Obviously, the lowest of the ducts yields to ambiguous results as only three out of the five data points are classified as tendon duct. Although this is still the majority of the tested points.

During the analysis of the data set *B-2* it was perceived that a time dependent gain applied to the data prior to attribute analysis did result in a distorted reflection attribute. This is because deeper reflections are enhanced causing stronger amplitudes in the resultant image. Hence, when computing the reflection attribute the relative difference between the extracted maximum amplitudes has changed. As a gain is applied to the data set *E* no anomaly could be observed within the maximum absolute amplitude and thus, this attribute could not be evaluated for *E*. Furthermore, a similar scattered data representation for the propagation attribute as described in Section 5-4-1 did not reveal information and therefore is not presented here.

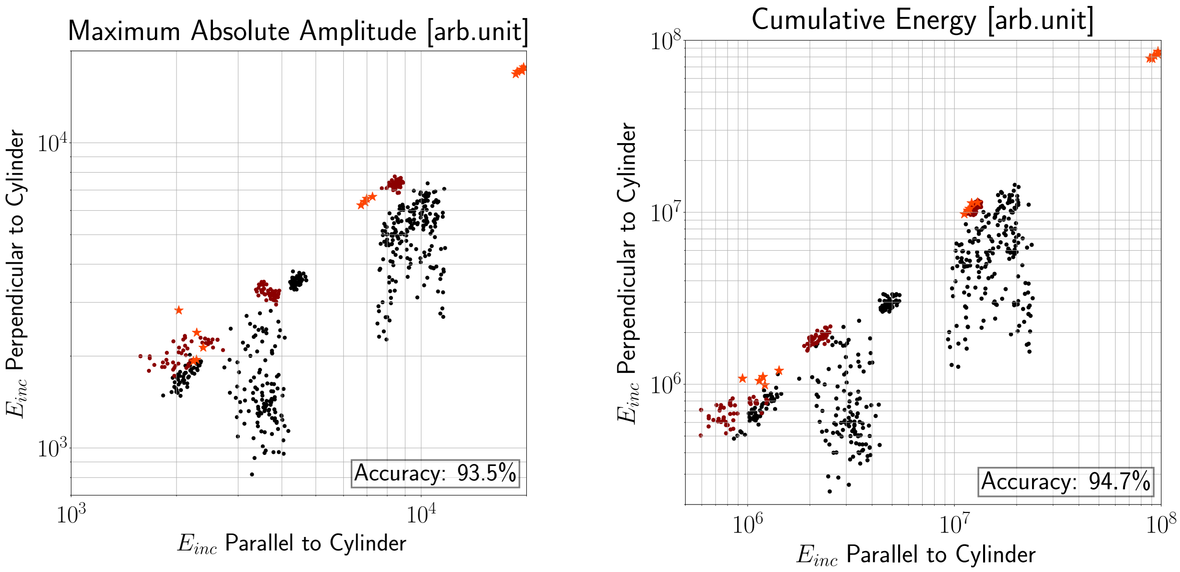

(a) Maximum absolute amplitude .

(b) Cumulative energy.

Figure 6-3: Attributes of the reflection events for the two polarizations $\boldsymbol{E}_{inc}$-parallel and $\boldsymbol{E}_{inc}$-perpendicular. Red dots correspond to tendon ducts in *A*, *B-1* and *C* whereas black dots correspond to rebars in *A*, *C* and *D*. Bright red stars correspond to the upper three tendon ducts in *B-2*. The shaded area and the accuracy represent the result of the logistic regression for the scanner measurements as training data set.

For the cumulative energy attribute B-Scans are presented in Appendix B-3. Similarly, to the reflection and propagation attribute, the $\boldsymbol{E}_{inc}$-parallel polarization creates stronger anomalies. Due to the windowed function deeper reflectors are taken more into account compared to the reflection and propagation attribute. Accordingly, the decrease in amplitude due to an increase in depth is also observed.

Again, scattered data is used to visualize the cumulative energy value related to the reflector. This is evaluated for multiple B-scans which traverse the cylinder orthogonally. Accordingly, the attribute is shown in Figure 6-3b on logarithmic axis where red dots stand for tendon ducts and black dots for rebars. A similar behavior as for the maximum absolute amplitude (Figure 6-3a) can be observed. Further, the explanation regarding the location of the rebar and tendon duct reflection points applies here as well. Again, logistic regression is performed with the scanner data points as training data set and the resultant decision line is plotted in Figure 6-3b. Comparing the two decision lines reveals a similar slope for both attributes. Nevertheless, the classification for the cumulative energy attribute results in a slightly higher accuracy 94.7 %. Computing the ratio of $\boldsymbol{E}_{inc}$-perpendicular to $\boldsymbol{E}_{inc}$-parallel and relating the two attributes indicates a linear relationship between them and thus, it seems as redundant information are added when considering both (see Appendix B-3). Indeed, Appendix B-3 provides a figure relating the ratio of the antenna orientations for both attributes which reveals that a slightly larger accuracy (97.4 %) is gained when both attributes are considered. However, some reflection points still spread into the shaded area of the other group which would result in misclassification.

The upper three tendon ducts in *B-2* show an anomaly within this attribute allowing to extract the feature within five B-scans each, indicated by bright red stars in Figure 6-3b. All data points fall in the category related to tendon ducts and thus provide more accurate results compared to the reflection attribute.

As the aforementioned considerations provide a classification only for the case of data from two antenna orientations, a correlation between the cumulative energy and the reflection attribute for each orientation is investigated in Appendix B-3. However, this approach does not show the potential to classify the reflectors as for both polarizations the data points nearly fall on one curve.

Next, examining the amplitude variation along the hyperbola for both antenna orientations require the selection of the hyperbolic signatures following Section 5-3-1. Obviously, the interference that occurs within measurements at specimens A and C increases the difficulty of this process. In addition, for manual measurements identifying the pixels corresponding to the hyperbolas is complicated due to the low spatial sampling rate of the PL antenna orientation and thus, this might introduce errors.

The amplitude variance for individually normalized hyperbola amplitudes does not provide information to establish a sufficient relation to the reflector group and is therefore only presented in the Appendix B-3. What can be seen is that the shape of the curve is similar for both orientations independent of the cylinder type. In addition, the rebars from measurement C do not resemble nice hyperbolas within the PL orientation due to the interference with each other and hence, the amplitude variation does not follow the outline of a Gaussian curve. For measurement D the lower most rebars (D-Rebar 3 and D-Rebar 2) also create chaotic amplitude variations. Consequently, for further analysis these reflectors have to be evaluated carefully.

Exemplary, Figure 6-4 presents the normalization with respect to $\boldsymbol{E}_{inc}$-parallel for measurement A. Clearly, the deviation between the curves of the two polarizations is larger for the rebar reflections in black and gray than for the tendon duct reflections in red and light red. Independent of the type of reflector it seems that it is largest for the maximum amplitude and decreases along the flanks. Also, this can be observed for the reflection events D-Rebar 5 and D-Rebar 1 (see Appendix B-3) which correspond to the shallowest rebars in specimen D. Also, for *B-1* the difference is more or less constant for all the hyperbola indices.

The investigation of the orthogonal polarization amplitude ratios is performed by relating a range of ten traces around the apex for the two polarizations. The results for the five reflectors in the data set collected at specimen A are presented in Figure 6-5. Generally, the amplitudes are distributed following a tube-like shape with a wider spread of weak amplitudes (< 0.5) for the data points related to rebars (black dots). Although, this cannot be observed for measurement D in Appendix B-3 where the data points are more or less evenly scattered around the angle bisecting line (dotted line). Accordingly, the specific scattering behavior for measurement A and C can be explained by the strong interference between adjacent rebars and by the interference with the direct wave which is not present in D. Comparing *B-1* and D indicates, that the amplitudes for tendon ducts appear centered around the angle bisecting line while the data points for rebars in measurement D seem to be slightly tilted. However, this investigation does not lead to an unambiguous distinction between the reflector types.

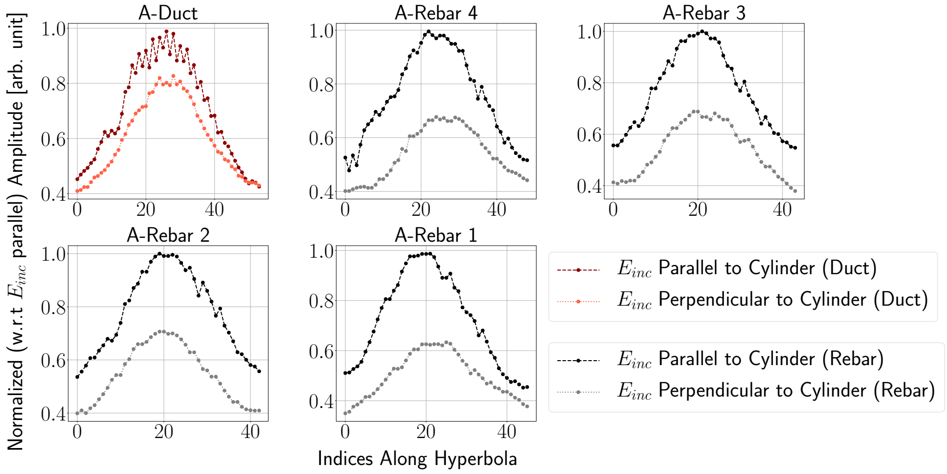

Figure 6-4: Amplitude variance for measurement *A* where both polarizations are normalized with respect to $\boldsymbol{E}_{inc}$-parallel. One tendon duct (red and orange) and four rebar reflections (black and gray) are presented.

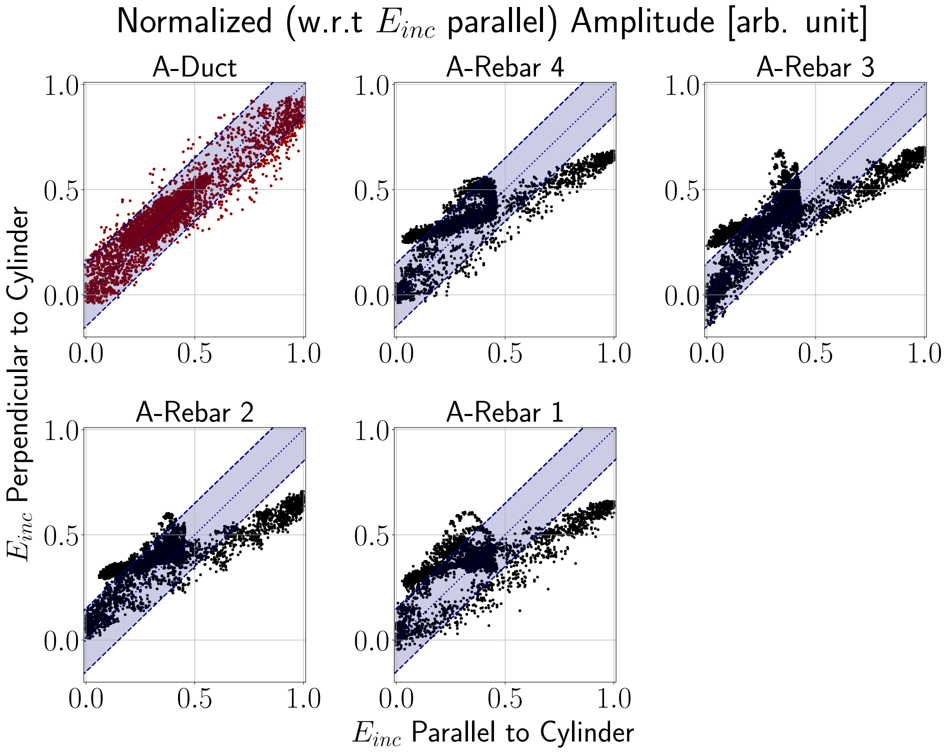

Figure 6-5: Amplitude ratios for the orthogonal antenna polarizations $\boldsymbol{E}_{inc}$-parallel and $\boldsymbol{E}_{inc}$-perpendicular for a range of ten traces around the apex trace of the hyperbola range (measurement at specimen *A*). Red corresponds to tendon ducts and black to rebars. The blue shaded area marks a $10\ \%$ range around the angle bisecting line.

As described in Section 5-4-1, the amplitudes at the apex position are commonly correlated to the diameter. Accordingly, the relationship between the apex amplitudes for the $\boldsymbol{E}_{inc}$-parallel and $\boldsymbol{E}_{inc}$-perpendicular polarization is presented in Figure 6-6. As expected, the data points which are normalized with respect to $\boldsymbol{E}_{inc}$-parallel accumulate towards a vertical axis where the $\boldsymbol{E}_{inc}$-parallel polarization takes a value of one. Due to the non-robust amplitude variance for some data points a deviation from that axis is present and therefore, the apex position does not always resemble the position of maximum amplitude. Nevertheless, data points from tendon ducts are merely in the upper half of the image where the amplitude of each orientation becomes comparable. Logistic regression is applied to the data points extracted from scanner measurements which act as training data. This reveals a nearly horizontal border between the two reflector groups, yielding to an accuracy for the scanner measurements of 92.5 % which is lower than for the reflection and cumulative energy attribute.

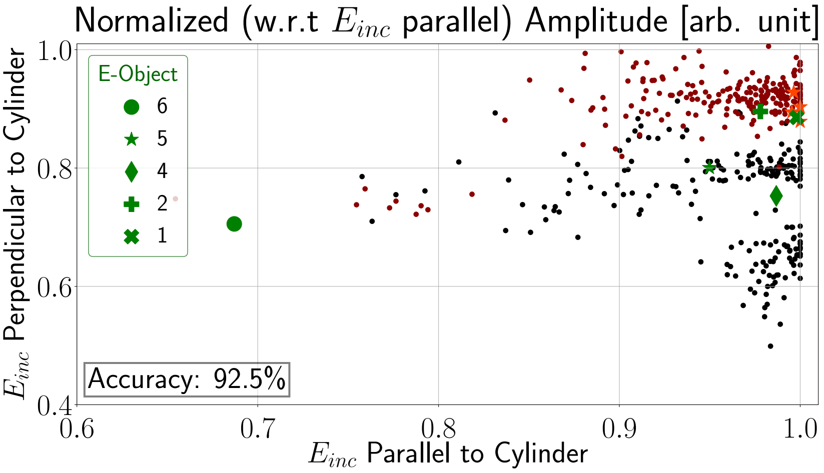

Figure 6-6: Relationship for the apex amplitudes of the objects within the $\boldsymbol{E}_{inc}$-parallel and $\boldsymbol{E}_{inc}$-perpendicular polarization. Red dots correspond to tendon ducts in *A*, *B-1* and *C* whereas black dots correspond to rebars in *A*, *C* and *D*. Bright red stars indicate the data points for measurement *B-2* and green markers are related to the different objects in *E*. The shaded area and the accuracy represent the result of the logistic regression for the scanner measurements as training data set.

Evaluating the apex position for the survey with less dense spatial sampling intervals *B-2* leads to the correct classification as tendon duct, indicated by bright red stars in Figure 6-6. In addition, this attribute was tested for the measurement E which is visualized by the green markers. Reflector E-Object 3, classified as tendon duct, is not displayed as it results in an outlier far away from the range presented here. Though, E-Object 2 and E-Object 1 result in the red shaded area corresponding to tendon ducts whereas E-Object 4, E-Object 5 and E-Object 6 are classified as rebar.

The mean along the x-axis of the normalized hyperbola range is presented in Figure 6-7 for survey A and in Appendix B-3 for the remaining surveys. Clearly, for the $\boldsymbol{E}_{inc}$-parallel polarization on the left, the maximum of the mean normalized amplitude is larger for the black curve which represent rebars. Contrary, for the $\boldsymbol{E}_{inc}$-perpendicular polarization in the middle, this is reversed as the bright red curve for the tendon duct shows larger maximum amplitudes than the rebars (gray curve). In addition, the shape of the mean for $\boldsymbol{E}_{inc}$-parallel and $\boldsymbol{E}_{inc}$-perpendicular behaves similar for the tendon ducts but deviates strongly for the rebars. As a result, the scatter plot on the right shows that the tendon ducts (red points)

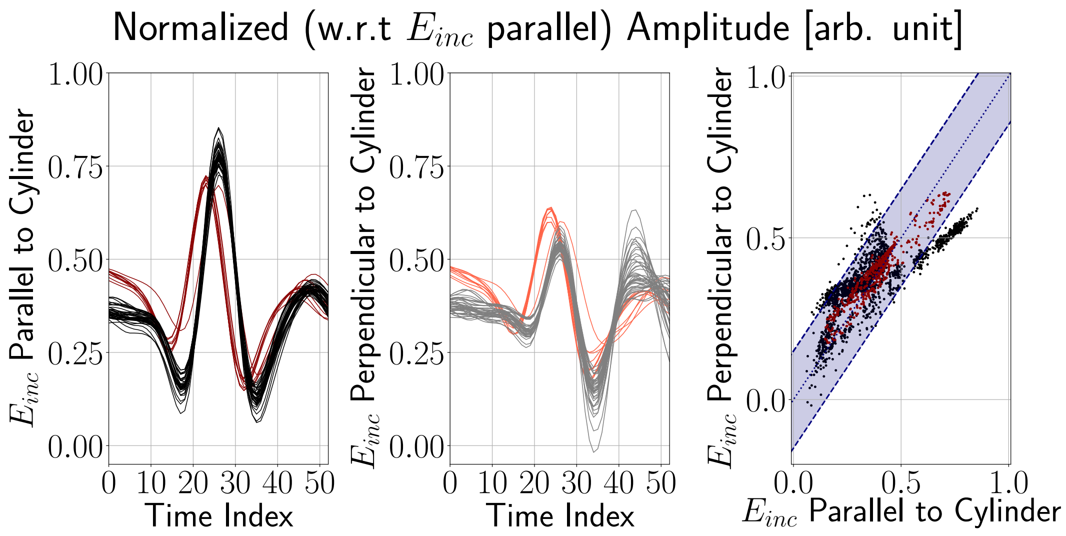

Figure 6-7: Mean of the normalized hyperbola range for the $\boldsymbol{E}_{inc}$-parallel polarization (left) and $\boldsymbol{E}_{inc}$-perpendicular (middle). Normalization was performed with respect to (w.r.t.) $\boldsymbol{E}_{inc}$-parallel. On the right, the relationship between the two is presented. Red and orange dots correspond to tendon ducts and black and gray dots to rebars.

accumulate around the angle bisecting line (dotted line) and do not exceed the blue shaded range corresponding to 10 % above and below that line. On the other hand, the rebar data points (black) are spread within that range and even achieve values outside. The point cloud around 0.75 for $\boldsymbol{E}_{inc}$-parallel leaving the blue range corresponds to the maxima of the curves in the middle and on the left. Comparing the results for measurement *B-1* and *D* in Appendix B-3 which describe data where nearly no interference between adjacent cylinders takes place shows that the maximum for the mean is comparable for tendon ducts but deviates for rebars. A scatter plot representing the maximum amplitudes of the mean curves for both polarizations is only presented in Appendix B-3. In the first instance, it shows the potential for differentiating the two reflector types. Although, incorporating the manual measurement *B-2* (bright red stars) does not show a clear separation anymore. Furthermore, for the real case measurement *E* the green markers do exceed the range of the discussed data points strongly and thus, the classification using the mean trace is not reliable.

The autocorrelation to enhance information contained in the GPR data can be found in Appendix B-3 where the individual autocorrelation functions for the considered polarizations and the relationship between them is presented. All curves, independent of the type of reflector, exhibit a trending and repetitive behavior. Thus, the shape of the functions does not seem to support the classification of hyperbolas. Contrary, the relationship between the polarizations exhibits a linear trend for all the data points. Comparison between the different scanner measurements shows that autocorrelations related to tendon duct reflections are distributed mainly around the angle bisecting line while for rebars the line around which they are centered appears to be slightly tilted. Accordingly, the slope of the line fit is related to the TWT, see Figure 6-8. Certainly, this graph does not show a cluster of the data points for a cylinder type. Indeed, for large TWTs the two groups fall in the same range of slopes while for small TWTs (< 2 ns) a separation is recognizable. Although, these black data points belong to the rebars of measurement A and C which are strongly subjected to interference of adjacent rebars as well as to interference with the direct wave. This observation indicates that the autocorrelation in this form cannot be considered to derive features of the two reflector groups.

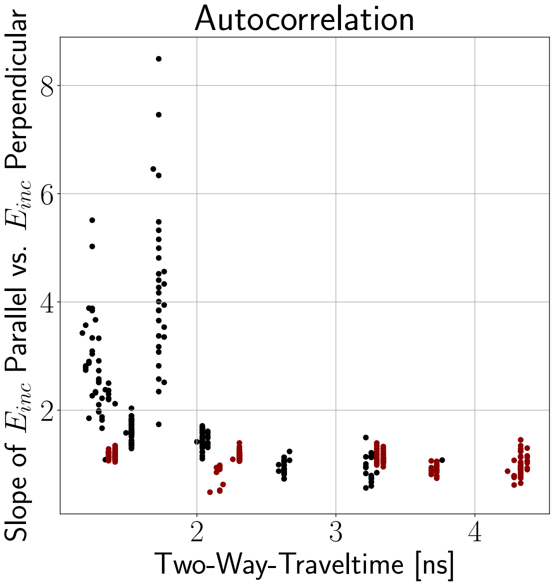

Figure 6-8: The slope of the line fit for the autocorrelation of $\boldsymbol{E}_{inc}$-parallel as a function of $\boldsymbol{E}_{inc}$-perpendicular with respect to the TWT is presented. Red dots correspond to tendon ducts in *A*, *B-1* and *C* whereas black dots correspond to rebars in *A*, *C* and *D*. The dashed blue line describes the border between the range where the trough amplitude is larger compared to the peak amplitude (< 1) and vice versa for > 1.

Next, the peak-to-peak amplitude ratio is analyzed following the description in Section 5-4-1. Figure 6-9 illustrates the ratio relative to the TWT, showing a nearly distinct separation for the $\boldsymbol{E}_{inc}$-perpendicular polarization of the scanner measurements in the middle: Tendon duct data points (orange) appear merely in the range where the peak-to-peak ratio takes values larger than one (blue dotted line) whereas rebar data points (gray) fall below one. As some rebar points fall in the range above one it is advisable to consider multiple data points for each reflection event in order to increase the probability of finding the right class of reflector. Manual measurements cannot be sufficiently classified as the yellow stars in Figure 6-9 on the right show values smaller than one and thus, without knowing the origin these would be misclassified as rebar.

Furthermore, Figure 6-9 on the left presents the peak-to-peak ratio for $\boldsymbol{E}_{inc}$-parallel indicating that this polarization does not yield to a reliable differentiation due to the spread of data points. In the traveltime range between 0.5 ns to 3.5 ns it seems as if the rebar reflections tend to result in lower peak-to-peak ratios compared to the tendon ducts. Although, the points are quite spread and no clear separation can be defined. In addition the rebar point cloud for TWTs smaller than 0.5 ns results in a higher ratio than for the tendon duct in a similar TWT region. However, this could be due to the interference with the direct wave. For the sake of completeness, bright red stars mark the four tendon ducts from measurement *B-2* and emphasize that a classification using the peak-to-peak ratio with respect to the TWT is ambiguous.

As the relationship between the two measurement polarizations have shown to provide meaningful results, Appendix B-3 illustrates the peak-to-peak ratio for $\boldsymbol{E}_{inc}$-perpendicular as a function of $\boldsymbol{E}_{inc}$-parallel. Again, logistic regression is applied with the data points from the scanner measurement as training data set yielding to the classification indicated by the shaded areas. As expected from the discussed peak-to-peak ratios, the obtained decision line assigns the four tendon ducts of *B-2* to the black shaded area and thus falsely to the class of rebars. In addition, green markers describing the measurement *E*, yield to a different classification than the aforementioned attributes: *E*-Object 1 appears due to a tendon duct whereas the others are related to rebars. Thus, the ratios provide promising results for the scanner measurement but seem to generate falsely classifications for manual measurements.

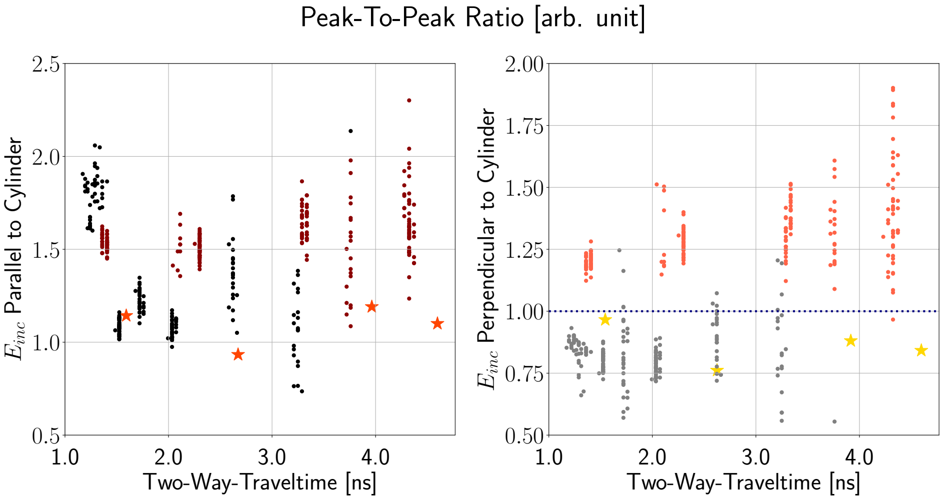

Figure 6-9: Peak-to-peak amplitude ratio for each polarization as a function of TWT. On the left $\boldsymbol{E}_{inc}$-parallel is presented and on the right $\boldsymbol{E}_{inc}$-perpendicular. Red and orange dots correspond to tendon ducts and black and gray dots to rebars.

Amplitude reverberations due to the creeping wave are expected to only occur for cylinders with a diameter larger than 20 mm (see Section 5-4-1). Indeed, these reverberations are only present in the data if the signal-to-noise ratio is high and if no strong events appear within the time range for the creeping wave. Consequently, this is seldom the case for on-site measurements. As can be seen in the radargrams in Appendix B-3 the creeping wave can be identified for measurement *B-1* and *D* which is in accordance with the expectation as the two data sets contain reflections from cylinders with a diameter of 28 mm and 80 mm, respectively. Although, investigating the amplitude difference for the peak amplitude and the amplitude which is considered to be related to the creeping wave did not yield to any classification potential as the investigated diameters do not provide a sufficient number of samples. In addition, this attribute is only applicable to data with superior quality and consequently, not useful for commercial application.

6-3 Geometry of the Hyperbolic Signature

Again, the hyperbola selection is difficult for data with low spatial sampling rates and with low signal-to-noise ratios. Using a non-linear least squares python function, the hyperbola equation for zero radius (Eq. (5-3a) in Section 5-4-2) is modeled and fit to the hyperbola selection. The results for the four scanner measurements, with the apex centered around the zero position, are shown in Appendix B-4. In the first instance, it seems that cylinders with larger diameter result in a wider hyperbola as rebar reflections generally show narrow curves. However, when investigating the graph for measurement *B-1* and *D* the increase in concrete cover yields to the widening of the hyperbola. Although, comparing the shallowest cylinders (solid line), the two curves differ even if the concrete cover is identical. Indeed, for *B-1*-Duct 3 and *D*-Rebar 4, which show a similar cover thickness, the hyperbola is wider for the rebar reflection. Hence, investigating simply the shape of the hyperbola is difficult as the data is not dichotomous and thus cannot be assigned to only one class.

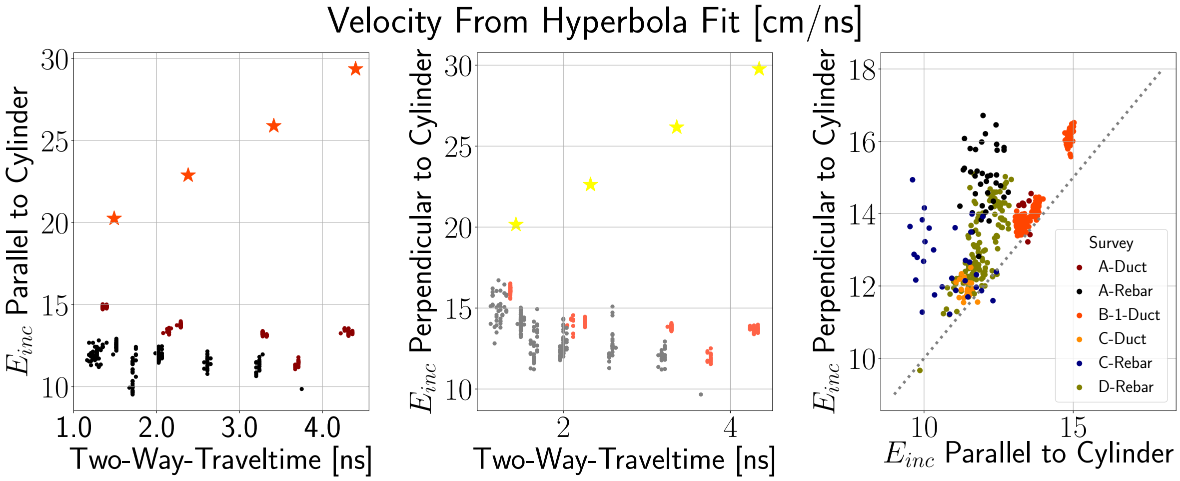

Figure 6-10: Velocity of the hyperbola obtained by fitting the hyperbola equation with zero radius. On the left and in the middle $\boldsymbol{E}_{inc}$-parallel and $\boldsymbol{E}_{inc}$-perpendicular are presented as a function of TWT. Red dots correspond to tendon ducts and black dots to rebars. The right side contains the relationship between the velocities of both polarizations, color coded with respect to the measurement.

Based on the explanation in Section 5-4-2 the velocity from the hyperbola fit is investigated. Therefore, Figure 6-10 shows on the left the result for the $\boldsymbol{E}_{inc}$-parallel polarization and in the middle the result for $\boldsymbol{E}_{inc}$-perpendicular both as a function of the TWT. Again, the scanner measurements in multiple B-scans can be identified by red and black dots for tendon ducts and rebars, respectively. It can be seen, that the separation between the two classes is distinct for $\boldsymbol{E}_{inc}$-parallel where only the red point cloud around 3.75 ns appears to interrupt the pattern. Neglecting these data points, the tendon ducts show larger velocities than the rebar reflections. For both classes the velocity decreases as the TWT increases. Also, this can be observed for the second polarization in the middle of Figure 6-10. Although, the data points cannot be separated as clearly as in $\boldsymbol{E}_{inc}$-parallel. Nevertheless, the trend towards low velocities for the point cloud at 3.75 ns shows the same decrease in velocity. As indicated in the scatter plot on the right, this group of velocities belongs to the tendon duct in C (orange dots). An explanation for this systematic behavior could be the large concrete cover and comparatively large diameter. However, the scatter plot reveals relatively low velocities for the rebars in C (blue points) as well. Therefore, it is more probable that the hyperbola fitting velocity values stand out due to a lower radar wave velocity.

Within the scatter plot of the two polarizations (Figure 6-10 right) it can be observed that the fitting velocity is larger for the $\boldsymbol{E}_{inc}$-perpendicular polarization than for $\boldsymbol{E}_{inc}$-parallel. Consistently, neglecting the velocity for C-Duct the scanner data points show a nearly vertical border between the two classes around the x-axes value of 13 ns.

This attribute is applied to the measurement *B-2* showing extremely large velocities which are out of the range (bright red and yellow stars in Figure 6-10). Indeed, as measurement *B-1* and *B-2* were conducted at the same concrete specimen it would be expected that they result in the same hyperbola velocities which is not the case. This might be attributed to an error in the hyperbola fitting procedure. Although, the fit compares well with the selected pixels.

Chapter 7

Discussion

Multiple attribute based approaches to determine the diameter of a cylindrical object within concrete exist (Bertram, 2017; Chang et al., 2009; He et al., 2009; Leucci, 2012; Shihab and Al-Nuaimy, 2005; Utsi and Utsi, 2004). Indeed, none of the studies assess the classification of hyperbolic reflections by deriving features that unambiguously determine the reflector origin. Therefore, this thesis presents different approaches for attribute based analysis in order to derive a classification scheme for reinforcement bars and tendon ducts. A summary with respect of the potential for feature extraction is shown in Appendix B-3. Although image-based approaches are less computationally intensive they do not always reveal the origin of the reflector. Accordingly, attributes are evaluated for four different data sets with high spatial sampling rates and for two less dense manual measurements. In addition, the attempt is to keep the computational effort as small as possible.

To increase the number of data points the selected hyperbolic events were transferred to neighboring profiles via amplitude information. For concrete specimens with rebar meshes this was challenging as reflections from orthogonal cylinders interfere with the target event and thus erroneous hyperbolas were returned. They had to be discarded by visual inspection. Thus, this process has to be improved to reduce the effort for the operator.

First of all, the areal representation of the reflection and propagation attributes in Figure 6-2 asses mainly the internal structure of the concrete block but do not provide information about the type of intrusion without further processing. It was found that evaluating the maximum absolute amplitude (reflection attribute) for the specific reflection events in both polarizations, depicts a characteristic behavior that enables the identification of two distinct classes (Figure 6-3a). The reason for this is that tendon ducts have a large radar cross section area compared to rebars and thus generate stronger reflections in the $\boldsymbol{E}_{inc}$-perpendicular polarization.

Obviously, the reflection attribute classification can only be applied when the tested event exhibits the maximum amplitude for the entire trace. Consequently, this involves limitations for the considered data sets: First, no gain should be applied prior to extracting the reflection events because this manipulates the relative amplitude. Specifically, for the propagation attribute the gain applied prior to storing the data distorts the resulting image as the attribute takes the entire time history into account. Second, no strong reflector should exist above the actual target because otherwise the maximum absolute amplitude is not sensitive to the target. However, this is challenging as it constitutes a very simple data set for which commonly no classification algorithm must be applied.

This attribute results in a classification not only for the four scanner measurements but also for the survey *B-2*. Accordingly, in the first instance there seems to be no need for an improvement of the spatial sampling interval for real case applications. Opposed to this, the data set acquired at a bridge in Northwestern Germany cannot be evaluated because no clear anomaly could be assigned to any of the six reflectors. As the radargrams in Appendix B-1 show, the data contain reflections from many buried objects which lie in different depth. Due to low amplitude ranges between adjacent reflection hyperbolas in the upper part of the PR orientation (below 2.5 ns) the maximum absolute amplitude for these ranges extracts the high amplitude of the later occurring reflection ($\approx$ 3 ns). As a result, no distinct anomaly can be discerned. Especially for the PL orientations with an extremely large spatial distance between the traces (100 mm), relating the amplitude to a certain reflection event becomes difficult.

A similar discussion applies to the cumulative energy attribute: The B-scans from the energy cubes of the data sets in Appendix B-3 reveal distinct anomalies also for deeper objects as the sliding time window includes energy from the entire record. This leads to individual anomalies for the measurement E in $\boldsymbol{E}_{inc}$-parallel while for $\boldsymbol{E}_{inc}$-perpendicular the blurred hyperbolas in the radargram transfer into distorted energy values. Due to the summation and the squaring in the cumulative energy equation (Eq. (5-1)) the resultant range of values is larger compared to the maximum absolute amplitude. In addition, the cumulative energy provides a slightly larger accuracy of 94.7 % compared to 93.5 % of the reflection attribute.

Taking a closer look at the individual point clouds in the Figure 6-3a and 6-3b shows that for low amplitudes (cluster 1) the black rebar related data points are positioned further away from the decision line for the cumulative energy compared to the maximum absolute amplitude. Although, this goes along with a shift of the red tendon duct related data points further into the black shaded area. Accordingly, both point clouds are shifted and thus a less accurate result is given for the cumulative energy attribute. On the other hand, the bright red stars which are the reflection points for the second deepest tendon duct in concrete specimen B are more precisely classified in the cumulative energy attribute than in the reflection attribute. However, as they resemble the data points from the scanner measurement *B-1* they should coincide with these data points which is not given for any of the two attributes.

All three point clouds in cluster 2 are well distinguished (Figure 7-1a and 7-1b). However, some data points are still misclassified since they extend into the shaded area of the other reflector group. This effect is stronger for the maximum absolute amplitude attribute. Thus, the cumulative energy provides higher accurate results in the intermediate range.

Considering the high amplitude range in cluster 3 (Figure 6-3a and 6-3b), indicates a sufficient classification for both attributes. Yet, the separation of the two point clouds corresponding to tendon ducts and rebars is more pronounced within the maximum absolute amplitude (Figure 7-1a). Again, the data points of measurement *B-2* are not conform with the scanner measurement *B-1*.

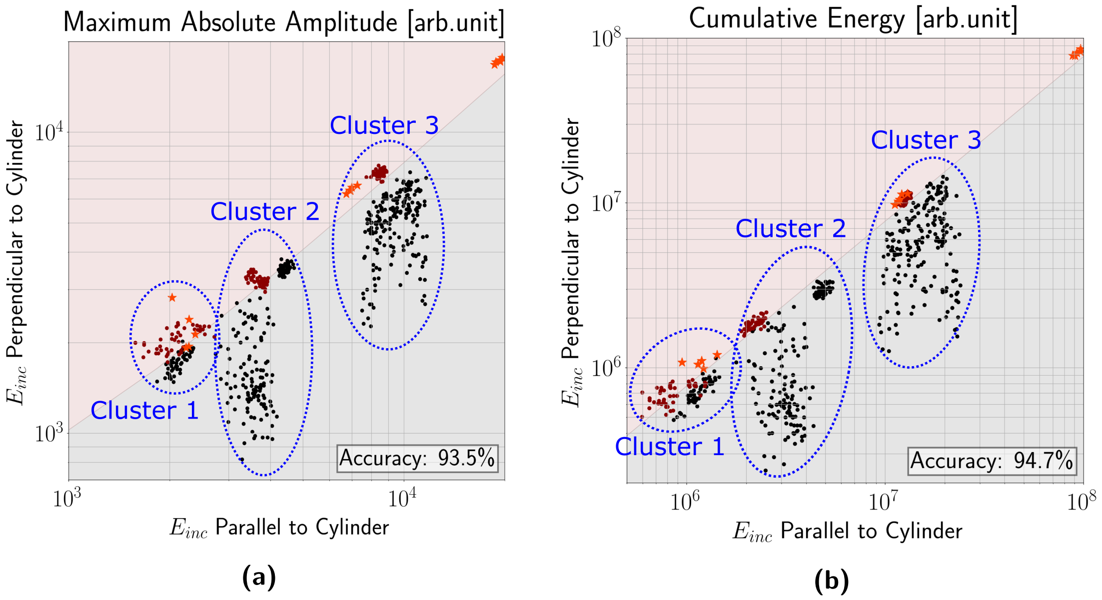

Figure 7-1: Attributes of the reflection events for the two polarizations $\boldsymbol{E}_{inc}$-parallel and $\boldsymbol{E}_{inc}$-perpendicular. Red dots correspond to tendon ducts in *A*, *B-2* and *C* whereas black dots to rebars in *A*, *C* and *D*. Bright red stars correspond to the upper three tendon ducts in *B-2*. The shaded area represents the result of the logistic regression. The blue dotted lines mark the three clusters.

Concluding, three clusters which are related to the change in TWTs can be identified with different benefits of application. Unfortunately, the clusters cannot be assigned to a distinct range of traveltimes. Furthermore, in order to evaluate the potential of the maximum absolute amplitude and the cumulative energy attribute Appendix B-5 contains the analysis for random data points which do not correspond to any reflection event (purple stars). These points obey a chaotic behavior which is confirming the potential for the combination of the maximum absolute amplitude and cumulative energy attributes to delineate features of the two reflector groups. Two approaches can be made to overcome the limitations: It is advisable to not only apply the attribute to one reflection point but investigate many points corresponding to the maximum position along a line transecting the cylinder perpendicular. By doing so, the probability of accurate assessment increases. Second, as visualized in Appendix B-3 relating the maximum absolute amplitude and the cumulative energy leads to a more precise classification (97.4 %).

The results for the amplitude variance prove that investigating the entire hyperbola is challenging, especially for the cases where interference between adjacent cylinders is present (measurement C). No clear Gaussian shape can be identified for these hyperbola amplitudes. Further, comparing the shape for the two polarizations normalized with respect to $\boldsymbol{E}_{inc}$-parallel for measurements A, *B-1* and D show ambiguous results as no distinct behavior for the two reflector groups is obtained. Again, the reason for this is the difference in RCS. As proven in Zanzi and Arosio (2013) the relationship between the amplitudes for $\boldsymbol{E}_{inc}$-parallel and $\boldsymbol{E}_{inc}$-perpendicular can only be successfully determined for the low-frequency region. Accordingly, for a 2 GHz survey the considered diameters must be smaller than 20 mm (Sharma and Kind, 2018). Otherwise, for frequency ranges resulting in $2\pi R/\lambda > 1$ the ratio between the two polarizations oscillates and hence, the relative difference between the curves is unstable. In case of the tendon duct in C with ∅ 86 mm, the center frequency of the measurement has to be $<$ 400 GHz in order to work in the low-frequency region. Nevertheless, it is observed that the amplitude difference between the two polarization occurs over the entire range of the hyperbola. This is because the hyperbolas are created as the antennas are moved perpendicular to the cylinder and thus the amplitudes along the flanks are also influenced by the smaller RCS. Concluding, the amplitude variance cannot be considered to classify reflectors over a broad range of diameters if the resolution should be appropriate.

Due to the dependence of the scattering response on the RCS, the scatter plot of the ten traces around the apex do not provide promising results, see Appendix B-3. The distinct difference in the inclination of the point clouds for the rebars in measurement A and C is ambiguous as for the individual rebars in measurement D this cannot be observed. A reason for this is probably the interference with the direct wave arrival in data set A and C. Nevertheless, for rebars it can be observed that large values in $\boldsymbol{E}_{inc}$-parallel ($>$ 0.75) yield to relatively low values in $\boldsymbol{E}_{inc}$-perpendicular. Thus, simply extracting the apex amplitude decreases the computational effort by simultaneously increasing the benefit.

Apex amplitudes for the two orthogonal polarizations in Figure 7-2 show that a nearly horizontal decision line is created from the logistic regression. Approximately three clusters can be recognized: The red tendon duct reflections for high values of $\boldsymbol{E}_{inc}$-parallel are consistently showing comparable amplitudes for $\boldsymbol{E}_{inc}$-perpendicular. A second cluster appears which corresponds to the rebars in D where no interference with the direct wave is prominent and the diameter of the rebar is larger than for the other reflections. The third cluster includes the range for small $\boldsymbol{E}_{inc}$-perpendicular amplitudes ($<$ 0.7) and is related to rebars in A and C. Accordingly, the separation between cluster 2 (∅ 28 mm) and cluster 3 (∅ 10 mm and ∅ 12 mm) potentially occurs due to the difference in diameter. However, further investigation of data from concrete specimens with a structure similar to D but with different diameters has to be performed since the presented result do not entirely address the impact of the direct wave and the interference between reflections. Nevertheless, this attribute proves the potential for differentiating between data points related to tendon ducts and rebars under controlled environments. In addition, the existence of cluster 2 and 3 reveals that information about the rebar diameter can be extracted in order to indicate whether a rebar with rather small or larger diameter is present.

Following the derived features, E-Object 1 and E-Object 2 would be classified as tendon ducts although construction plans reveal that the position of the reflection hyperbola coincides with reinforcement bars. Furthermore, E-Object 4 and E-Object 5 are classified as rebar. Indeed, these reflections potentially originate from hollow bodies and thus obey different scattering behavior than steel intrusions. The misclassification for the lower reflections is expected because the amplitudes around the apex are weakened due to preceding reflections. Another explanation is that the even larger spatial sampling intervals for the PL orientation (100 mm) compared to *B-2* (50 mm) result in nearly horizontal reflectors where no hyperbolic signal can be identified anymore (Appendix B-1). Consequently, in order to obtain reliable information, the spatial sampling rate determined by the Nyquist criterion should not be violated too strongly. For the sake of completeness, Appendix B-5 shows the apex attribute analysis in comparison with random extracted amplitudes. These random data points follow the angle bisecting line towards low amplitude values with only small deviations. This encourages the above consideration as the rebar reflections clearly deviate from this angle bisection line

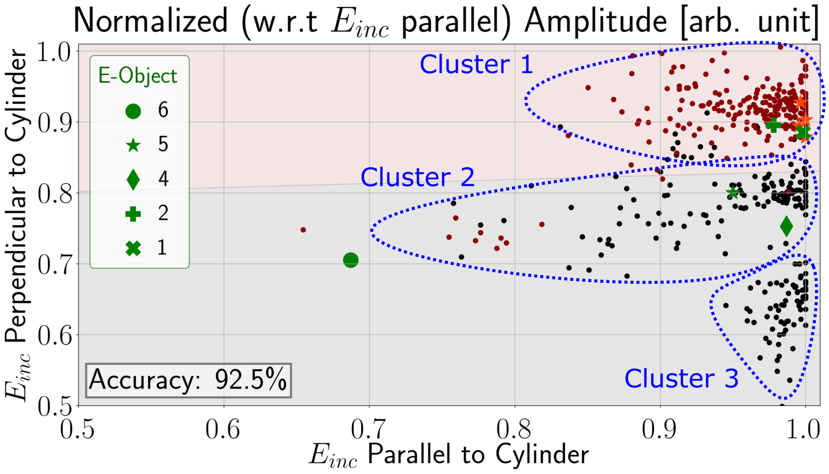

Figure 7-2: Relationship for the apex amplitudes of the objects within the $\boldsymbol{E}_{inc}$-parallel and $\boldsymbol{E}_{inc}$-perpendicular polarization. Red dots correspond to the reflection hyperbolas of tendon ducts and black dots to rebars, both for scanner measurements (*A*, *B-1*, *C* and *D*). Bright red stars indicate the data points for measurement *B-2* and green markers are related to the different objects in *E*. The three clusters of data points are marked by the blue dashed oval.

towards lower values.

Since the amplitude variance reveals strong deviations from the Gaussian shape for some events, computing the mean trace from the cutout hyperbola region constructs more stable amplitudes (Figure 6-7). An explanation for the larger difference between the shape of the mean in $\boldsymbol{E}_{inc}$-parallel and $\boldsymbol{E}_{inc}$-perpendicular for the rebars is the process of hyperbola creation. As stated for the amplitude variance, the diameter related smaller amplitudes occur over the entire range of the hyperbola. Thus, when adding up these values for the arithmetic mean the effect becomes amplified. Unfortunately, the maximum value of the mean (Appendix B-3) does not give sufficient results for the tendon ducts of *B-2* and for the objects in *E* which might be attributed to the large spatial sampling intervals. Accordingly, the feasibility is limited to high spatial sampling rates.

Autocorrelation functions for the apex trace of the cutout also do not result in a feature sufficiently describing the reflectors. This is visualized in Figure 6-8 which shows the slope of a line fit to the autocorrelation of the four scanner measurements. The occurring deviation coincides for the entire TWT range except for times < 2 ns which is probably due to the direct wave interference.

The peak-to-peak amplitude ratio gives moderate classification results as a clear distinction can only be identified within $\boldsymbol{E}_{inc}$-perpendicular (Figure 6-9 on the left). In accordance with Eisenmann et al. (2017) the peak-to-peak ratio shows overlapping regions for $\boldsymbol{E}_{inc}$-parallel because the waveform shape does not change significantly when alternating the diameter. Whereas for $\boldsymbol{E}_{inc}$-perpendicular the waveform is sensitive to the diameter change. In this case, for rebars the trough amplitude is typically larger than the peak amplitude (< 1). Contrary, for tendon ducts this is reversed as the ratio depicts values larger than one. Constrained by low spatial sampling rates, peak-to-peak ratios for measurement *B-2* result in low ratios for both polarizations. Following this observation, simply measurements with the $\boldsymbol{E}_{inc}$-perpendicular polarization with relatively high spatial sampling rates need to be conducted in order to test the classification for a data set. On the one hand the acquisition time is reduced by only requiring one polarization but simultaneously the spatial sampling limitation results in an increase of time again. In addition, in order to determine the $\boldsymbol{E}_{inc}$-perpendicular polarization for unknown targets the orientation of the cylinder relative to the antenna must be known. Accordingly, pre-studies have to be performed to identify the orientation of the target cylinder which in turn increases the survey time. Further, commonly conductive cylinders in at least two directions are built in, yielding to the exigency of $\boldsymbol{E}_{inc}$-perpendicular data for each direction. Thus, to obtain sufficient results from the peak-to-peak attribute the acquisition time is increased due to high spatial sampling rates in both antenna orientations.

Identifying the amplitude reverberation due to the creeping wave is challenging and only possible under ideal circumstances: High signal to noise ratios and no strong events occurring in its time range. As the creeping wave is strongly damped, the amplitude of the recorded wave is much smaller than the backscattering response (Franz and Klante, 1959). Thus, if a lot of undesired scattering energy is returned the creeping wave is masked. Furthermore, this attribute is limited by the frequency and diameter relation described in Section 5-4-1.

The hyperbola geometry related attribute which analyzes the hyperbola fitting velocity needs further investigation by considering concrete specimens with diverse structure. So far, the presented results in Figure 6-10 only reveal a potential distinction within $\boldsymbol{E}_{inc}$-parallel whereas for $\boldsymbol{E}_{inc}$-perpendicular the two reflector groups show coinciding velocities. This might be caused by the difficulty of selecting hyperbolas within the $\boldsymbol{E}_{inc}$-perpendicular polarization. In particular, for measurements A and C the hyperbolas are not pronounced due to the direct wave interaction and the smaller backscattering characteristic. On the other hand, selecting the proper pixels within B-scans of measurement D was relatively simple but still a distinction based on the velocity as a function of TWT cannot be made. The reason for this could be a strong impact of the actual EM velocity on the resultant hyperbola fitting velocity. However, relating the two observations depicts more promising results.

Another reason for the overlapping point clouds for the TWT related attribute analysis is the missing time zero removal. Even though the controlled environments provide smooth surfaces and the need for setting the traces to the correct zero TWT was neglected, for a comparison with other data this is an essential step. Consequently, for further analysis the time zero should be determined.

In addition, Zanzi and Arosio (2013) state that due to the interaction of the energy, scattered from the cylinders, with the background signal an inappropriate background removal can cause the RCS ratio to deviate from the theoretical prediction. As a consequence, wrong amplitudes are extracted yielding to wrong classifications. Therefore, the background removed data should solely be considered when no hyperbola can be extracted elsewhere. In this case the resultant data points must be considered carefully and should be compared to the dewowed data.

As the scattering response described by the RCS impacts all amplitude related attributes this yields to a frequency dependency of the tested attributes. However, for this thesis only one center frequency ($f_c = 2$ GHz) was considered and therefore the diameters which are in the low frequency range are limited to < 20 mm.

Chapter 8

Conclusion and Outlook

Attributes exist in great quantity and within recent years many surveys were conducted that attempt to determine the diameter of conductive cylinders. Indeed, none addressed the classification with respect to the structural design. Within this thesis attribute based analysis of reflectors within reinforced and prestressed concrete was performed to delineate features which clearly assign the reflection to either reinforcement bars or tendon ducts. Accordingly, some existing methodologies were adapted for the purpose of this survey and some attributes where established due to visual inspection of the data.

The analysis was applied to data sets ($f_c = 2$ GHz) from four concrete specimens available at BAM. Besides scanner measurements with high spatial sampling rates due to an automatic acquisition system, which were collected by members of BAM Division 8.2, an additional data set in survey wheel acquisition mode was acquired as part of the thesis. This manual measurement simulates the step from high spatial sampling rate data under controlled environments to on-site measurements with commonly relatively large trace spacing and low signal-to-noise ratios. In order to obtain orthogonal polarizations, data in both antenna orientations perpendicular broadside and parallel broadside were conducted.

Prior to the actual attribute analysis, the dewowed and background removed data were investigated to identify reflections within the six data sets. The events were directly extracted, and the hyperbolic reflections were selected without any automated process. Attributes were applied to the hyperbola cutouts and to the amplitudes along the hyperbola within both polarizations ($\boldsymbol{E}_{inc}$-parallel and $\boldsymbol{E}_{inc}$-perpendicular). Conversion from antenna orientation to polarization depends on the angle between the antenna dipole axis and the long axis of the cylinder.

Three attributes were obtained which provide promising results for both scanner and manual measurements under controlled conditions: Maximum absolute amplitude, cumulative energy and apex amplitude. Indeed, the combination of the first two results in a larger accuracy (97.4 %) compared to the individual investigation. Further, the maximum value within the mean computed over a time range along the hyperbola, the peak-to-peak ratio and the hyperbola fitting velocity show limited potential as they only reveal a decision line for high spatial sampling rates. As these attributes were related to the TWT the quality of the derived features is limited as the time zero removal was not applied to the data. Nevertheless, the results are promising, and further investigation has to be performed to increase the number of samples and to validate the observations. Autocorrelation functions and the analysis of the creeping wave did not provide encouraging results for all measurements. The extracted features require surveys where both orthogonal polarizations exist and the Nyquist sampling theorem is not violated to strongly. Therefore, the measurement effort could not be reduced. Future work should try to generate features which eliminate the need for one of the polarizations.

None of the presented attributes were able to classify the reflection in the on-site data set collected at a Bridge in Northwestern Germany. One reason is the strong interference between the hyperbolic reflections. Accordingly, attributes which are independent of the amplitude should be in the focus of future work. This could be for example geometry based attributes, i.e., the velocity of the hyperbolic signature, or frequency based attributes. Another issue is the gain which was applied prior to storing the data because the amplitudes are distorted and do not present the proper relations.

Only one manual measurement representing tendon ducts was evaluated indicating moderate classifications. As a consequence, the potential of the attributes for data with low spatial sampling rates should be assessed further. From this, potential error sources with respect to the preprocessing can be analyzed, i.e. background removal.

Future work should also focus on the relationship between the individual attributes in order to analyze the gained information content with respect to the computational effort. This could eliminate the calculation of one of them or could improve the classification quality. In addition, the entire analysis should be expanded to other intrusions present in concrete such as hollow bodies, cables, voids and the like. An approach could be to incorporate phase attributes as they provide valuable information about the material of the object. Also, additional measurements should be conducted with multiple frequencies to analyze the impact of the scattering response on the amplitude based attributes.

Amplitude and traveltime investigations can sometimes be used the visually identify the reflector origin from the shape and location. Nevertheless, due to the large data sets the need for automation arouse in recent years. Many researchers have presented approaches to automatically extract the hyperbola within a data set. This automation process could be extended to incorporate also the extracted features because the identification and selection of the hyperbola is the most challenging part. For nonmetallic intrusions the automation process could also consider attributes which classify the material of the object.

Concluding, the presented reflector analysis can sufficiently extract features for three out of the nine tested attributes. In addition, the apex amplitude shows the potential to subdivide the group of rebars according to their diameter range. The feature extraction can be performed without a large computational effort and therefore, it is a valuable tool for automation. In fact, evaluating data with low spatial sampling rates, and specifically on-site data, is still a challenge.

Bibliography

Akroyd, T. N. W. (1962). *Concrete*, chapter 1 - The Properties of Concrete, pages 1 – 45. Pergamon.

Al-Zayer, R. (2005). *Influence of the Host Medium on GPR Polarization Characteristics of a Cylinder*. Colorado School of Mines. Department of Geophysics.

Aldami, H. A. N. and Karim, H. (2011). *GPR Data Simulation for Engineering Investigations in Shallow Regions*. PhD thesis, University of Technology, Building and Construction Engineering Department, Iraq.

Almeida, J., Camara, J., Friedrich, T., Voumard, J.-M., Bousias, S. N., Haugerud, S. A., M., K., Reineck, K. H., and Shiratani, H. (2005). Post-tensioning in buildings. fib Bulletin No. 31, International Federation for Structural Concrete.

Alteköster, C. A. (2004). *Untersuchungen zur Reproduzierbarkeit von Bodenradarmessungen*. PhD thesis, University of Bonn.

Annan, A. P. (2001). *Ground Penetrating Radar - Workshop Notes*. Sensors & Software Inc., Ontario, Canada.

Annan, A. P. (2012). *Near-Surface Geophysics*, chapter 11 - Ground-Penetrating Radar, pages 357–438. Society of Exploration Geophysicists.

Annan, P., Cosway, S., and DeSouza, T. (2002). Application of GPR to map concrete to delineate embedded structural elements & defects. In *Proceedings of SPIE - The International Society for Optical Engineering*, volume 4758 of *Ninth International Conference on Ground Penetrating Radar (GPR2002)*, pages 359–364.

Baker, G., Jordan, T., and Pardy, J. (2007). *Special Paper*, volume 432, chapter - An introduction to ground penetrating radar (GPR), pages 1–18. Geological Society of America.

Balanis, C. A. (2012). *Advanced engineering electromagnetics*. John Wiley & Sons, 2nd edition.

Balanis, C. A. (2016). *Antenna Theory: Analysis and Design.* John Wiley & Sons, 4th edition.

Benedetto, A. and Pajewski, L. (2015). *Civil Engineering Applications of Ground Penetrating Radar.* Springer, Cham.

Bertram, U. (2017). Untersuchungen zur Bestimmung des Bewehrungsdurchmessers mit Radar durch einen Datenfusionsansatz. Bachelor thesis, Technische Universität Berlin.

Blindow, N., Eisenburger, D., Illich, B., Petzold, H., and Richter, T. (2007). *Environmental Geology: Handbook of Field Methods and Case Studies*, chapter 4.5 - Ground Penetrating Radar, pages 283–335. Springer Berlin Heidelberg.

Blindow, N. and Kirsch, R. (2009). *Groundwater Geophysics: A Tool for Hydrogeology*, chapter 7 - Ground penetrating radar, pages 227–252. Springer Berlin Heidelberg.

Böniger, U. and Tronicke, J. (2010). Improving the interpretability of 3D GPR data using targetspecific attributes: application to tomb detection. *Journal of Archaeological Science*, 37(2):360 – 367.

Bradski, G. (2000). The OpenCV Library. *Dr. Dobb's Journal of Software Tools.*

Bungey, J., Millard, S., and Shaw, M. (1994). The influence of reinforcing steel on radar surveys of concrete structures. *Construction and Building Materials*, 8(2):119 – 126.

Cassidy, N. J. (2009). *Ground Penetrating Radar Theory and Applications*, chapter 5 - Ground Penetrating Radar Data Processing, Modelling and Analysis, pages 141 – 176. Elsevier, Amsterdam.

Castro, D., Reis Júnior, J. R., Teixeira, W. L. E., Silva, V. d. A., and Filho, F. P. L. (2014). Ground-penetrating radar imaging techniques applied in 3D environment: Example in inactive dunes. *Brazilian Journal of Geophysics*, 32:273–289.

Chang, C. W., Lin, C. H., and Lien, H. S. (2009). Measurement radius of reinforcing steel bar in concrete using digital image GPR. *Construction and Building Materials*, 23(2):1057 – 1063.

Coulomb (1953). *Grundversuche der Physik in Historischer Darstellung: Erster Band: Von den Fallgesetzen bis zu den elektrischen Wellen*, chapter - Das Coulombsche Gesetz (1785–1786), pages 97–104. Springer Berlin Heidelberg, Berlin, Heidelberg.

Daniels, D. J. (2009). *Ground Penetrating Radar Theory and Applications*, chapter 4 - Antennas, pages 99 – 139. Elsevier, Amsterdam.

Davis, J. L. (1990). *Wave Propagation in Electromagnetic Media*, chapter 7 - Time-Varying Electromagnetic Fields, pages 187–207. Springer New York, New York, NY.

Dérobert, X., Balayssac, J.-P., Sbartaï, Z. M., and Dumoulin, J. (2018). chapter 3 - electromagnetic methods. In Balayssac, J.-P. and Garnier, V., editors, *Non-Destructive Testing and Evaluation of Civil Engineering Structures*, pages 87 – 137. Elsevier.

DIN EN 12620:2008-07 (2008). Gesteinskörnungen für Beton; Deutsche Fassung EN 12620:2002+A1:2008. Beuth.

Dobbs, R. (1985). *Electromagnetic Waves*, chapter 7 - Generation of electromagnetic waves, pages 89–103. Springer Netherlands, Dordrecht.

Dos Santos, V. R. N., Al-Nuaimy, W., Porsani, J. L., Hirata, N. S. T., and Alzubi, H. S. (2014). Spectral analysis of ground penetrating radar signals in concrete, metallic and plastic targets. *Journal of Applied Geophysics*, 100:32 – 43.

Dou, Q., Wei, L., Magee, D., and Cohn, A. (2016). Real-time hyperbola recognition and fitting in GPR data. *IEEE Transactions on Geoscience and Remote Sensing*, PP:1–12.

Doğan, M. and Turhan-Sayan, G. (2016). Preprocessing of A-scan GPR data based on energy features. In *SPIE Defense + Security.*

Eisenmann, D., Margetan, F., Chiou, C.-P., Roberts, R., and Wendt, S. (2013). Ground penetrating radar applied to rebar corrosion inspection. *AIP Conference Proceedings*, 1511:1341–1348.

Eisenmann, D., Margetan, F. J., Chiou, C.-P., Ellis, S., Huang, T., and Tan, J. Y. (2017). Effects of position, orientation, and metal loss on GPR signals from structural rebar. *AIP Conference Proceedings*, 1806(1):080005.

Ellingson, S. W. (2018). *Electromagnetics*, volume 1. VT Publishing, Blacksburg, Virginia.

Everett, M. E. (2013). *Near-Surface Applied Geophysics*, chapter 9 - Ground-penetrating radar, page 239278. Cambridge University Press.

Farrar, C. and Worden, K. (2013). *Structural Health Monitoring A Machine Learning Perspective.* John Wiley & Sons, Ltd.

Feynman, R. P., Leighton, R. B., and Sands, M. (2010). *The Feynman lectures on physics; New millennium ed.*, volume II. Basic Books, New York, NY.

Forte, E., Pipan, M., Casabianca, D., Di Cuia, R., and Riva, A. (2010). 2D and 3D GPR imaging and characterization of a carbonate hydrocarbon reservoir analogue. *Proceedings of the 13th Internarional Conference on Ground Penetrating Radar, GPR 2010.*

Franz, W. and Klante, K. (1959). Diffraction by surfaces of variable curvature. *IRE Transactions on Antennas and Propagation*, 7(5):68–70.

Geophysical Survey Systems, Inc. (2017). *SIR® 20 Manual.* Geophysical Survey Systems, Inc., Nashua, New Hampshire.

Geßner, S., Niedermeier, R., Ahrens, M. A., Hegger, J., Fischer, O., and Mark, P. (2016). *Beton Kalender 2017*, chapter I - Spannbetonbau Entwicklung, Bemessung und Konstruktion, pages 1–100. John Wiley & Sons, Ltd.

Gierens, L. (2020). Research module in applied geophysics (unpublished). RWTH Aachen, Joint Masters Programme in Applied Geophysics.

Greiner, W. (1998). *Classical Electrodynamics*, chapter 16 - Electromagnetic Waves in Matter, pages 316–332. Springer New York, New York, NY.

Griffiths, D. J. (2013). *Introduction to electrodynamics; 4th ed.* Pearson, Boston, MA.

He, X.-Q., Zhu, Z.-Q., Liu, Q.-Y., and Lu, G.-Y. (2009). Review of GPR rebar detection. *Progress in Electromagnetics Research Symposium*, 1.

Huang, H., Shi, J., Wang, F., Zhang, D., and Zhang, D. (2020). Theoretical and experimental studies on the signal propagation in soil for wireless underground sensor networks. *Sensors*, 20(9).

Hum, S. V. (2020). Radio and microwave wireless systems. `http://www.waves.utoronto.ca/prof/svhum/ece422/notes/`. last access: 18.06.2020.

Hunter, J. D. (2007). Matplotlib: A 2D graphics environment. *Computing in Science Engineering*, 9(3):90–95.

Hyndman, R. and Athanasopoulos, G. (2018). *Forecasting: principles and practice.* OTexts, Melbourne, Australia, 2nd edition.

Kansu, M. (2013). An analogy between macroscopic and microscopic systems for Maxwell's equations in higher dimensions. *The European Physical Journal Plus*, 128.

Knott, E. F. (1993). *Radar cross section measurements.* Van Nostrand, Reinhold.

Lau, K. and Lasa, I. (2016). *Corrosion of Steel in Concrete Structures*, chapter 3 - Corrosion of prestress and post-tension reinforced-concrete bridges, pages 37 – 57. Woodhead Publishing, Oxford.

Leucci, G. (2012). Ground penetrating radar: an application to estimate volumetric water content and reinforced bar diameter in concrete structures. *Journal of Advanced Concrete Technology*, 10:411–422.

Li, Z., Leung, C., and Xi, Y. (2009). *Structural Renovation in Concrete.* CRC Press, London.

Ling, S. J., Moebs, W., and Sanny, J. (2016). *University Physics*, volume 2. OpenStax, Houston, Texas. https://openstax.org/books/university-physics-volume-2/pages/1-introduction.

Lovejoy, D. (1993). *Magnetic Particle Inspection: A practical guide*, chapter 13 - Basic electromagnetic field theory, pages 345–386. Springer Netherlands, Dordrecht.

Millard, S., Shaari, A., and Bungey, J. (2002). Field pattern characteristics of GPR antennas. *NDT & E International*, 35:473–482.

Milsom, J. and Eriksen, A. (2003). Field geophysics, 3rd Edition. *Environmental & Engineering Geoscience*, 19:205–206.

Morris, I., Abdel-Jaber, H., and Glisic, B. (2019). Quantitative attribute analyses with ground penetrating radar for infrastructure assessments and structural health monitoring. *Sensors*, 19:1637.

Morris, I. and Glisic, B. (2017). GPR attribute analysis for material property identification. In *2017 9th International Workshop on Advanced Ground Penetrating Radar (IWAGPR)*, pages 1–5.

Naaman, A. (2001). Reinforced concrete. In Buschow, K. J., Cahn, R. W., Flemings, M. C., Ilschner, B., Kramer, E. J., Mahajan, S., and Veyssire, P., editors, *Encyclopedia of Materials: Science and Technology*, pages 8095 – 8109. Elsevier, Oxford.

Niu, L. (2018). A review of the application of logistic regression in educational research: common issues, implications, and suggestions. *Educational Review*, pages 1–27.

Osipov, A. V. and Tretyakov, S. A. (2017). *Modern Electromagnetic Scattering Theory with Applications.* John Wiley & Sons, 1st edition.

Park, B., Kim, J., Lee, J., Kang, M.-S., and An, Y.-K. (2018). Underground object classification for urban roads using instantaneous phase analysis of ground-penetrating radar (GPR) data. *Remote Sensing*, 10:1417.

Park, H.-A. (2013). An introduction to logistic regression: From basic concepts to interpretation with particular attention to nursing domain. *Journal of Korean Academy of Nursing*, 43:154–164.

Pedregosa, F., Varoquaux, G., Gramfort, A., Michel, V., Thirion, B., Grisel, O., Blondel, M., Prettenhofer, P., Weiss, R., Dubourg, V., Vanderplas, J., Passos, A., Cournapeau, D., Brucher, M., Perrot, M., and Duchesnay, E. (2011). Scikit-learn: Machine learning in Python. *Journal of Machine Learning Research*, 12:2825–2830.

Poplavko, Y. M. (2019). *Electronic Materials*, chapter 7 - Dielectrics, pages 287 – 408. Elsevier.

Qiao, L., Qin, Y., Ren, X., and Wang, Q. (2015). Identification of buried objects in GPR using amplitude modulated signals extracted from multiresolution monogenic signal analysis. *Sensors*, 15:30340–30350.

Queiroz, F. A. A., Vieira, D. A. G., Travassos, X. L., and Pantoja, M. F. (2012). Feature extraction and selection in ground penetrating radar with experimental data set of inclusions in concrete blocks. In *11th International Conference on Machine Learning and Applications*, volume 2, pages 48–53.

Radzevicius, S. and Daniels, J. (2000). Ground penetrating radar polarization and scattering from cylinders. *Journal of Applied Geophysics*, 45:111–125.

Reynolds, J. M. (1997). *An Introduction to Applied and Environmental Geophysics.* John Wiley & Sons.

Ristic, A. V., Petrovacki, D., and Govedarica, M. (2009). A new method to simultaneously estimate the radius of a cylindrical object and the wave propagation velocity from GPR data. *Computers & Geosciences*, 35(8):1620 – 1630.

Roberts, R. L. (1994). *Analysis and Theoretical Modeling of GPR Polarization Data.* PhD thesis, The Ohio State University.

Roberts, R. L. and Daniels, J. J. (1996). Analysis of GPR polarization phenomena. *Journal of Environmental and Engineering Geophysics*, 1(2):139–157.

Sahamitmongkol, R. (2010). Effect of scanning direction on amplitude of reflected pulse radar from steel bar. *Journal of Building Appraisal*, 6.

Sangoju, B. (2017). Estimation of rebar diameter in concrete structural elements using ground penetrating radar. In *Indian National Seminar & Exhibition on Non-Destructive Evaluation NDE 2015, Hyderabad, India (NDE-India 2015)*.

Scheers, B. (2001). *Ultra-Wideband Ground Penetrating Radar, with Application to the Detection of Anti Personnel Landmines*. PhD thesis, Université catholique de Louvain, Laboratoire d'Hyperfréquences.

Schubert, M. (2011). Entwurf, Aufbau und Test einer universellen Steuereinheit für zeitkritische Anwendungen bei zerstörungsfreien Prüfungen im Bauwesen. Bachelor thesis, Technische Universität Berlin.

Sharma, G. K. and Kind, T. (2018). Distinction of tendon ducts and rebars by GPR reflection signal patterns. In *2018 17th International Conference on Ground Penetrating Radar (GPR)*, pages 1–4.

Shihab, S. and Al-Nuaimy, W. (2005). Radius estimation for cylindrical objects detected by ground penetrating radar. *Subsurface Sensing Technologies and Applications*, 6:151–166.

Soutsos, M., Bungey, J., Millard, S., Shaw, M., and Patterson, D. (2001). Dielectric properties of concrete and their influence on radar testing. *NDT & E International*, 34:419–425.

Stehno, G. (1981). *Baustoffe und Baustoffprfung*. Springer-Verlag Wien.

Syambas, N., Hendrawan, T., Sugihartono, and Suksmono, A. (2009). Interpretation target pattern of a buried basic object on surface ground penetrating radar system. *International Journal on Electrical Engineering and Informatics*, 1:553 – 558.

Szymczyk, M. and Szymczyk, P. (2013). Preprocessing of GPR data. *Image Process. Commun.*, 16:83–90.

Thidè, B. (2011). *Electromagnetic Field Theory*. Upsilon Books, Uppsala, Sweden.

Urone, P. P. and Hinrichs, R. (2012). *College Physics*. OpenStax, Houston, Texas. `https://openstax.org/books/college-physics/pages/1-introduction-to-science-and-the-realm-of-physics-physical-quantities-and-units`.

Utsi, E. C. (2017). *Ground Penetrating Radar Theory and Practice*. Elsevier (Butterworth-Heinemann), 1st edition.

Utsi, V. and Utsi, E. (2004). Measurement of reinforcement bar depths and diameters in concrete. In *Proceedings of the Tenth International Conference on Grounds Penetrating Radar, 2004.*, pages 659 – 662.

Van Gestel, J.-P. and Stoffa, P. (2001). Application of alford rotation to ground-penetrating radar data. *Geophysics*, 66.

Van Rossum, G. and Drake, F. L. (2009). *Python 3 Reference Manual*. CreateSpace, Scotts Valley, CA.

Virtanen, P., Gommers, R., Oliphant, T. E., Haberland, M., Reddy, T., Cournapeau, D., Burovski, E., Peterson, P., Weckesser, W., Bright, J., van der Walt, S. J., Brett, M., Wilson, J., Jarrod Millman, K., Mayorov, N., Nelson, A. R. J., Jones, E., Kern, R., Larson, E., Carey, C., Polat, İ., Feng, Y., Moore, E. W., Vand erPlas, J., Laxalde, D., Perktold, J., Cimrman, R., Henriksen, I., Quintero, E. A., Harris, C. R., Archibald, A. M., Ribeiro, A. H., Pedregosa, F., van Mulbregt, P., and Contributors SciPy 1. 0 (2020). SciPy 1.0: Fundamental Algorithms for Scientific Computing in Python. *Nature Methods*, 17:261–272.

Visser, H. J. (2012). *Antenna theory and application.* John Wiley & Sons, Ltd.

Wang, J. H. (2018). chaper 23 - lifecycle cost and performance analysis for repair of concrete tunnels. In Pacheco-Torgal, F., Melchers, R. E., Shi, X., Belie, N. D., Tittelboom, K. V., and Sáez, A., editors, *Eco-Efficient Repair and Rehabilitation of Concrete Infrastructures*, Woodhead Publishing Series in Civil and Structural Engineering, pages 637 – 672. Woodhead Publishing.

Wu, Y.-F. (2006). New avenue of achieving ductility for reinforced concrete members. *Journal of Structural Engineering*, 132(9):1502–1506.

Yuan, C., Li, S., Cai, H., and Kamat, V. (2018). GPR signature detection and decomposition for mapping buried utilities with complex spatial configuration. *Journal of Computing in Civil Engineering*, 32.

Zanzi, L. and Arosio, D. (2013). Sensitivity and accuracy in rebar diameter measurements from dual-polarized GPR data. *Construction and Building Materials*, 48:1293–1301.

Zhao, W., Forte, E., Pipan, M., and Tian, G. (2013). Ground penetrating radar (GPR) attribute analysis for archaeological prospection. *Journal of Applied Geophysics*, 97:107–117.

Zilch, K. and Zehetmaier, G. (2010). *Bemessung im konstruktiven Betonbau.* Nach DIN 1045-1 (Fassung 2008) und EN 1992-1-1 (Eurocode 2). Springer Berlin Heidelberg.

Appendix A

Materials and Methods

This Appendix contains additional information for the concrete specimens and extracted reflections.

Table A-1: Summary of the structural composition of the concrete specimens, $\varnothing$ corresponds to the diameter of the embedded object and h to the concrete cover thickness.

BAM code	Specimen code	Size [mm]	Rebar [mm]	Duct [mm]
PK 240	A	$1200 \times 1200 \times 200$	$\varnothing 10$ ($h = 30$), Mesh size 150; $\varnothing 6$ ($h = 164$), Mesh size 100	$\varnothing 65$ ($h = 90$)
PK 266	B	$2000 \times 800 \times 210$ $2000 \times 800 \times 330$ $2000 \times 800 \times 450$ $2000 \times 800 \times 570$	-	$\varnothing 80$ ($h = 60$), $\varnothing 80$ ($h = 130$), $\varnothing 80$ ($h = 180$), $\varnothing 80$ ($h = 240$)
PK 31	C	$2000 \times 1500 \times 500$	$\varnothing 12$ ($h = 30$), Mesh size 150; $\varnothing 12$ ($h = 458$), Mesh size 150	$\varnothing 86$ ($h = 160$)
PK 200	D	$1500 \times 1500 \times 660$	$\varnothing 28$ ($h = 60$, $h = 120$, $h = 180$, $h = 150$, $h = 90$	-

Table A-2: Summary for the coordinates of the extracted reflectors with the relationship between antenna orientation and the $\boldsymbol{E}_{inc}$-parallel polarization.

Survey code	Object Code	Profile Constant	Profile Direction	$\boldsymbol{E}_{inc}$-parallel
A	A-Duct	$x = 460$	$y \in [150, 220]$	PL
	A-Rebar 1	$y = 125$	$x \in [20, 100]$	PR
	A-Rebar 2	$y = 125$	$x \in [90, 160]$	PR
	A-Rebar 3	$y = 125$	$x \in [150, 220]$	PR
	A-Rebar 4	$y = 125$	$x \in [215, 315]$	PR
B-1	*B-1*-Duct 1	$y = 50$	$x \in [0, 270]$	PR
	B-1-Duct 2	$y = 50$	$x \in [200, 430]$	PR
	B-1-Duct 3	$y = 50$	$x \in [400, 630]$	PR
	B-1-Duct 4	$y = 50$	$x \in [620, 820]$	PR
C	*C*-Duct	$x = 700$	$y \in [50, 100]$	PL
	C-Rebar 1	$y = 140$	$x \in [20, 110]$	PR
	C-Rebar 2	$y = 140$	$x \in [90, 190]$	PR
	C-Rebar 3	$y = 140$	$x \in [170, 260]$	PR
	C-Rebar 4	$y = 140$	$x \in [240, 330]$	PR
	C-Rebar 5	$y = 140$	$x \in [320, 410]$	PR
	C-Rebar 6	$y = 140$	$x \in [380, 500]$	PR
D	*D*-Rebar 1	$y = 140$	$x \in [125, 270]$	PR
	D-Rebar 2	$y = 140$	$x \in [250, 400]$	PR
	D-Rebar 3	$y = 140$	$x \in [350, 550]$	PR
	D-Rebar 4	$y = 140$	$x \in [500, 650]$	PR
	D-Rebar 5	$y = 140$	$x \in [625, 770]$	PR
B-2	*B-2*-Duct 1	PR: $y = 5$ PL: $y = 50$	PR: $x \in [0, 80]$ PL: $x \in [0, 8]$	PR
	B-2-Duct 2	PR: $y = 5$ PL: $y = 50$	PR: $x \in [60, 180]$ PL: $x \in [6, 18]$	PR
	B-2-Duct 3	PR: $y = 5$ PL: $y = 50$	PR: $x \in [170, 270]$ PL: $x \in [17, 27]$	PR
	B-2-Duct 4	PR: $y = 5$ PL: $y = 50$	PR: $x \in [270, 361]$ PL: $x \in [27, 37]$	PR
E	*E*-Object 1	PR: $y = 5$ PL: $y = 100$	PR: $x \in [120, 159]$ PL: $x \in [6, 8]$	PR
	E-Object 2	PR: $y = 5$ PL: $y = 100$	PR: $x \in [160, 203]$ PL: $x \in [8, 11]$	PR
	E-Object 3	PR: $y = 5$ PL: $y = 100$	PR: $x \in [200, 242]$ PL: $x \in [10, 13]$	PR
	E-Object 4	PR: $y = 5$ PL: $y = 100$	PR: $x \in [100, 260]$ PL: $x \in [5, 13]$	PR
	E-Object 5	PR: $y = 5$ PL: $y = 100$	PR: $x \in [440, 590]$ PL: $x \in [22, 30]$	PR
	E-Object 6	PR: $y = 5$ PL: $y = 100$	PR: $x \in [700, 800]$ PL: $x \in [35, 40]$	PR

Appendix B

Results

This Appendix contains the results supporting the main ideas discussed within Chapter 6. First, the preprocessing results are presented, followed by the visualization of the reflection events extracted from the radargrams. Next, additional figures for the amplitude based attributes and the hyperbolic geometry related attribute are shown.

B-1 Preprocessing Results

This section contains the preprocessing results, i.e., dewowed and background removed radargrams for the structure scanner data sets *B-1*, *C* and *D* and for the manual measurements *B-2* and *E*.

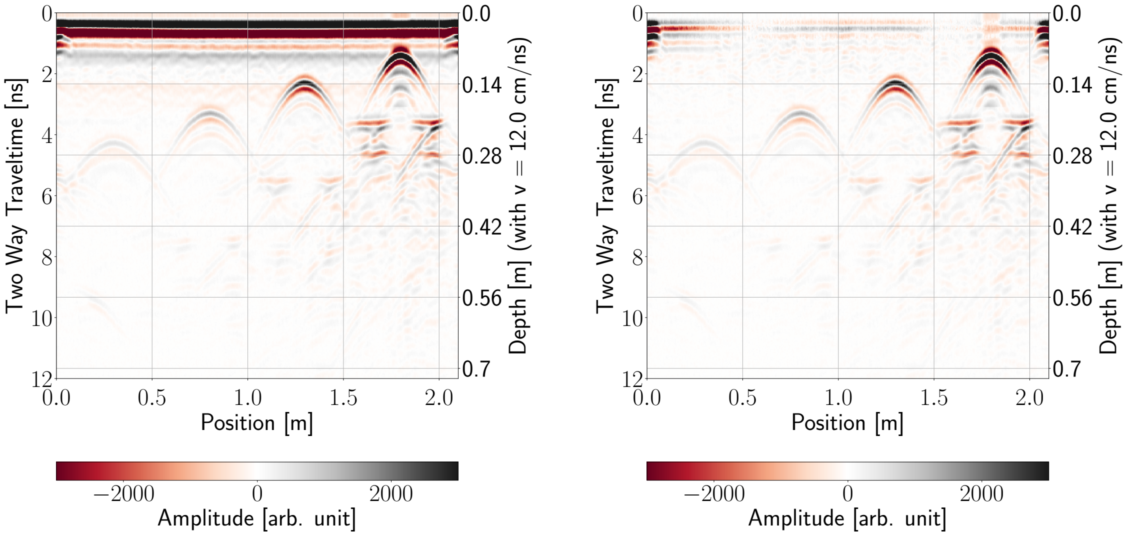

(a) Dewowed $\boldsymbol{E}_{inc}$-parallel data. **(b)** Background removed $\boldsymbol{E}_{inc}$-parallel data.

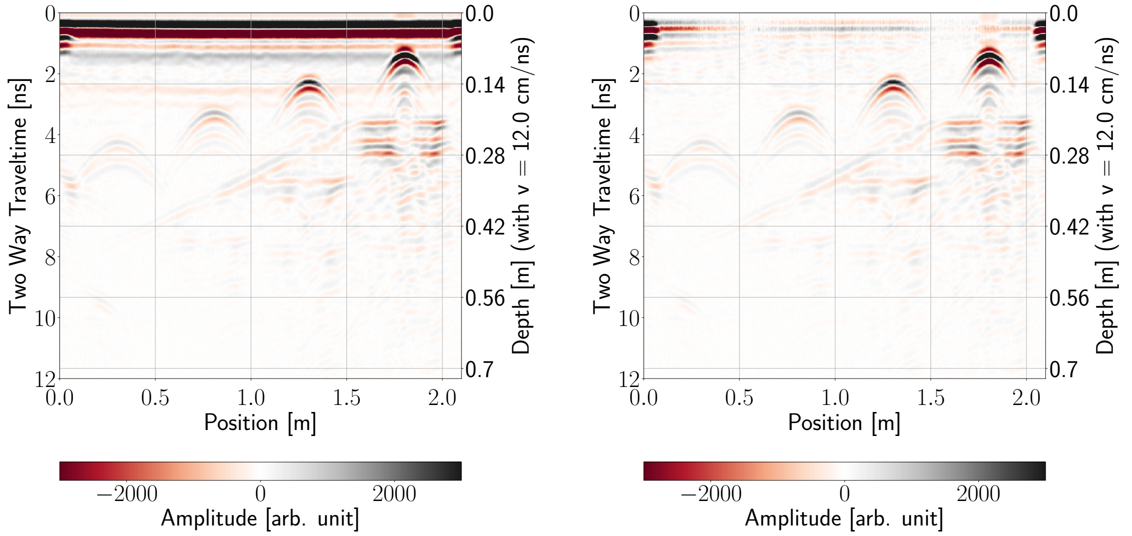

(c) Dewowed $\boldsymbol{E}_{inc}$-perpendicular data. **(d)** Background removed $\boldsymbol{E}_{inc}$-perpendicular data.

Figure B-1: Comparison of the dewowed and background removed radargrams of measurement *B-1* (y-axis index 50) for the two antenna orientations PR in a) and b) and PL in c) and d). The hyperbolic reflections correspond to tendon ducts with a diameter of 80 mm in different depths.

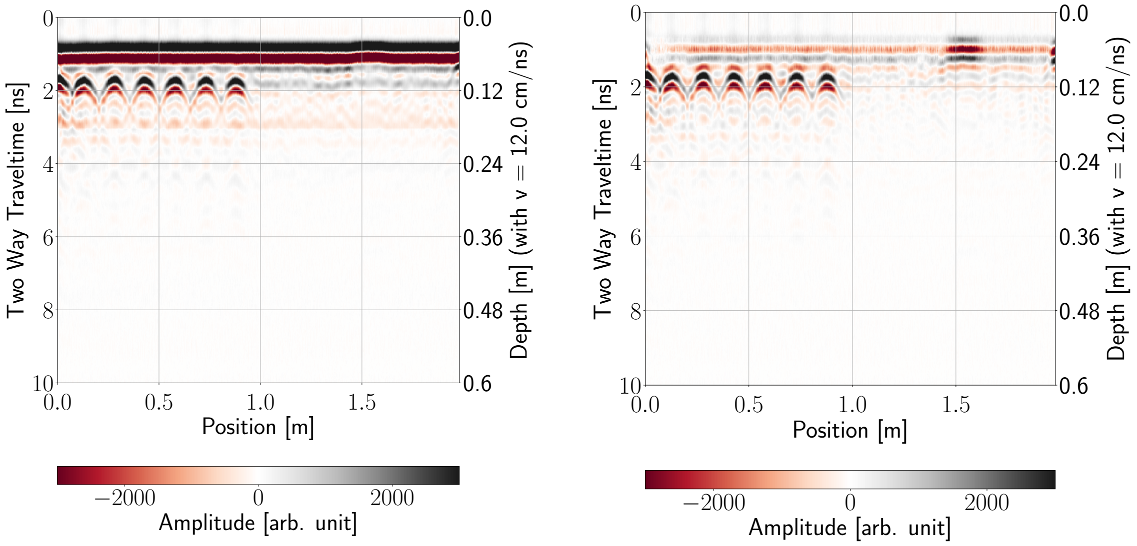

(a) Dewowed $\boldsymbol{E}_{inc}$-parallel data.

(b) Background removed $\boldsymbol{E}_{inc}$-parallel data.

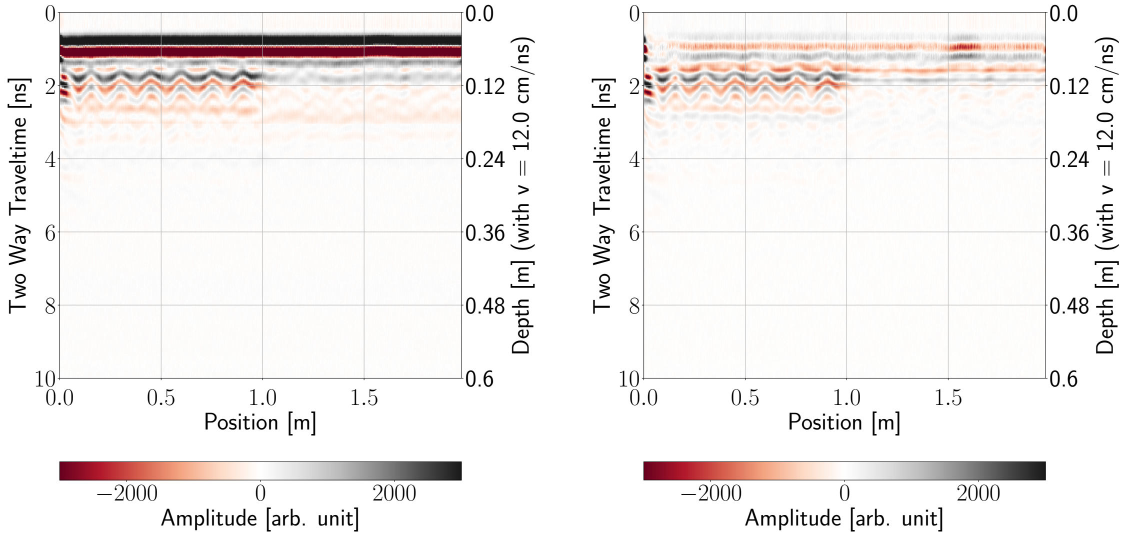

(c) Dewowed $\boldsymbol{E}_{inc}$-perpendicular data

(d) Background removed $\boldsymbol{E}_{inc}$-perpendicular data.

Figure B-2: Comparison of the dewowed and background removed radargrams of measurement C (y-axis index 140) for the two antenna orientations PR in a) and b) and PL in c) and d). The hyperbolic reflections correspond to the upper reinforcement mesh with a diameter of 12 mm.

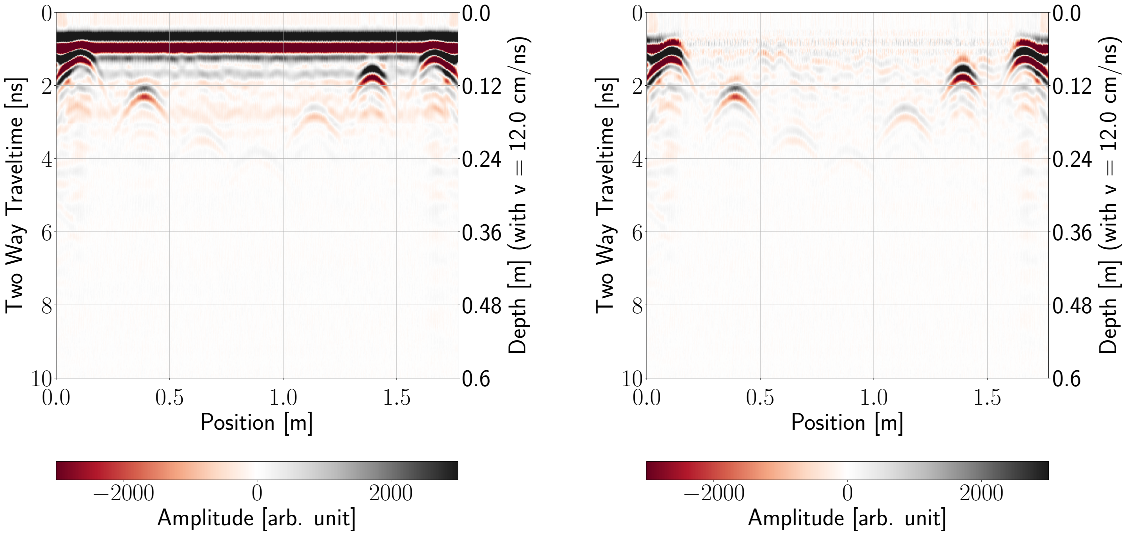

(a) Dewowed $\boldsymbol{E}_{inc}$-parallel data. **(b)** Background removed $\boldsymbol{E}_{inc}$-parallel data.

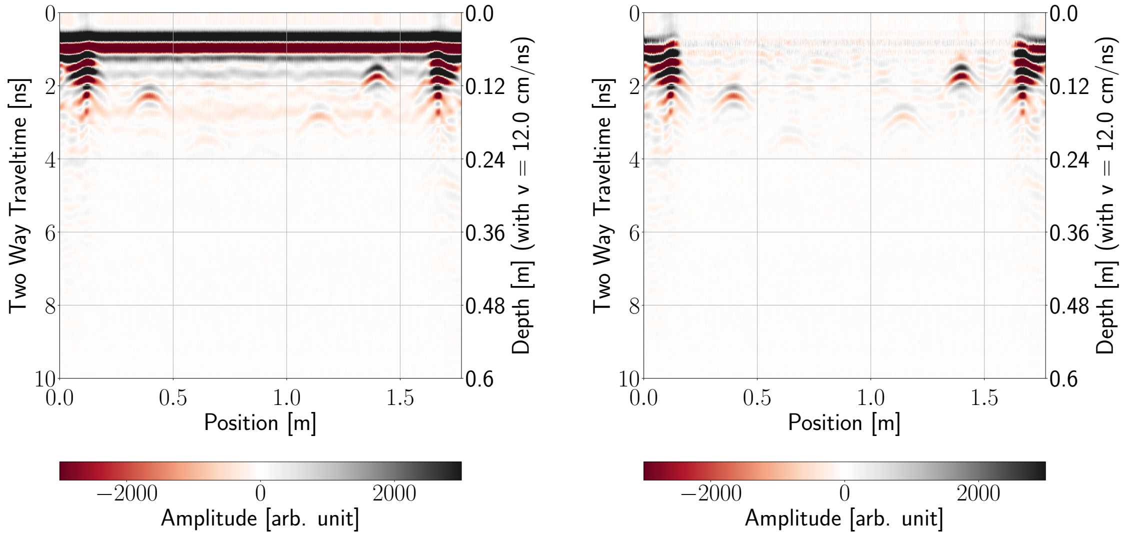

(c) Dewowed $\boldsymbol{E}_{inc}$-perpendicular data. **(d)** Background removed $\boldsymbol{E}_{inc}$-perpendicular data.

Figure B-3: Comparison of the dewowed and background removed radargrams of measurement *D* (y-axis index 140) for the two antenna orientations PR in a) and b) and PL in c) and d). The hyperbolic reflections correspond to rebars with a diameter of 28 mm in different depths.

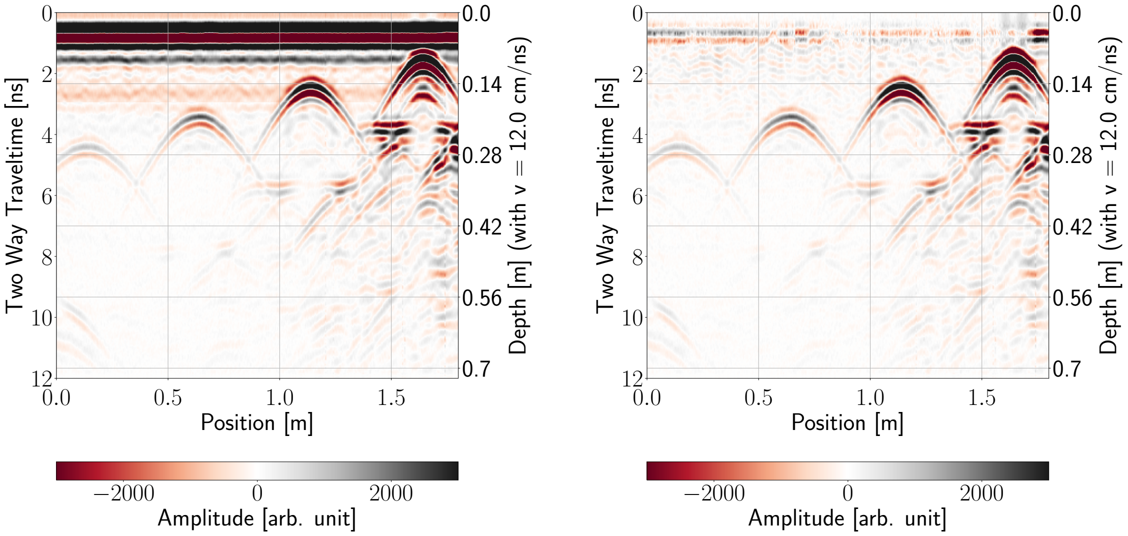

(a) Dewowed $\boldsymbol{E}_{inc}$-parallel data.

(b) Background removed $\boldsymbol{E}_{inc}$-parallel data.

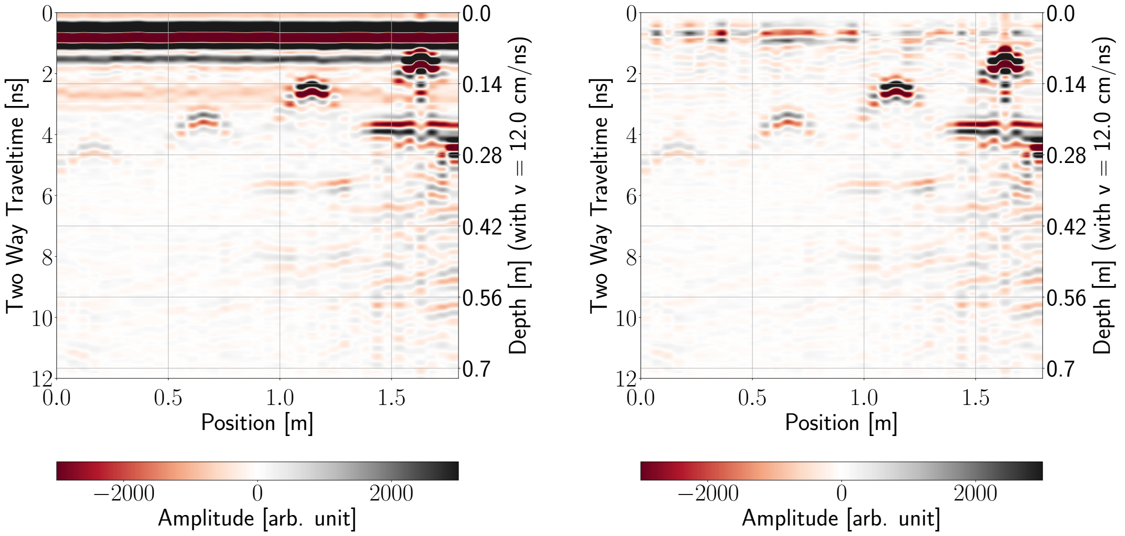

(c) Dewowed $\boldsymbol{E}_{inc}$-perpendicular data.

(d) Background removed $\boldsymbol{E}_{inc}$-perpendicular data.

Figure B-4: Comparison of the dewowed and background removed radargrams of measurement *B-2* for the two antenna orientations PR (y-axis index 5) in a) and b) and PL (y-axis index 50) in c) and d). The hyperbolic reflections correspond to tendon ducts with a diameter of 80 mm in different depths.

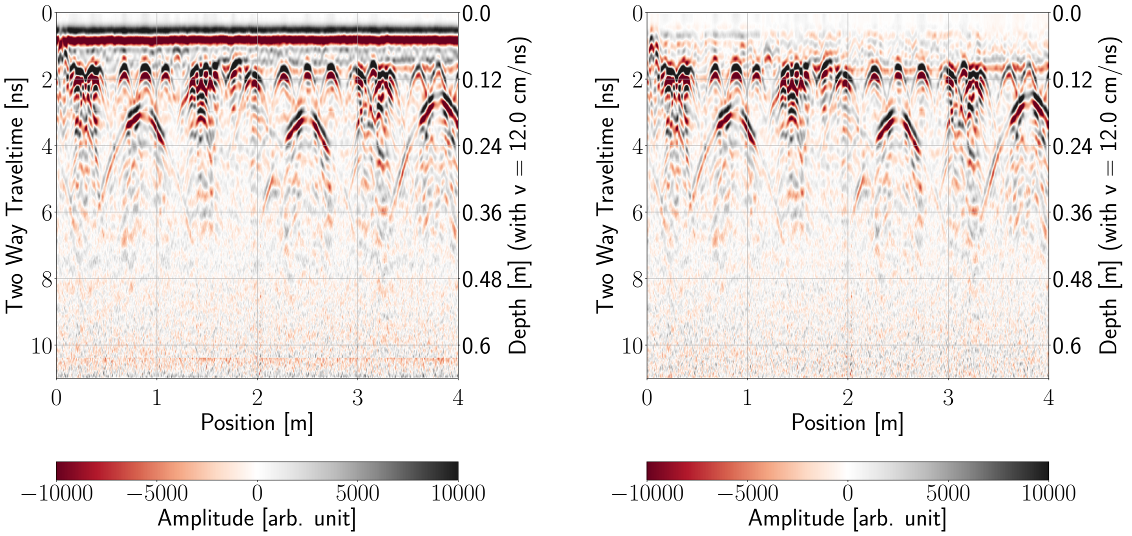

(a) Dewowed $\boldsymbol{E}_{inc}$-parallel data.

(b) Background removed $\boldsymbol{E}_{inc}$-parallel data.

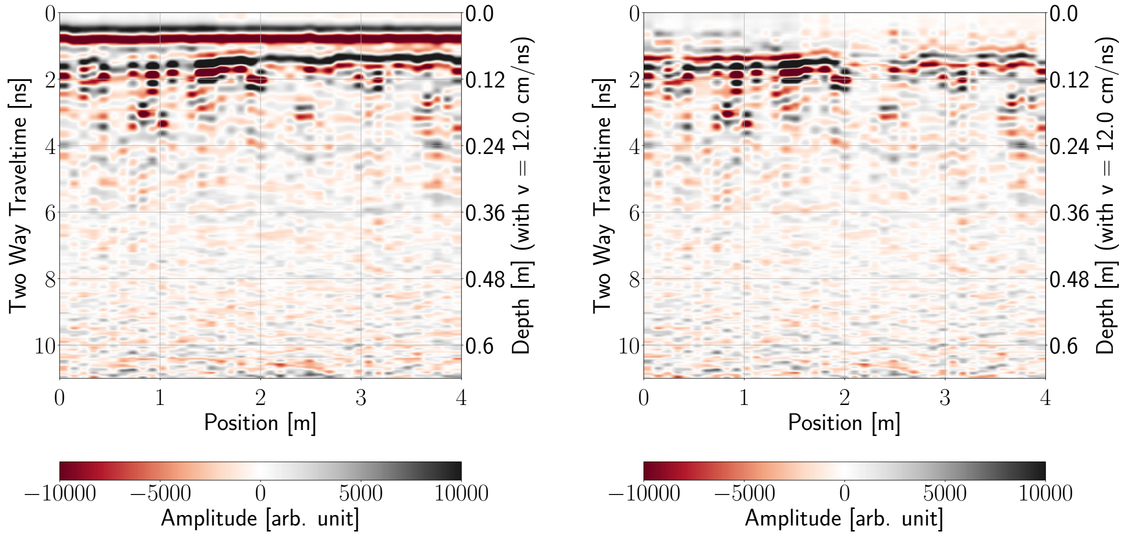

(c) Dewowed $\boldsymbol{E}_{inc}$-perpendicular data.

(d) Background removed $\boldsymbol{E}_{inc}$-perpendicular data.

Figure B-5: Comparison of the dewowed and background removed radargrams of measurement *E* for the two antenna orientations PR (y-axis index 5) in a) and b) and PL (y-axis index 100) in c) and d). The origin of the hyperbolic reflections is unknown.

B-2 Extracted Hyperbolic Reflections

In order to analyze the data with respect to feature extraction, the hyperbolic reflection events are chosen from (multiple) B-Scans. Accordingly, this section presents the considered events for all data sets with the associated abbreviations. The summary of the coordinates for the individual reflectors is presented in Appendix A.

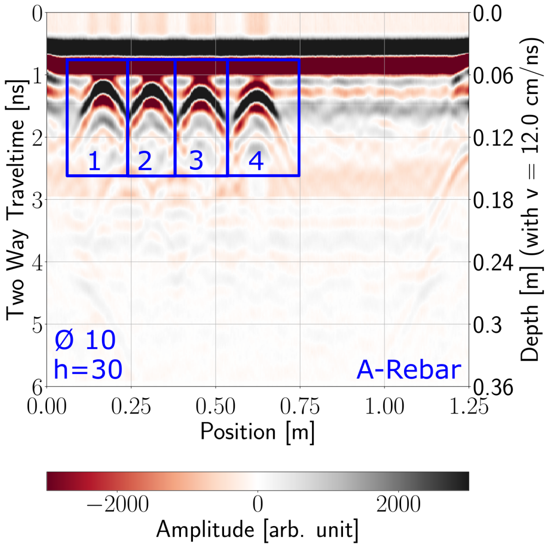

(a) Survey *A*.

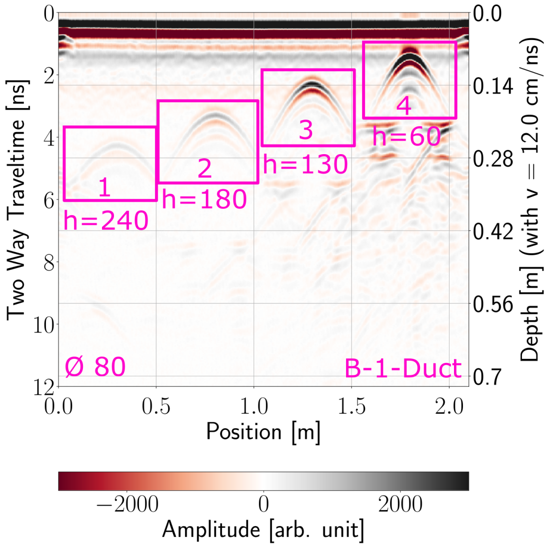

(b) Survey *B-1*.

Figure B-6: Dewowed radargrams ($\boldsymbol{E}_{inc}$-parallel) of measurements *A* and *B-1* with the extracted hyperbolic reflections annotated with blue and pink rectangles for rebars and tendon ducts, respectively.

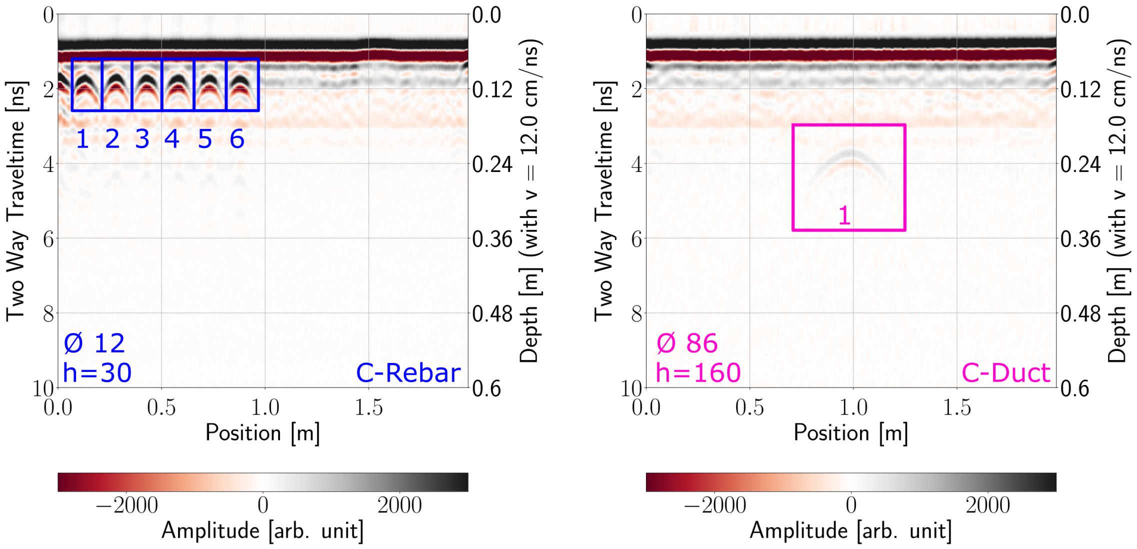

(a) Survey *C*.

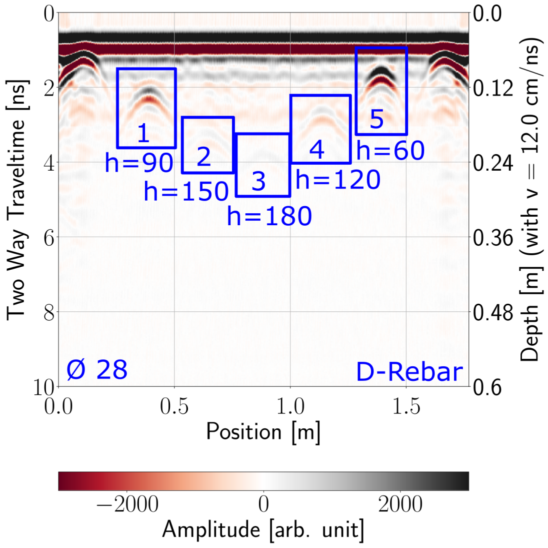

(b) Survey *D*.

Figure B-7: Dewowed radargrams ($\boldsymbol{E}_{inc}$-parallel) of measurements *C* and *D* with the extracted hyperbolic reflections annotated with blue and pink rectangles for rebars and tendon ducts, respectively.

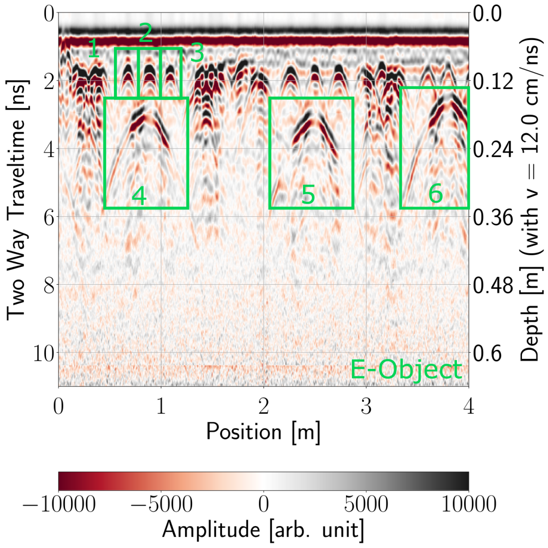

(a) Survey *E*.

Figure B-8: Dewowed radargrams ($\boldsymbol{E}_{inc}$-parallel) of measurement *E* with the extracted hyperbolic reflections annotated with green rectangles as the origin of the event is unknown.

B-3 Amplitude Based Attributes

This Chapter contains additional figures for the amplitude based attributes. In the beginning the areal representations of the reflection and propagation attributes for measurements *B-1*, *C*, *D*, *B-2* and *E* are shown. Next, the B-scans of the cumulative energy are presented for the same data sets. In addition, scatter plots illustrate the individual comparison with respect to each polarization and the relationship between the cumulative energy and the reflection attribute. Followed by the amplitude variance individually normalized and normalized with respect to $\boldsymbol{E}_{inc}$-parallel for the scanner measurements and *B-2*. The next section shows the orthogonal polarization amplitude ratios as a scatter plot for the $\boldsymbol{E}_{inc}$-parallel normalized time window around the apex of the hyperbola range. Further, the mean of the hyperbola range for both polarizations and a scatter plot of the apex position within the mean is presented. Afterwards, the autocorrelation functions for the scanner measurements are shown. In the end of the Chapter the peak-to-peak amplitude ratios of $\boldsymbol{E}_{inc}$-perpendicular as a function of $\boldsymbol{E}_{inc}$-parallel are provided.

The following table shows an overview for the evaluated attributes with a grading describing the potential of the extracted feature:

Table B-1: Summary of the results for the feature extraction where the numbers describe the classification potential: 1 classifies the measurements under controlled conditions, 2 classifies the high spatial sampling rate data sets, 3 provides geometry information and 4 did not provide sufficient geometry information.

Attribute	Result	Improvement
Maximum absolute amplitude	1	No time-variant gain; Combine with cumulative energy.
Total absolute trace area	3	-
Cumulative energy	1	No time-variant gain; Combine with maximum absolute amplitude.
Amplitude variance	2	Needs data with high signal-to-noise ratio and high spatial sampling rates.
Orthogonal polarization amplitude ratio	2 (1)	Only consider the apex amplitude.
Autocorrelation	4	-
Peak-to-peak ratio	2	Perform time zero removal; Consider $\boldsymbol{E}_{inc}$-perpendicular; Needs high spatial sampling rates.
Amplitude Reverberation	4	-
Geometry of the hyperbola	2	Perform time zero removal; Consider $\boldsymbol{E}_{inc}$-parallel; Needs high spatial sampling rates.

Reflection and Propagation Attributes

This Section shows the reflection (maximum absolute amplitude) and propagation (total absolute trace area) attributes for the scanner and manual measurements. The discussion from Section 6-2 applies here as well. Further, it can be observed that only the upper two tendon ducts for measurement *B-1* create distinct signals. Similarly, for D solely three rebars appear in each image whereas for C the tendon duct which would be expected as a horizontal anomaly in the center is not visible at all in the reflection attribute and ambiguous in the propagation attribute.

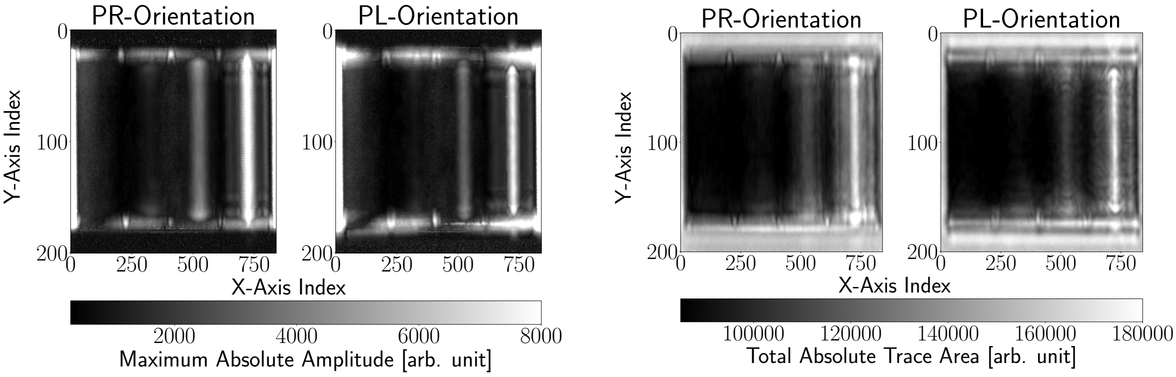

(a) Reflection attribute of *B-1*.

(b) Propagation attribute of *B-1*.

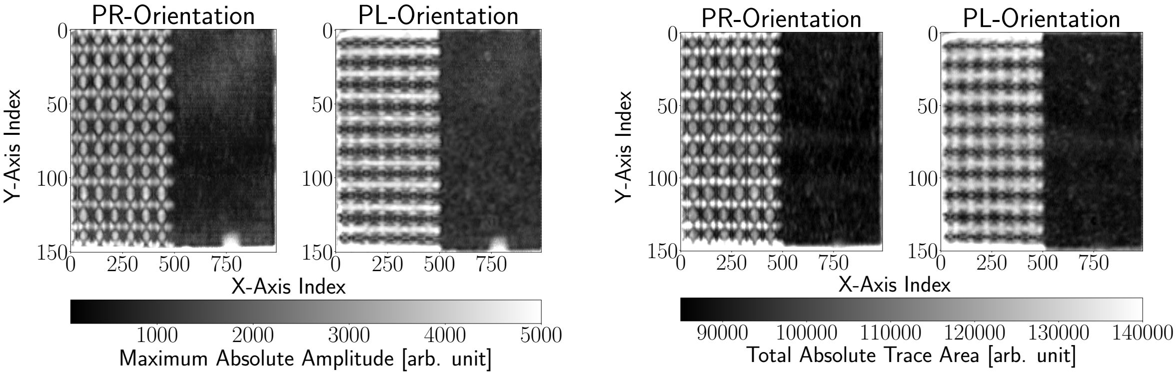

(c) Reflection attribute of *C*.

(d) Propagation attribute of *C*.

Figure B-9: Reflection and propagation attribute for measurements *B-1* in a) and b) and *C* in c) and d), with the PR antenna orientation on the left and the PL orientation on the right.

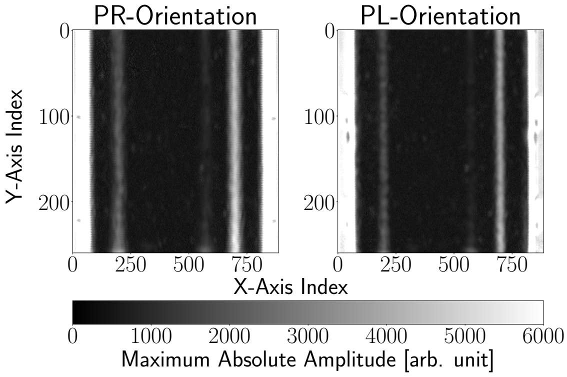

(a) Reflection attribute of *D*.

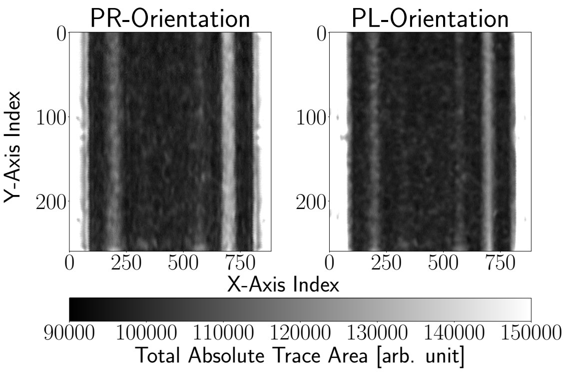

(b) Propagation attribute of *D*.

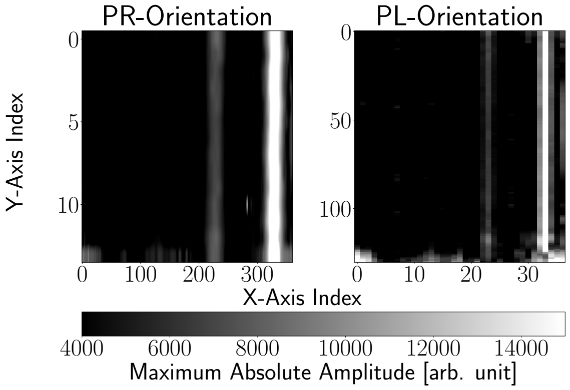

(c) Reflection attribute of *B-2*.

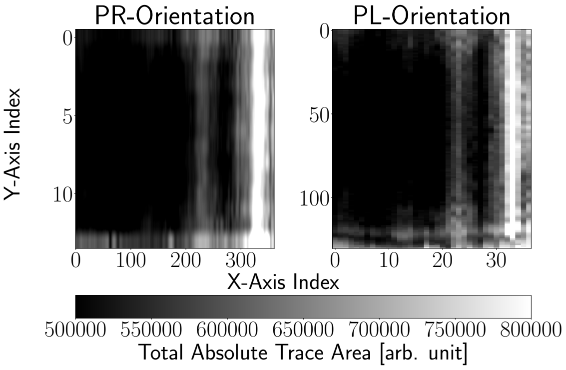

(d) Propagation attribute of *B-2*.

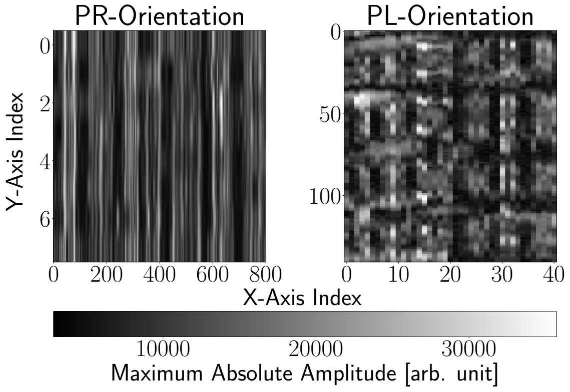

(e) Reflection attribute of *E*.

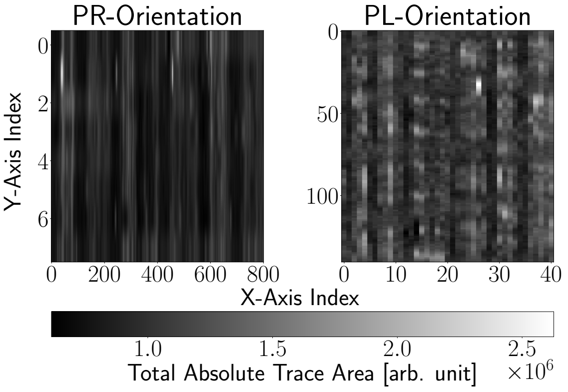

(f) Propagation attribute of *E*.

Figure B-10: Reflection and propagation attribute for measurements *D* in a) and b), *B-2* in c) and d) and *E* in e) and f) with the PR antenna orientation on the left and the PL orientation on the right.

Cumulative Energy

This section contains B-scans of the cumulative energy for the four scanner measurements and one manual measurement. Followed by the scatter plots relating the cumulative energy with the reflection attribute.

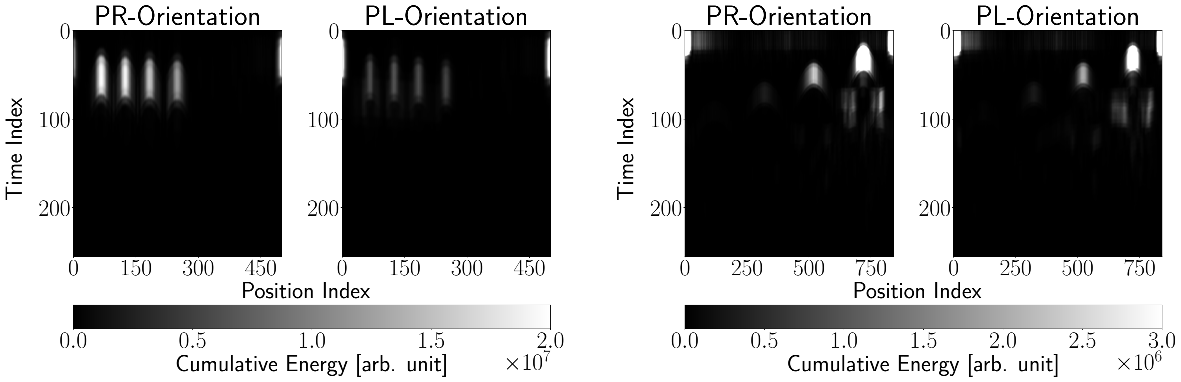

(a) Data set *A* for y index 125.

(b) Data set *B-1* for y index 50.

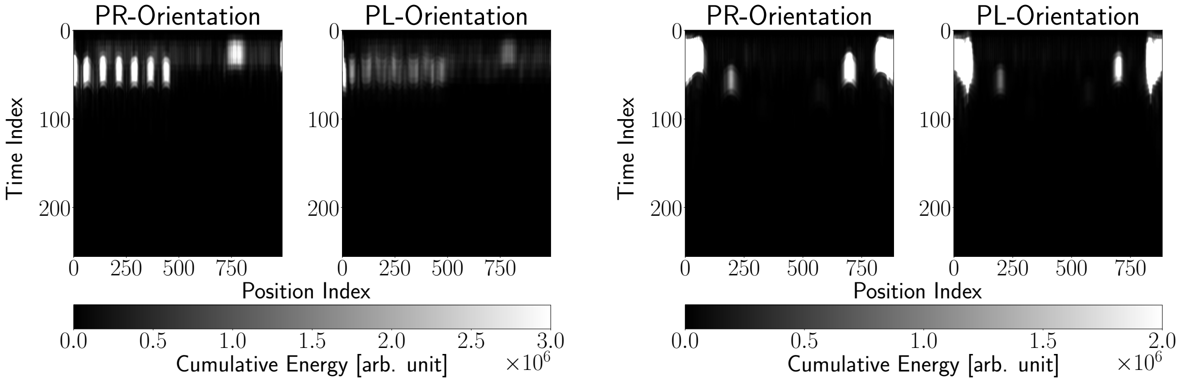

(c) Data set *C* for y index 140.

(d) Data set *D* for y index 140.

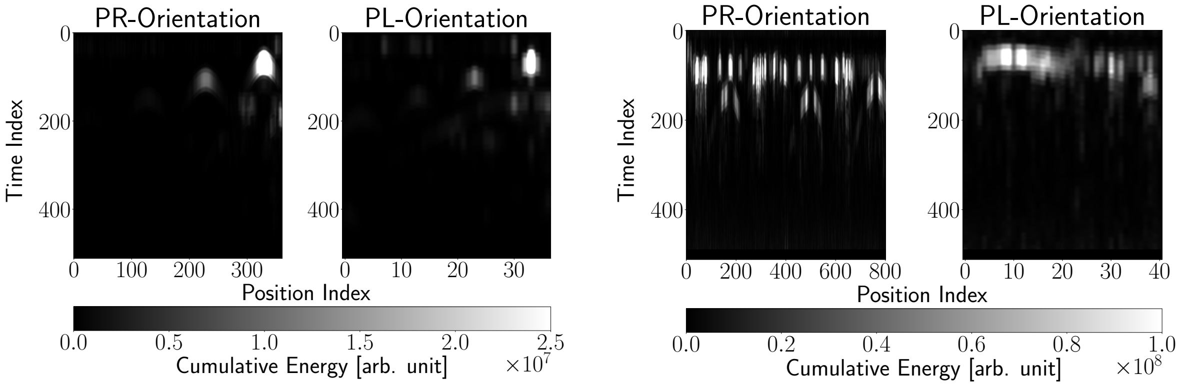

(e) Data set *B-2* for y index 5.

(f) Data set *E* for y index 5.

Figure B-11: Cumulative energy for PR and PL orientation B-scans for all data sets along the x-axis with constant y. White corresponds to large energies and therefore indicates the position of an event.

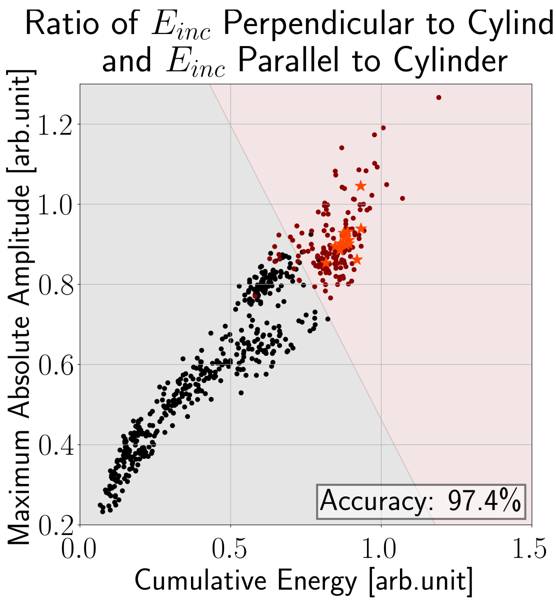

(a) Relationship for the ratio between the $\boldsymbol{E}_{inc}$-parallel and $\boldsymbol{E}_{inc}$-perpendicular components.

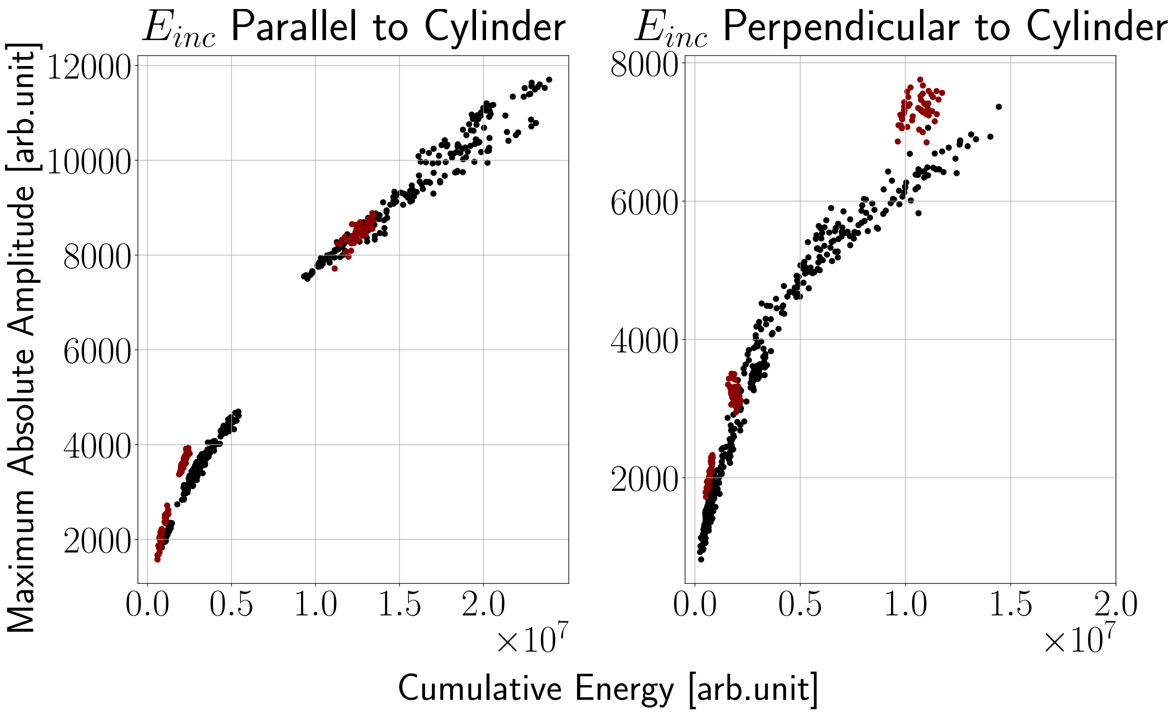

(b) Relationship for each individual polarization.

Figure B-12: Relationship between the cumulative energy and maximum absolute amplitude attribute. Red corresponds to tendon ducts and black to rebars (*A*, *B-1*, *C* and *D*). The shaded area in a) indicates the result of the logistic regression. Bright red stars show the data points for the manual measurement *B-2*.

Amplitude Variance

This section contains the amplitude variance for the scanner measurements and *B-2* for individual normalized amplitudes and amplitudes normalization with respect to $\boldsymbol{E}_{inc}$-parallel. It can be observed that the deepest structure (*B-1*-Duct 1) which lies in a depth of 240 mm is diffused. However, comparing it with the extremely disturbed amplitude variation of *D*-Rebar 2 (concrete cover $h = 150$ mm) indicates that the smaller diameter results in less robust amplitude variance. In addition, *D*-Rebar 4 shows a similar behavior and amplitude for both antenna polarizations and therefore, it could be falsely classified as tendon duct.

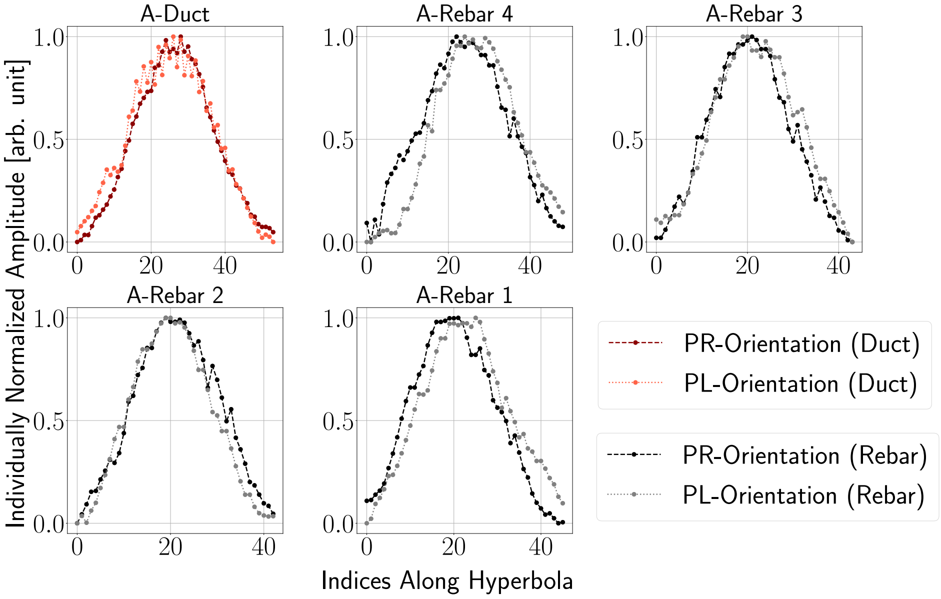

(a) Individual normalization for *A*.

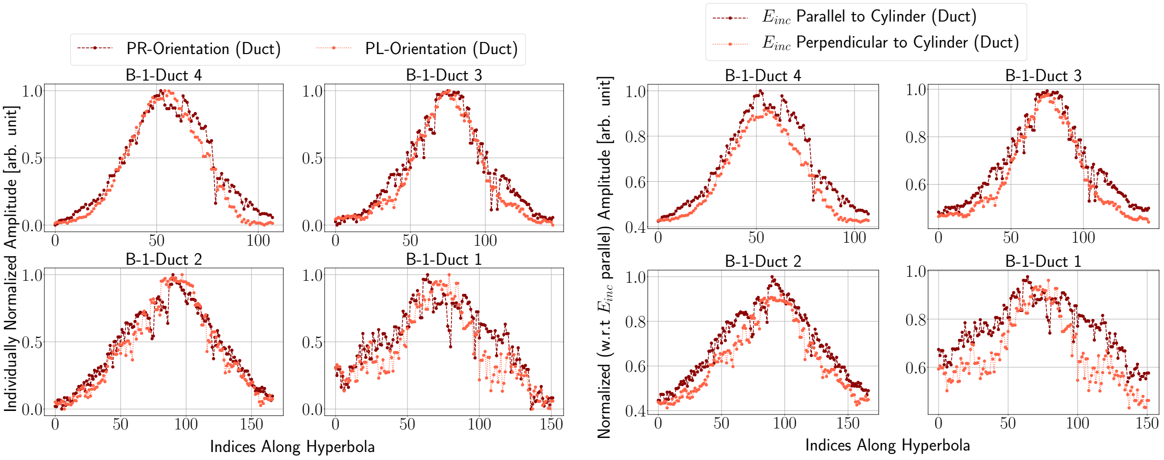

(b) Individual normalization for *B-1*.

(c) Normalization with respect to $\boldsymbol{E}_{inc}$-parallel for *B-1*.

Figure B-13: Amplitude variance for measurements *A* a) and *B-1* b) and c), where red curves correspond to tendon ducts and black curves to rebar reflections.

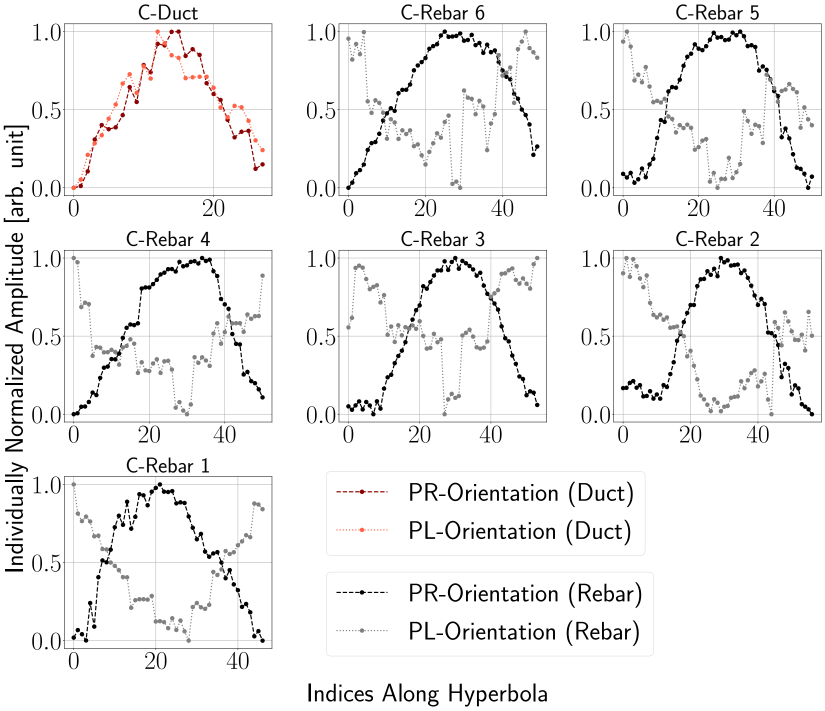

(a) Individual normalization for *C*.

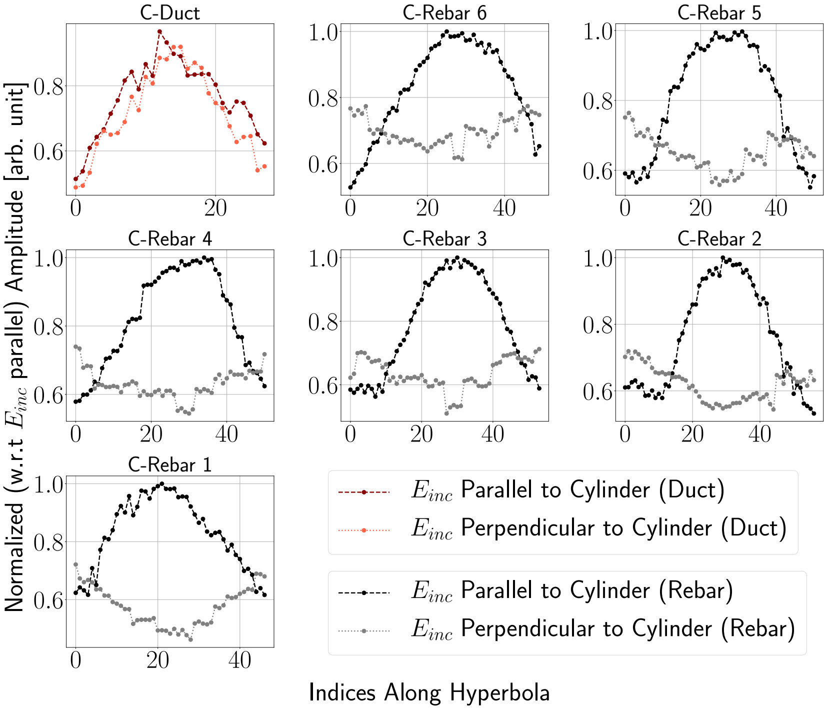

(b) Normalization with respect to $\boldsymbol{E}_{inc}$-parallel for *C*.

Figure B-14: Amplitude variance for measurement *C*, where red curves correspond to tendon ducts and black curves to rebar reflections.

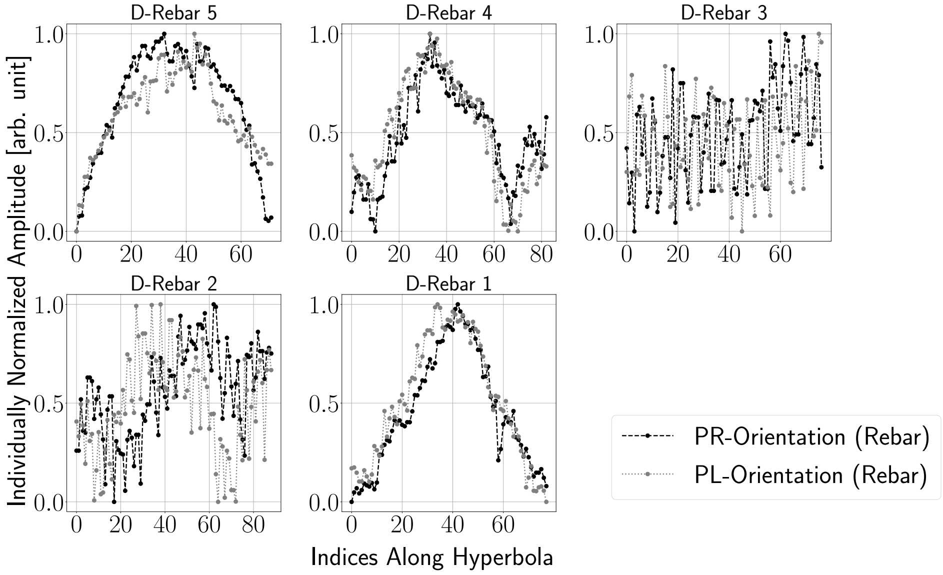

(a) Individual normalization for *D*.

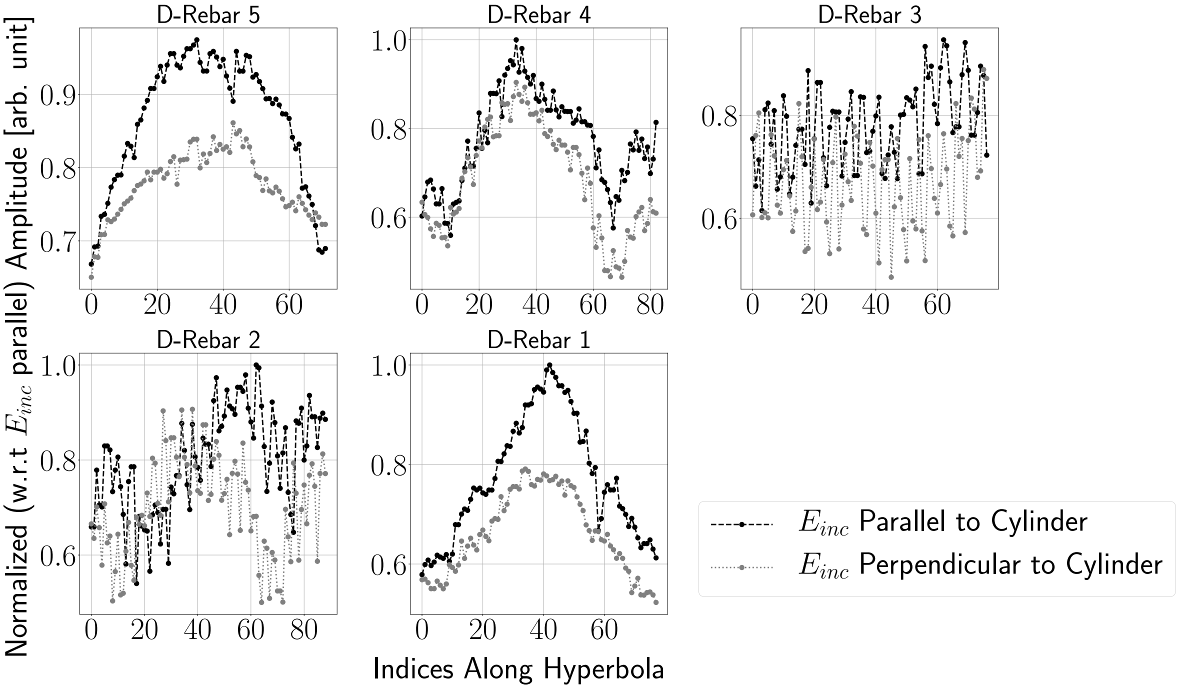

(b) Normalization with respect to $\boldsymbol{E}_{inc}$-parallel for *D*.

Figure B-15: Amplitude variance for measurement *D*, where black curves correspond to rebar reflections.

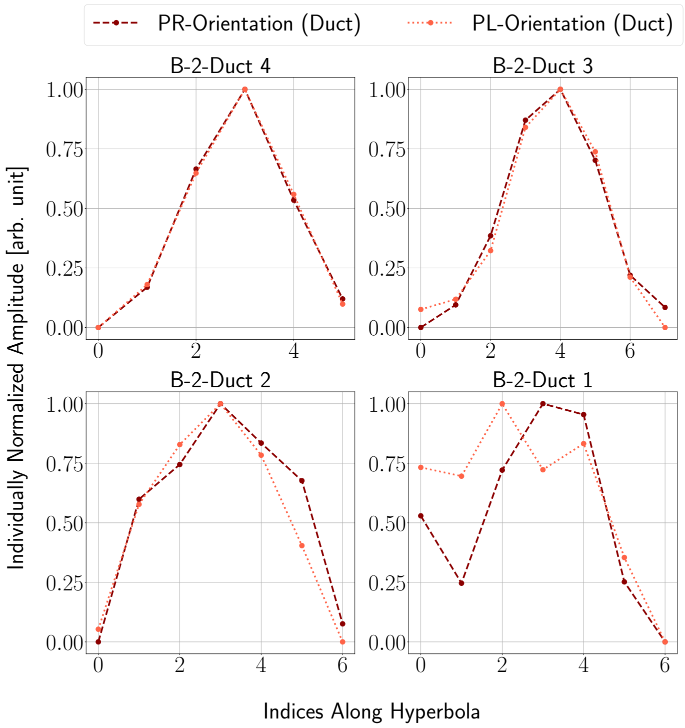

(a) Individual normalization for *B-2*.

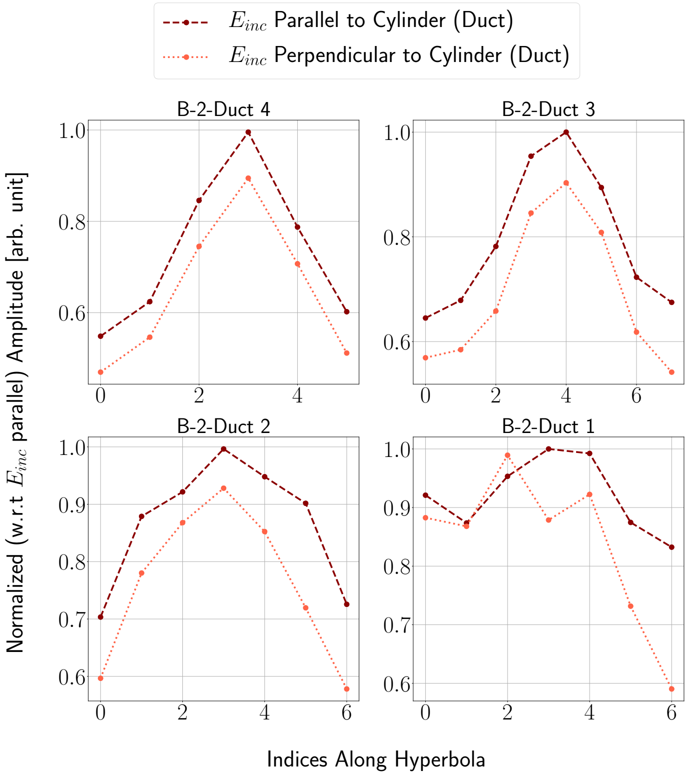

(b) Normalization with respect to $\boldsymbol{E}_{inc}$-parallel for *B-2*.

Figure B-16: Amplitude variance for measurement *B-2*, where red curves correspond to tendon duct reflections.

Orthogonal Polarization Amplitude Ratios

This section illustrates the amplitude relationship for the considered orthogonal antenna orientations.

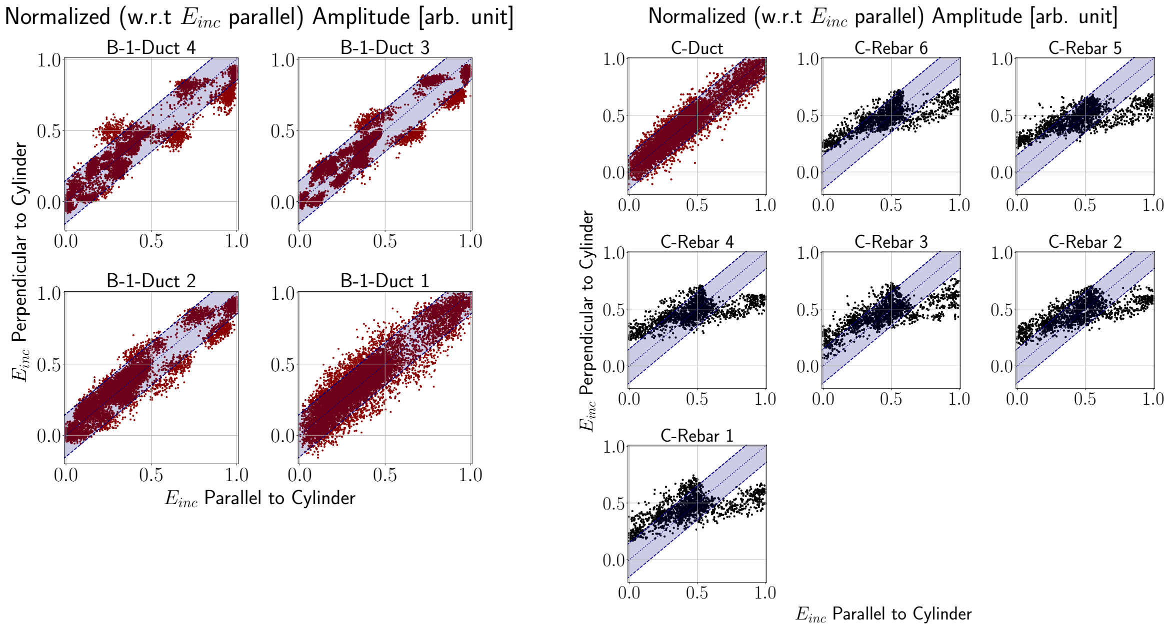

(a) Survey *B-1*.

(b) Survey *C*.

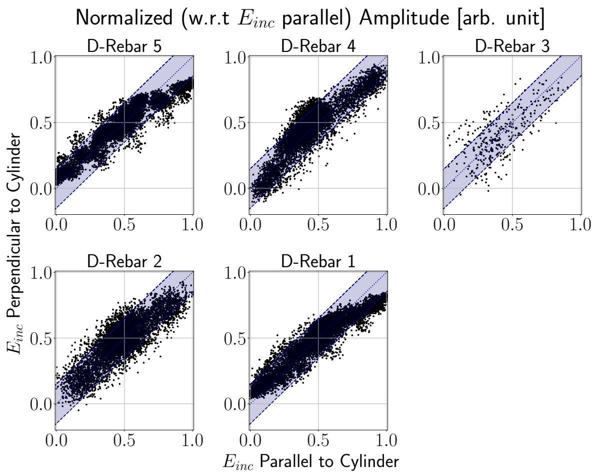

(c) Survey *D*.

Figure B-17: Amplitude ratios for the orthogonal polarizations $\boldsymbol{E}_{inc}$-parallel and $\boldsymbol{E}_{inc}$-perpendicular for a range of ten traces around the apex trace of the hyperbola range. Red corresponds to tendon ducts and black to rebars. The blue shaded area marks a $10\ \%$ range around the angle bisecting line.

The following Figure B-18 shows the mean of the hyperbola range for the measurements *B-1*, *C* and *B-2*. A complete discussion of this attribute is presented in Chapter 6. Investigating *B-2* indicates a gradual decrease of the maximum value with an increase in concrete cover for both polarizations. In contrast, the minimum mean value obeys a jump like behavior from the upper two tendon ducts to the lower two which is further analyzed by the peak-to-peak ratio.

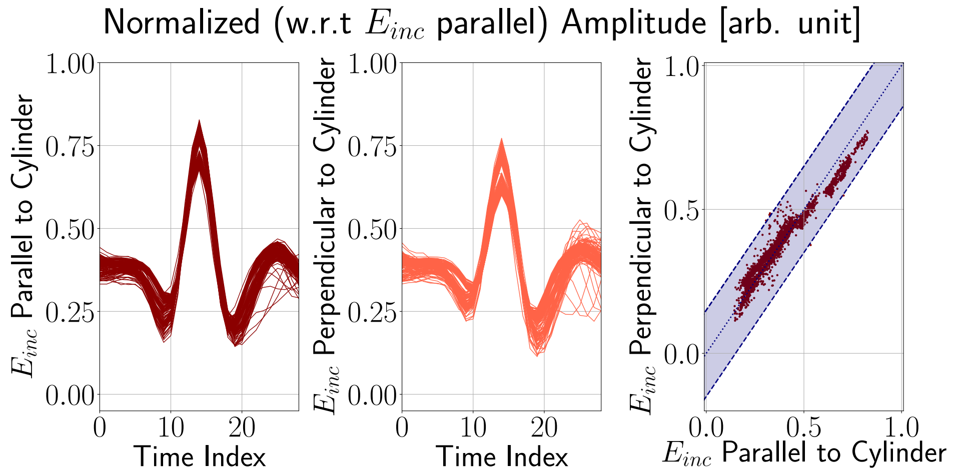

(a) Survey *B-1*.

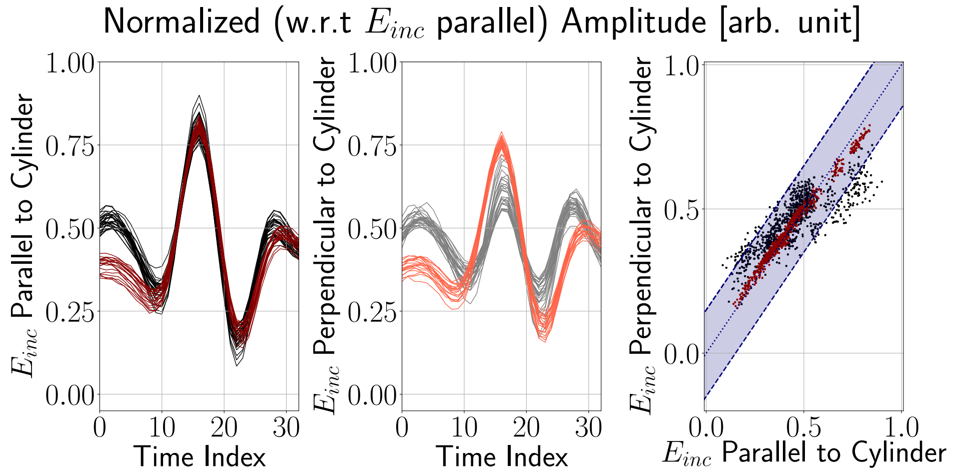

(b) Survey *C*.

Figure B-18: Mean trace over the hyperbola range for all events within each specimen extracted in multiple B-scans. The left of each image contains the graph for the $\boldsymbol{E}_{inc}$-parallel polarization, the middle the graph for the $\boldsymbol{E}_{inc}$-perpendicular polarization and the right graph illustrates the relationship between them. Red corresponds to tendon ducts and black to rebars. The blue shaded area marks a $10\ \%$ range around the angle bisecting line.

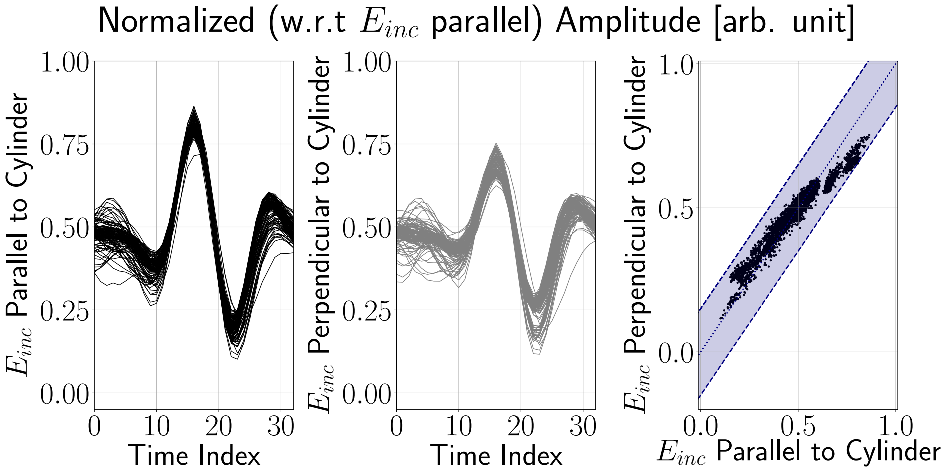

(a) Survey *D*.

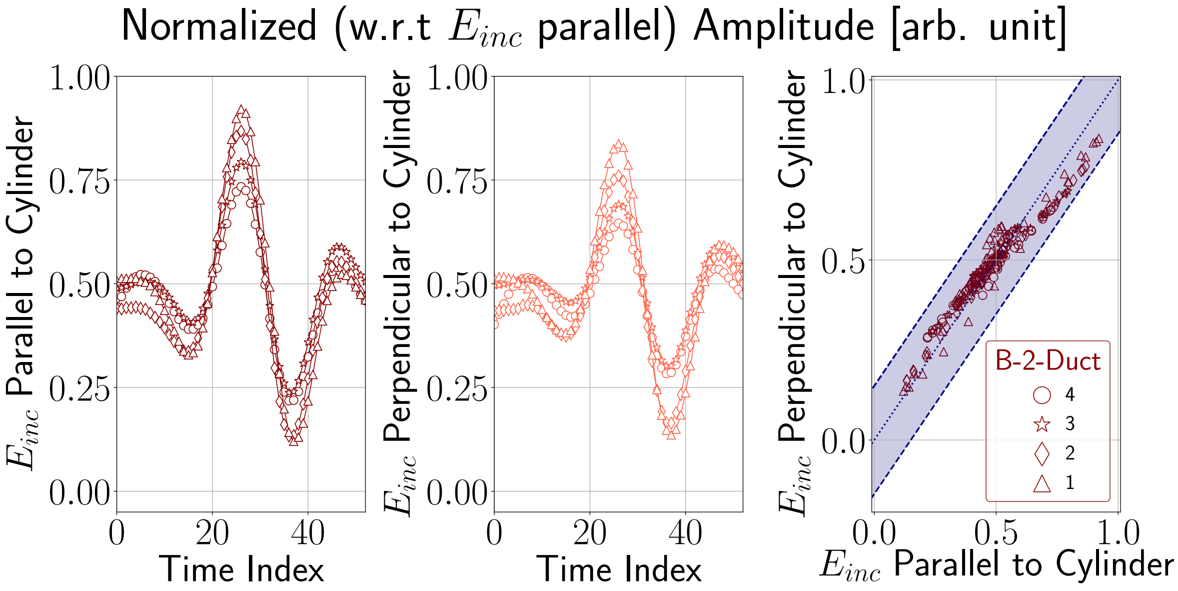

(b) Survey *B-2*.

Figure B-19: Mean trace over the hyperbola range for all events within each specimen extracted in multiple B-scans. The left of each image contains the graph for the $\boldsymbol{E}_{inc}$-parallel polarization, the middle the graph for the $\boldsymbol{E}_{inc}$-perpendicular polarization and the right graph illustrates the relationship between them. Red corresponds to tendon ducts and black to rebars. The blue shaded area marks a $10\ \%$ range around the angle bisecting line.

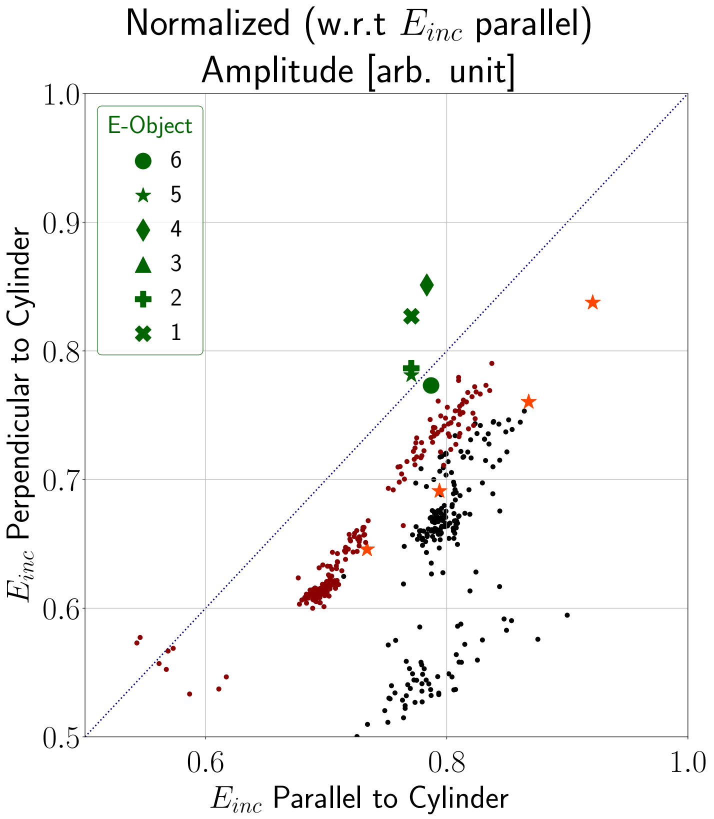

Figure B-20: Apex value of the mean trace over the hyperbola range for each reflector extracted in multiple B-scans; $\boldsymbol{E}_{inc}$-perpendicular as a function of $\boldsymbol{E}_{inc}$-parallel. Red corresponds to tendon ducts and black to rebars. Measurement *B-2* is shown as bright red stars and measurement *E* as green markers.

Autocorrelation

This section presents the autocorrelation of the apex trace with trending and repetitive behavior independent of the object type. Comparison between the different scanner measurements shows that the autocorrelation functions related to tendon duct reflections are distributed mainly around the angle bisecting line while for rebars the line around which they are centered appears to be slightly tilted.

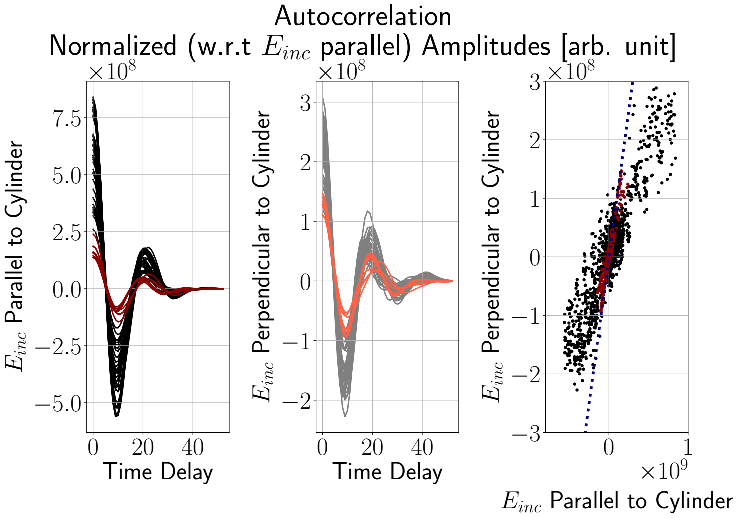

(a) Survey *A*.

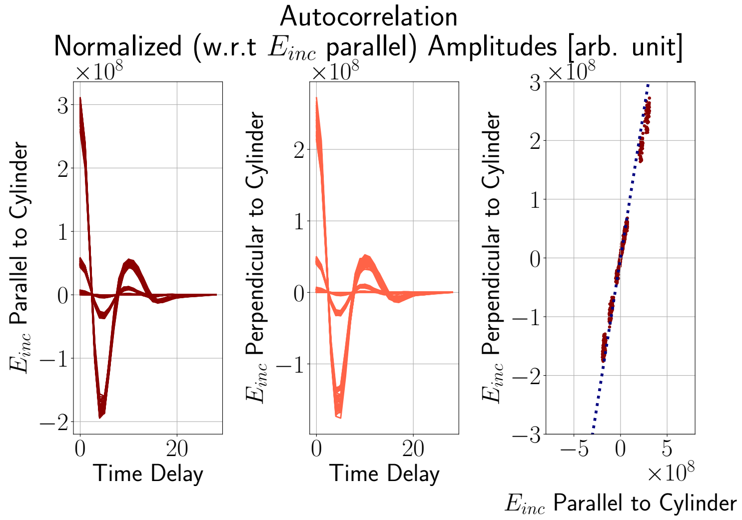

(b) Survey *B-1*.

Figure B-21: Autocorrelation function of the apex trace of the hyperbola range of the tested events within each specimen. Where $\boldsymbol{E}_{inc}$-parallel is on the left of each image and $\boldsymbol{E}_{inc}$-perpendicular in the middle. The scatter plot on the right shows the relationship between the two polarizations. Red corresponds to tendon ducts and black to rebars.

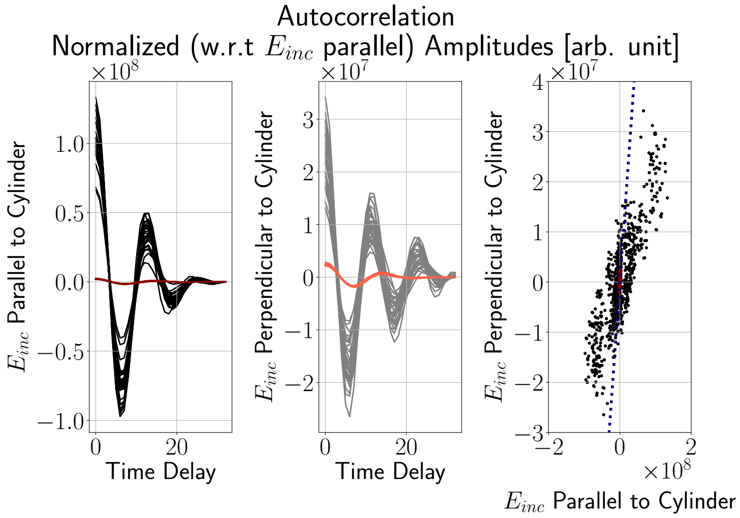

(a) Survey *C*.

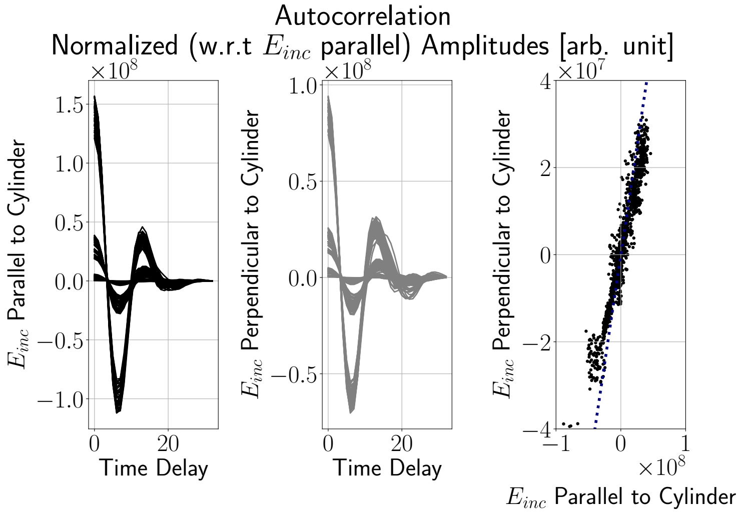

(b) Survey *D*.

Figure B-22: Autocorrelation function of the apex trace of the hyperbola range of all tested events within each specimen. Where $\boldsymbol{E}_{inc}$-parallel is on the left of each image and $\boldsymbol{E}_{inc}$-perpendicular in the middle. The scatter plot on the right shows the relationship between the two polarizations. Red corresponds to tendon ducts and black to rebars.

Peak-To-Peak Response

Within this section the peak-to-peak amplitude ratio of $\boldsymbol{E}_{inc}$-parallel as a function of $\boldsymbol{E}_{inc}$-perpendicular is shown for all measurements (*A*, *B-1*, *C*, *D*, *B-2* and *E*). In Figure B-23 the red and black data points represent tendon duct and rebar related reflections, respectively. Bright red stars mark the tendon duct reflections from measurement *B-2* and green markers the objects from *E*. The shaped areas visualize the result of the logistic regression as described in Section 5-4-3.

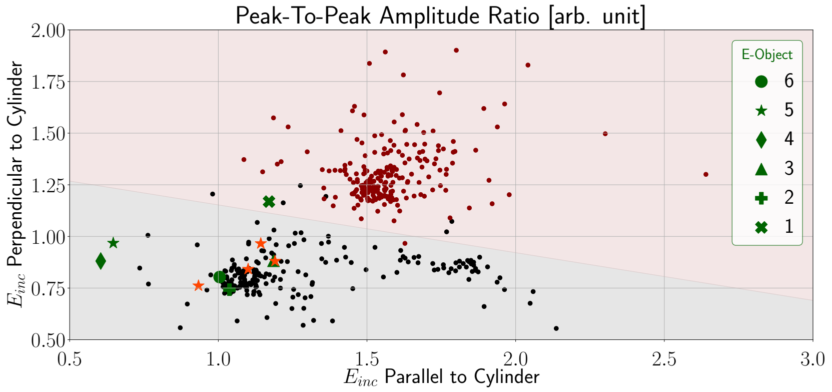

Figure B-23: Relationship of the peak-to-peak amplitude ratio for the two considered polarizations. Red corresponds to tendon ducts and black to rebars. The shaded areas are the result of the logistic regression. Measurement *B-2* is shown as bright red stars and measurement *E* as green markers.

B-4 Geometry of the Hyperbolic Signature

This section contains the hyperbolic signatures of the reflection events from tendon ducts and rebars for the four scanner measurements with different concrete covers and diameters.

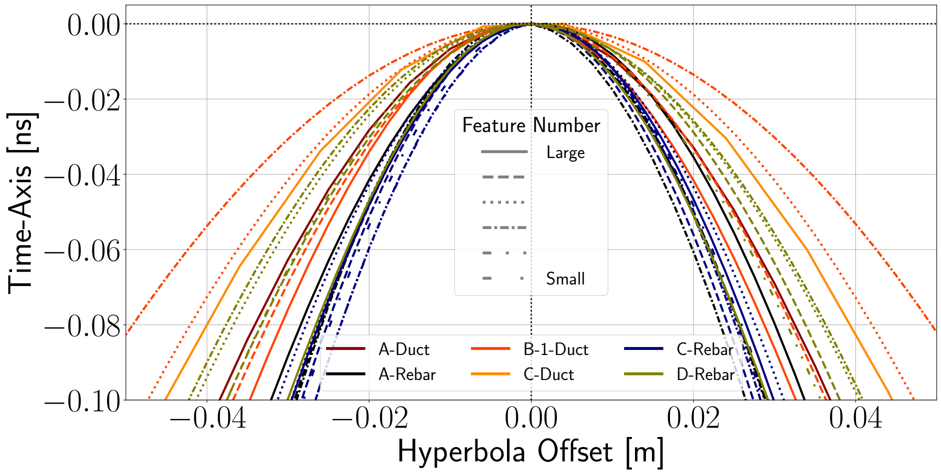

Figure B-24: Hyperbolas for the reflection events within the scanner measurements. The color scheme describes the particular survey and the line style refers to the object number.

B-5 Random Data Points

This Section presents the most promising attributes to evaluate the features in comparison with randomly extracted amplitudes (purple starts). Clearly, they do not correspond to any of the two evaluated classes: tendon duct or rebar. Within in the relation between the maximum absolute amplitude and the cumulative energy in Figure B-25 the points obey a chaotic behavior. For the apex amplitudes of the two polarizations In Figure B-26 they show extremely low values following the angle bisecting line.

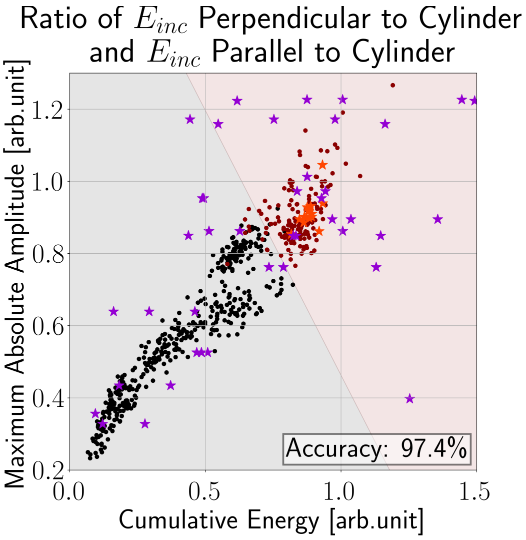

Figure B-25: Maximum absolute amplitude and cumulative energy of the anomalies for the two antenna polarizations. Red dots correspond to tendon ducts in *A*, *B-2* and *C* whereas black dots to rebars in *A*, *C* and *D*. Bright red stars correspond to the upper three tendon ducts in *B-2*. The shaded area represents the result of the logistic regression. In addition, purple stars represent random data points witch do not correspond to any of the classes.

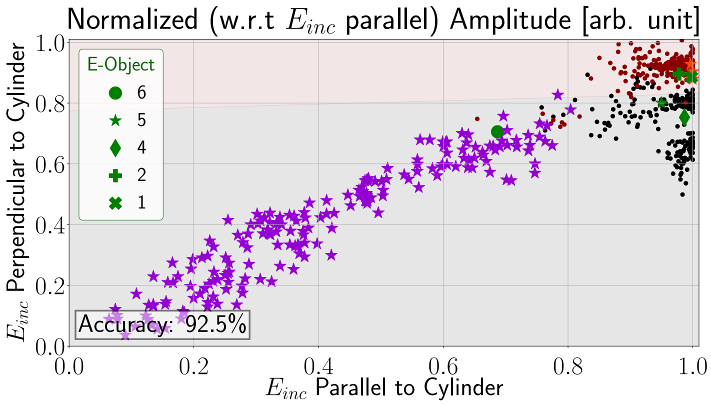

Figure B-26: Relationship for the apex amplitudes of the hyperbolas within the $\boldsymbol{E}_{inc}$-parallel and $\boldsymbol{E}_{inc}$-perpendicular polarization. Red dots correspond to the reflection hyperbolas of tendon ducts and black dots to rebars, both for scanner measurements (*A*, *B-1*, *C* and *D*). Bright red stars indicate the data points for measurement *B-2* and green markers are related to the different reflectors in *E*. In addition, purple stars represent random data points witch do not correspond to any of the classes.

Appendix C

Python Programs

Table C-1: Summary of the Python programs used to apply the preprocessing and hyperbola selection.

Program	Description
A01_preprocess_3D_DZT	Reads in 3D GPR *dzt*-file (GSSI acquisition system) containing a conjunction of the individual measured profiles; Performs the processing steps (dewow and background removal).
A01_preprocess_2D_DZT	Reads in 2D GPR *dzt*-files (GSSI acquisition system) each representing one measurement profile; Performs the processing steps (dewow and background removal).
A02_extract_reflector	Code to extract reflection events within the data; Select the pixels of the hyperbolic signature.
A02b_extract_multiple_reflectors	Takes the selected hyperbolas and transfers them to multiple B-scans.

Table C-2: Summary of the Python programs used to apply the attributes and extract the features.

Program	Description
A03_amplitude_variance	Extracts the amplitude variation along the selected hyperbola (output of A02).
A03b_amplitude_polarization_comparison	Computes the range around the hyperbola for the defined time window; Creates a scatter plot of the ten trace range around the cutout apex trace.
A03b_mean_amplitude_polarization_comparison	Calculates the arithmetic mean of the hyperbola; Relates the mean for the two polarizations.
A05_hyperbola _geom	Fits the hyperbola equation (zero radius) to the selected hyperbolas (output from A02b); Relates the resultant velocities.
A07_autocorrelation	Computes the autocorrelation for the apex trace.
A08_peak_to_peak	Extracts the peak and trough value of the cutout apex trace; Evaluates the peak-to-peak ratio as a function of TWT.
A09_reverberation	Extracts the amplitude corresponding to the creeping wave; Relates it to the backscattered reflection.
A10_refl_prop_attribute	Calculates all six reflection and propagation attributes and the cumulative energy.
A10_refl_prop_attribute_features	Evaluates the reflection, propagation and cumulative energy attribute for the reflectors.

Python Functions

Table C-3: Summary of the Python functions used within the python programs to perform attribute analysis (A to M).

Function	Application
amplitude_range.py	Extracts a range of a predefined time window around the hyperbolic signature.
apex.py	Calculates the x-index of the apex of the selected hyperbola.
assign_header_data.py	Extracts header and data information from *dzt*-file.
autocorr.py	Computes the autocorrelation of a single input time series.
choose_hyperbola.py	Opens a figure to select the hyperbolic reflection pixels.
create_set.py	Takes the selected hyperbolic reflection and finds the corresponding reflection within other B-scans.
cumulative_energy.py	Calculates the cumulative energy for the defined time window.
dewow.py	Returns the dewowed version of the input data.
dir_rem.py	Returns the background removed version of the input data.
find_indices_of_both_polarizations.py	Finds x indices corresponding to the overlap positions for the two antenna orientations.
find_yvals.py	Finds index corresponding to the maximum amplitude of a defined time window range.
fit_hyperbola.py	Fits a hyperbola based on the hyperbolic equation (zero radius).
index_correlation_PR_PL_manual.py	Finds the reflection cutout in the second antenna orientation via the overlap positions.
logistic_regression_check.py	Creates the x and y coordinates for the decision line; Classifies input test data.
manual_meas_to_PR_PL.py	Converts the 2D data vector from 2D *dzt*-file to two separate vectors containing PR and PL data.

Table C-4: Summary of the Python functions used within the python programs to perform attribute analysis (N to Z).

Function	Application
normalize_ampl_range.py	Normalizes each trace cutout within the hyperbola range individually for each antenna orientation.
normalize_ampl_range_Eparallel.py	Normalizes the hyperbola range with respect to the $\boldsymbol{E}_{inv}$-parallel polarization.
peak_to_peak.py	Calculates the peak and trough value for the apex trace.
readDZT.py	Converts bindary *dzt*-files to ASCII and hands over header and data values.
reduce_ind.py	Reduces the indices of the selected hyperbola to end with a single time index per position index.
relate_indices_PR_PL_hypers.py	Relates hyperbolic signatures of PR and PL to apex and to same number of samples for both.
select_region.py	Opens a separate window to select the hyperbolic reflection.